Partial wave analysis of meson resonances that decay $K^*\bar{K}$ using data from the GlueX experiment

by

Sebastian Cole

A Dissertation Presented in Partial Fulfillment
of the Requirements for the Degree
Doctor of Philosophy

Approved July 2021 by the
Graduate Supervisory Committee:

Prof. Michael Dugger, Chair
Prof. Barry Ritchie
Prof. Ricardo Alarcon
Prof. Igor Shovkovy

ARIZONA STATE UNIVERSITY

July 2021

ABSTRACT

The GlueX experiment housed in hall D of the Thomas Jefferson National Laboratory was created to map the light meson spectrum, which will contribute to the Standard Model of particle physics by strengthening our understanding of the strong interaction. GlueX is a medium-energy photoproduction experiment that utilizes a linearly polarized photon beam to create hadronic forms of matter. By mapping the light meson spectrum, the GlueX collaboration hopes to identify meson states forbidden by the Constituent Quark Model. As a main research objective, the GlueX collaboration is searching for hybrid $q\bar{q}g$ meson states that exhibit exotic quantum numbers.

Utilizing a polarized photon beam, GlueX was designed to search for hybrid mesons candidates. One such candidate is the η_1', which is predicted to decay to $K^*\bar{K}$ and have a mass near 2.3 GeV (Meyer and Van Haarlem, 2010; Meyer and Swanson, 2015). At this time, very few mesons have been identified in the 2.0 GeV mass region. This means any tools developed to search for meson states above 2.0 GeV need to to be verified in searches for known mesons at lower masses. In order to search for η_1' hybrid meson candidate in $\gamma p \to pK^+K^-\gamma\gamma$ events, it is imperative to identify meson states decaying $K^*\bar{K}$ that contribute to the low mass region, defined in this document as particles having PDG masses between 1400 and 1600 MeV. Identifying what mesons exist in the low mass region is also critical to mapping the light meson spectrum and determining the quark-gluonic content of those meson states.

The results of a partial wave analysis (PWA) of $\gamma p \to pX$ where $X \to K^*\bar{K}$ from $\gamma p \to pK^+K^-\gamma\gamma$ events in GlueX are presented. The PWA includes wave contributions with total angular momentum $J = 0$, 1, and 2 with possible identities of meson states with masses between 1400 and 1600 MeV revealed. In the $J = 0$ invariant mass distribution, the $\eta(1405)$ and $\eta(1475)$ are identified, adding to the

debate as to whether two pseudoscalar mesons exist in the low mass region. For the $J = 1$ distribution, the $f_1(1420)$ and $f_1(1510)$ axial vector mesons are seen, where the former helps further elaborate on the $E\iota$ puzzle of the twentieth century (Bertin *et al.*, 1995). Adding to the controversy of mesons in the low mass region, evidence for existence of the $f_2(1430)$ meson is strengthened in the $J = 2$ distribution. Additionally, the $f_2'(1525)$ state is seen. This work lays a foundation for the ASU meson physics group to continue on to a wider search for hybrid mesons in the $\gamma p \to pK^+K^-\gamma\gamma$ reaction topology.

Dedicated to my father, the late Jonathan Darrough Cole. I may never have pursued education at the highest level without your influence. You will forever have a vital impact on my life.

This achievement would not be possible without the people guiding, influencing, and assisting me along the way. Here, I attempt to briefly acknowledge their role.

I begin by acknowledging those at the Jefferson National Accelerator Facility and in the GlueX collaboration. To Elton Smith, thank you for assisting in my integration to the Jefferson Lab environment as a mentor. I thank Alex Barnes for initially guiding me through shifts in the counting house. Thank you to Alex Austregesilo and Thomas Britton for always patiently answering my questions regarding the GlueX software. As for Dave Mack, thank you for candidly sharing your insight and teaching me the subtleties to the art of this field. I thank Justin Stevens for taking the time to answer my questions and assist me with maintaining the TPOL software. I would like to acknowledge Beni Zihlmann for all his effort in assisting with maintaining TPOL. As for Mark Dalton, thank you for helping me stay grounded through some of the most difficult times in my life. The efforts of these people, and more, made it possible for me to work at the lab. Furthermore, they have taught me to perform particle physics experiments and analyze the collected data.

Being at Arizona State University for a decade means I have had many interactions, resulting in many people to acknowledge for their involvement in my education. Here, I endeavor to thank them for their roles. Thanks to Araceli Vizcarra and Ixchell Paape for all the administrative help over the years. I also thank Deborah Denson for this role, especially her patience in handling the difficulties of my move to Newport News to work at the lab. To Daniel Martin, your mentorship was integral to my success in the early days of my physics education and pushed me to pursue my P.h.D. I would like to acknowledge Gary Adams for the part he has played in my teaching efforts. I have learned a lot from his approach and love for educating students. To Barry Ritchie, thank you for supporting me through my time at Jefferson Lab and making yourself available to provide your thoughts on the work of this document.

I must profusely thank my advisor, Michael Dugger. Without the time he has taken to teach me all he knows about nuclear particle physics, I do not believe I would be where I am today. My success can largely be attributed to his tireless efforts.

Finally, I must thank my family. To Ed, Sue, and Ali Bull, thank you for your years of support. I thank my mother, Elizabeth Cole-Sonneveld, for sacrificing so much to ensure I received the best education and for assisting me in staying the course to achieve this goal. My sibling, Alexandra Cole, has always pushed me to be my best and I thank them for always being available to assist me in maintaining my sanity. Amanda Bull, my future wife, has learned only what my mother and sibling knew, that I can be very difficult. Your constant presence from when I applied to the point of my completion of graduate school has kept me grounded. Your unwavering support has made this possible and I thank you.

TABLE OF CONTENTS

CHAPTER Page

CHAPTER Page

LIST OF TABLES

*Fit width column is determined by $\Gamma = 2.355\sigma$ for full width at half maximum.

LIST OF FIGURES

Figure Page

Figure Page

Figure Page

Figure Page

Figure Page

Figure Page

Figure Page

Chapter 1

INTRODUCTION

It is tenable that the origins of particle physics can be tracked to the atomic model and Thomson's discovery of the electron in 1897. This seemingly humble beginning is the first of a slew of discoveries throughout the 1900's to the new millennium, leading to the development and refinement of the Standard Model of particle physics. The Standard Model is humanities attempt at describing the interaction of particles with respect to electromagnetic, weak, and strong forces. Despite the century of work, many questions regarding the detailed nature of hadronic phenomena remain unanswered due to computational difficulties of QCD. Hadronic models (including lattice calculations) are utilized for explanation of, and predictions for, hadronic phenomena. Work being conducted at the Thomas Jefferson National Accelerator Facility provides the constraints needed for builders of hadronic models.

The standard Constituent Quark Model describes hadrons as consisting of quarks. However, it fails to describe hadrons with exotic quantum numbers, and hadrons with more than three quarks. QCD's incorporation of the gluon as the mediator of the strong interaction that binds quarks together allows for the existence of such phenomena. These phenomena are of great interest to the particle physics community since inconclusive experimental evidence exists for these states, and conclusive evidence, alongside measurement of their observables, will improve our understanding of the strong interaction.

Mesons are hadrons that consist of a quark-antiquark pair bound by gluons. In the quark model, hadrons have J^{PC} quantum numbers determined by quark contributions to that total. With QCD's inclusion of the gluon, hadrons have J^{PC} quantum numbers

with quark contributions, as well as non-quark contributions. This is accomplished by an excitation of gluon(s) from virtual to real, resulting in a gluonic addition to the state's angular momentum. Currently, the GlueX experiment attempts to provide evidence and observables for hybrid meson candidates to assist in updating modern QCD measurements. To accomplish this goal, it is necessary to accurately map the light meson spectrum. To highlight the importance of this search and for contextual purposes, a historical discussion of particle physics is provided.

1.1 The constituent quark model

In 1932, Werner Heisenberg suggested that the proton and neutron were manifestations of the same particle named the nucleon (Griffiths, 2010). The mass difference between the proton and neutron was attributed to the charge difference. As a result, the nuclear force between two neutrons, two protons, or a proton and a neutron should be the same. This symmetry can be represented with an $SU(2)$ group in the same manner as spin, such that

$$p = \begin{pmatrix} 1 \\ 0 \end{pmatrix} \qquad n = \begin{pmatrix} 0 \\ 1 \end{pmatrix},$$

where p is equivalent to spin up and n is equivalent to spin down. Following the logic for formulating spin, Heisenberg introduced isospin, a quantum number that is intrinsic to particles* . In particular, he assigned the proton and neutron to an isospin doublet with total isospin $I = \frac{1}{2}$ with projection $I_3 = \pm\frac{1}{2}$. Heisenberg's isospin formalism is applicable to hadrons.

Despite the quark flavors, the treatment of quark interactions are equal in QCD. Thus, the strong interaction possesses a symmetry similar to the nuclear force of the protons and neutrons described by Heisenberg, known as flavor symmetry. For a

* Although spin is in the name, isospin is not a physical spin.

system of quarks, the Hamiltonian is

$$\hat{H} = \hat{H}_0 + \hat{H}_{strong} + \hat{H}_{em}, \tag{1.1}$$

where $\hat{H}_0$ is the kinetic and rest mass energy of the quarks, $\hat{H}_{strong}$ is the strong interaction term, and $\hat{H}_{em}$ is the electromagnetic interaction term. If the $m_u \approx m_d$ and $\hat{H}_{strong} \gg \hat{H}_{em}$, the first generation quarks exhibit a $SU(2)$ flavor symmetry, such that

$$u = \begin{pmatrix} 1 \\ 0 \end{pmatrix} \qquad d = \begin{pmatrix} 0 \\ 1 \end{pmatrix},$$

where u is equivalent to spin up and d is equivalent to spin down. As with the proton and neutron, the up and down quark have total isospin $I = \frac{1}{2}$ with the up quark having $I_3 = \frac{1}{2}$ and the down quark having $I_3 = -\frac{1}{2}$, with the antiquarks having opposite I_3. The implication of this formalism is that the up and down quark are indistinguishable, meaning they can be interchanged to form other particles of similar masses. The isospin of a meson or a baryon is determined by their quarks, and is particularly important for light hadrons consisting of up and down quarks because isospin states $\phi(I, I_3)$ are conserved by the strong interaction. It is also important to lighter hadrons since the $\phi(I, I_3)$ for all quark flavors, other than up and down, are $\phi(0, 0)$ (Thomson, 2013)* .

As already noted, mesons are $q\bar{q}$ pairs in the quark model. Mesons are fully described by J^{PC} quantum numbers. J is the quantum number for the total angular momentum determined by L and S, where L is the quantum number for the relative angular momentum and S is the quantum number for spin (not to be confused with strangeness). As previously discussed, the possible values for S are 0 and 1 for

* The idea of an $SU(2)$ flavor symmetry was extended to $SU(3)$ by Gell-Mann using $m_u \approx m_d \approx m_s$ and $\hat{H}_{strong} \gg \hat{H}_{em}$ approximations. Attempts to usefully extend to $SU(4)$ symmetry or beyond break down due to the mass difference being greater than the binding energies of QCD (> 1 GeV).

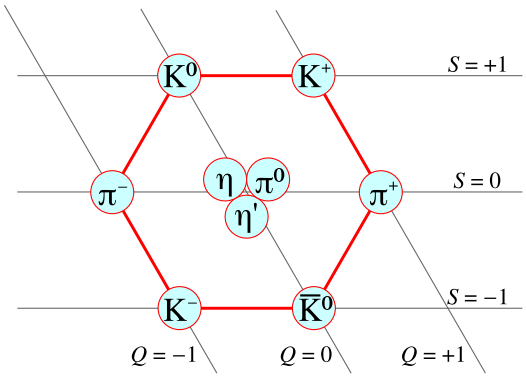

(a) Nonet for spin-0 mesons.

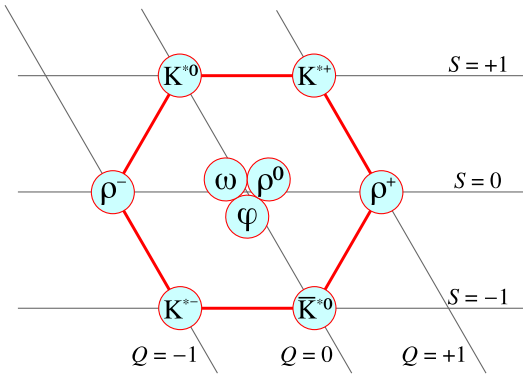

(b) Nonet for spin-1 mesons.

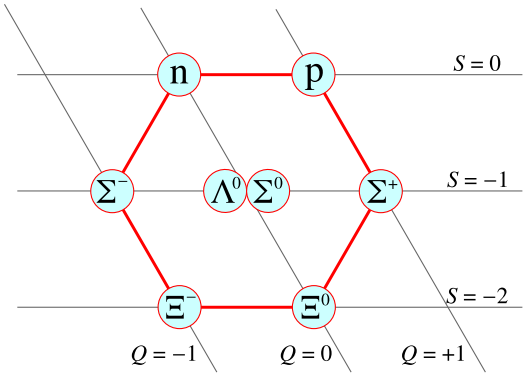

(c) Nonet for spin-$\frac{1}{2}$ baryons.

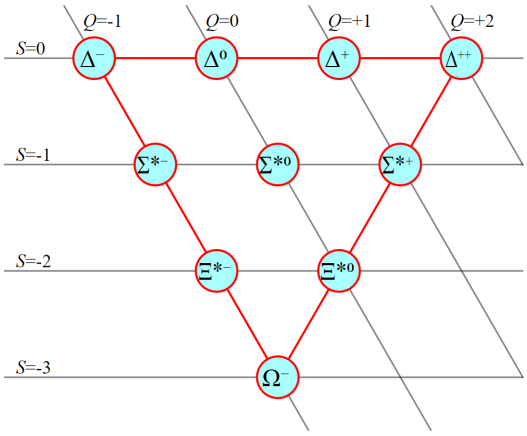

(d) Decuplet for spin-$\frac{3}{2}$ baryons.

Figure 1.1: Examples of Gell-Mann's Eightfold Way multiplets where the diagonal lines give the charge, Q, and horizontal lines give the strangeness, S, of the particles ((a) Pse (2021); (b) Vec (2021); (c) Oct (2021); (d) Dec (2021)).

antiparallel and parallel spins, respectively, and L are integers $(0, 1, 2, ...)$. These conditions lead to possible J values of $|L - S|$ to $L + S$ by integer steps (Griffiths, 2010).

Parity (P), a quantum number introduced as a conserved quantity by Eugene Wigner in the 1930s, describes the state of a system under spatial transformation $x \to -x$, $y \to -y$, and $z \to -z$. If the system remains unchanged, $P = 1$; if the wavefunction is out of phase by 180°, $P = -1$. Before Tsung-Dao Lee and Yang Chen-Ning showed otherwise in 1956, it was believed that parity was a conserved quantity in reactions. Studying Cobalt 60 beta decays, Lee and Yang showed this

to be true in electromagnetic and strong interactions, but not in weak interactions (Griffiths, 2010). For reactions, the parity is determined as the multiplication of its parts. For meson states, the parity is determined by $P = (-1)^{L+1}$.

Not to be confused with charm number, charge conjugation (C) is the transformation of all particles to their respective antiparticles. If the system remains unchanged, $C = 1$; if the wave function of the system is out of phase by 180°, $C = -1$. This only applies to neutral mesons that are their own antiparticle, where the charge conjugation is determined by $C = (-1)^{L+S}$ (Griffiths, 2010).

Combining J, P, and C according to the above rules produce $0^{-+}, 0^{++}, 1^{--}, 1^{+-}$, $1^{--}, 2^{--}, 2^{-+}, 2^{++}, ...$ as allowed J^{PC}'s. For some of these allowed J^{PC}'s, there currently exists a $J^{PC} = 0^{-+}$ meson nonet for pseudoscalar mesons (See Figure 1.1a) from $S = 0$ and $L = 0$, a $J^{PC} = 1^{--}$ meson nonet for vector mesons (See Figure 1.1b) from $S = 1$ and $L = 0, 2$, a $J^{PC} = 1^{++}$ meson nonet for pseudovector mesons from $S = 0$ and $L = 1$, a $J^{PC} = 0^{++}$ meson nonet for scalar mesons from $S = 1$ and $L = 1$, a $J^{PC} = 1^{++}$ meson nonet for axial vector mesons from $S = 0, 1$ and $L = 1$, and a $J^{PC} = 2^{++}$ meson nonet for tensor mesons from $S = 1$ and $L = 1, 3$ (Griffiths, 2010). Furthermore, $0^{--}, 0^{+-}, 1^{-+}, 2^{+-}, ...$ J^{PC}'s are forbidden by the quark model. These so called forbidden quantum numbers are said to be exotic since they imply the existence of something outside the $q\bar{q}$ system (See Section 1.2).

Besides the baryon number (B), electric charge (Q), total angular momentum (J), strangeness (S), parity (P), charge conjugation (C) and isospin (I), G-parity (G) is also conserved in strong interactions*. Since C-parity only applies to neutral mesons, for charged mesons it is necessary to generalize to G-parity, which then accounts for the isospin of the meson. For mesons, G-parity is determined by $G = (-1)^{L+S+I}$.

* Baryon number, like strangeness, is a quantum number such that baryons are $B = 1$, antibaryons are $B = -1$, and mesons are $B = 0$.

1.2 Exotics

The quark model defines hadrons as subatomic particles that consist of quark antiquark pairs, three quarks, or three antiquarks. However, QCD does not succumb to these constraints, creating the possibility for the existence of exotic forms of matter. Exotic hadrons are subatomic particles that consist of quarks and gluons, but are not possible in the quark model. With QCD, hadrons have many constituent possibilities, including, but not limited to, hybrid mesons ($qg\bar{q}$), tetraquarks ($qq\bar{q}\bar{q}$), pentaquarks ($qqqq\bar{q}$), and glueballs (gg). This section will focus on exotic hadrons as they pertain to this analysis effort.

1.2.1 Hybrid mesons

Hybrid mesons are quark-antiquark pairs with exotic quantum numbers that are forbidden by the constituent quark model as discussed in Section 1.1 (Klempt and Zaitsev, 2007). In QCD, these possibilities are explained by a gluonic field contributing $J^P = 1^-$ to the system, which is developed by the inclusion of the gluon as the mediator of the strong interaction. Possible light unflavored hybrid meson candidates are shown in Figure 1.2 from the HadSpec collaboration's lattice QCD predictions. Finding and classifying light hybrid mesons are the main goals of the GlueX experiment. Other experiments have searched, or are searching, for hybrid meson candidates in electron-positron and proton-antiproton collisions through heavy meson decays, as well as direct hadroproduction of the states (Meyer and Swanson, 2015). The GlueX experiment is unique in that it uses a linearly polarized photon beam to help assign parity in the search for hybrid mesons (See Section 1.3.1).

1.2.2 *Glueballs*

Glueballs are hadrons consisting of multiple gluons, modeled as $gg, ggg, gggg, ...$ states with integer spin. Currently, the existence of glueballs have yet to be confirmed since separating them from standard meson states is difficult. Pomeron exchange in photoproduction can produce exotic states, which could be hybrids, glueballs, or glueball-meson mixed states. Harnessing this phenomenon to classify light mesons in GlueX will assist in the completion of both quark model, and exotic light meson, nonets. Extraneous particles that evade classification within classical nonets may indicate they need to be explained by alternate physics (Mathieu *et al.*, 2009). While mapping of the light meson spectrum, the study of $f_0(980)$, $f_0(1370)$, $f_0(1500)$, and $f_0(1710)$ mesons will be of particular interest because these 0^{++} mesons could be glueball or glueball-meson mixed states (Klempt and Zaitsev, 2007).

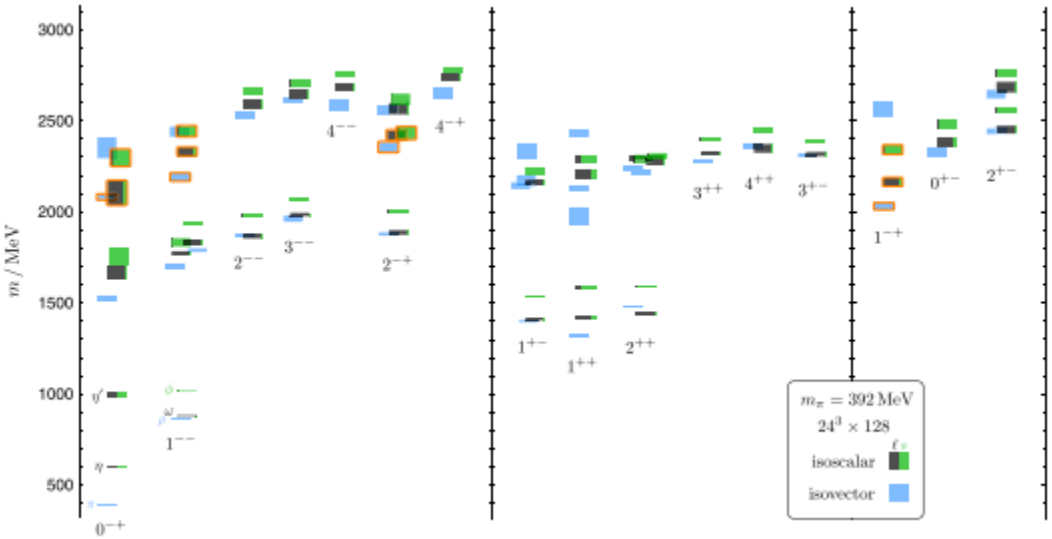

Figure 1.2: HadSpec collaboration's lattice QCD prediction of the light unflavored meson spectrum including isoscalar (blue) and isovector (black) states with potential strange quark contributions (green) and 1^{+-} gluon contributions (orange) (Dudek *et al.*, 2013).

1.3 The GlueX experiment

The GlueX experiment located at the Thomas Jefferson Laboratory in Newport News, Virginia assists in understanding confinement within QCD by identifying states with possible gluonic field excitations predicted by models of QCD, including lattice calculations (See section 1.2.1). A main goal is to outline the light hybrid meson spectrum as shown by the HadSpec predictions in Figure 1.2.

1.3.1 Bremsstrahlung photon beam

Bremsstrahlung is the process by which a photon is emitted from the deceleration of a charged particle due to interaction with another charged particle, also known as braking radiation. Coherence is achieved if the Bremsstrahlung process occurs in a lattice, such that the incident particle's momentum transfer to an atom of the lattice matches the reciprocal lattice vector[*] . The GlueX experiment uses coherent Bremsstrahlung (CB) to produce a linearly polarized photon beam from an electron beam incident on a thin diamond radiator. In this instance, the electron's momentum is transferred to an atom of the diamond. If the orientation of the diamond is consistent with producing a momentum transfer matching its reciprocal lattice vector, a polarized photon is emitted. In GlueX, this process is seen as an enhancement in the energy spectrum of the photon beam with incoherent Bremsstrahlung as a background contribution (Barbosa *et al.*, 2014).

Since Quantum Electrodynamics (QED) is well understood and polarization is relatively easy to obtain, the GlueX experiment uses a polarized photon beam. Dependencies of amplitudes in PWA for photoproduction include center of mass energy ($\sqrt{s}$) and the polar angle (θ) between the incident photon and the produced meson.

[*] Coherent Bremsstrahlung is analogous to Bragg scattering.

Linear polarization of the incident photon adds an azimuthal dependency to amplitudes of the PWA, where Φ is defined as the angle between the polarization direction and the produced meson. Furthermore, parity exchange can be determined by the orientation of the linear-polarization and how it transfers to the photoproduced meson. For a positive/negative parity exchange, the photon and photoproduced meson have the same/opposite parity. This can be identified in the data by looking at the polarization transfer to the meson states because linear-polarization is transferred directly or rotated 90 for positive and negative parity exchange, respectively. In terms of the JP state of he exchange particle, a "natural parity exchange" is one where the exchange particle carries $J^P = 0^+, 1^-, 2^+, ...$ quantum numbers, while an "unnatural parity exchange" is one where the exchange particle carries $J^P = 0^-, 1^+, 2^-, ...$ quantum numbers. With this definition, scalars and vectors would be considered natural exchanges, while pseudoscalar and pseudovectors would be unnatural. However, determining the polarization of the resonance meson from its decay products require that the parity of the meson resonance is known. Thus, the linearly polarized photon beam can assist in isolating the parity exchange in the resonance meson creation, or the intrinsic parity of the meson resonance itself, if the other quantity is known (Barbosa *et al.*, 2014).

1.3.2 Triplet photoproduction and photon beam polarization

Two important leptonic processes for the interaction of a polarized photon beam incident on a nuclear target: pair photoproduction and triplet photoproduction. In pair photoproduction, the incident photon interacts with the electric field of an atom's nucleus to produce an electron-positron pair. In triplet photoproduction, the incident photon interacts with the electric field of an atomic electron that not only produces an electron-positron pair, but also ejects the atomic electron from the atom. The

cross section for triplet production from a polarized photon beam is

$$\sigma_t = \sigma_0(1 - P\Sigma\cos(2\phi)), \tag{1.2}$$

where σ_0 is the unpolarized cross section, P is the photon polarization, Σ is the beam assymetry, and ϕ is the azimuthal angle of the recoil electron. The photon's beam polarization can be determined by the azimuthal distribution of recoiling electrons and a $A(1 - B\cos(2\phi))$ fit, such that $P = B/\Sigma$ (Dugger *et al.*, 2017).

1.4 Mesons decaying $K^*\bar{K}$

The photoproduction of states decaying to $K^+K^-\pi^0$ in GlueX is of great interest to the particle physics community. Whether the decay of the photoproduced meson is through intermediaries such as $a_0(980)\pi^0$, $K^*\bar{K}$, or directly to $K\bar{K}\pi$, much can be gained by studying this reaction. The PWA of meson states decaying $K^*\bar{K}$ is the focus of the work in this dissertation, specifically in the 1400 to 1600 MeV mass region. These efforts are crucial to future searches for the η_1' hybrid meson candidate because it is necessary to produce results consistent with previous experiments to lend credence to results produced in the 2 GeV mass region. Beyond this, the work contributes to what is formerly the E/ι puzzle, by attempting to provide evidence for the $\eta(1405)$, $f_1(1420)$, and $\eta(1475)$ mesons in early GlueX data. Before describing the approach used to search for these meson states, a history of the E/ι puzzle as it pertains to $K^*\bar{K}$ decays is outlined.

1.4.1 History of $K^*\bar{K}$

In 1963 a peak at 1425 Mev with J^{PC} 0^{-+} was first reported in the $K\bar{K}\pi$ mass spectrum. The peak seen in $p\bar{p}$ annihilations at rest became known as the E-meson. Over the next 40 years, experiments observed similar results in pp and πp central

production, $\gamma\gamma$ collisions from e^+e^- interactions, and J/ψ radiative and hadronic decays. However, an issue arose because different experiments reported results with differing quantum numbers, specifically 0^{-+} and 1^{++}. The discrepancies in results was a problem that had to be solved, which became known as the E/ι puzzle (Bertin *et al.*, 1995).

To further add to E/ι puzzle, the MARKIII collaboration reported two pseudoscalar mesons in the $K\bar{K}\pi$ mass spectrum from radiative decays of the J/ψ meson in 1990. Spin-parity analysis showed a pseudoscalar at 1416 MeV decaying $a_0\pi^0$ and 1490 MeV decaying $K^*\bar{K}$, as well as an axial vector meson at 1420 MeV decaying $K^*\bar{K}$ (Bai *et al.*, 1990). These results were later confirmed by the DM2 experiment, but the decay modes of these mesons was inconsistent with MARKIII (Aaij *et al.*, 2019). Furthermore, BESIII did not find evidence of these mesons in the radiative decay of J/ψ, but did find evidence of the $\eta(1405)$, $\eta(1475)$, and $f_1(1420)$ recoiling against the ω meson in $\psi(3686)$ decays (Ablikim *et al.*, 2008; Ablikim *et al.*, 2013). The OBELIX experiment further confirmed the possible existence of two psuedoscalar mesons in the 1400 MeV region in $\bar{p}p$ annihilation at rest(Bertin *et al.*, 1995). Although the results of these experiments are inconsistent in some ways, it became clear that a lower lying pseudoscalar meson couples to $a_0\pi^0$ and $K\bar{K}\pi^0$ decay modes and a higher lying pseudoscalar meson couples to the $K^*\bar{K}$ decay mode.

Evidence of the possible quark contributions to these meson states comes from the L3 collaboration. In the study of $\gamma\gamma$ collisions, L3 provided further evidence for the existence of the $\eta(1475)$ and the $f_1(1420)$, but no evidence of the $\eta(1405)$. This presents the possibility that the $\eta(1405)$ consists of gluonic content because it is not seen in purely electromagnetic interactions (Vorobiev, 2007). CLEO does not confirm the results of L3, but the upper limits provided still suggest that $\eta(1405)$ has large gluonic content (Ahohe *et al.*, 2005).

The $E852$ experiment out of Brookhaven provides important results for comparison to the results presented from this analysis. The E852 hadroproduction experiment out of Brookhaven used a pion beam to provide evidence for the existence of pseudoscalar and axial vector mesons in the 1.3 to 1.5 GeV mass region that decay to $K\bar{K}\pi^0$. It identified the $\eta(1295)$, $\eta(1416)$, and $\eta(1485)$ psuedoscalar resonances, and the $f_1(1285)$ and $f_1(1420)$ axial vector resonances. Invariant mass peaks identified in the GlueX data show evidence of these resonances in $KK\pi^0$, but PWA is necessary to separate the overlapping states by identifying their J^{PC}. E852 also denied the existence of a $C(1480)$ meson decaying $\phi\pi^0$ reported by the Lepton-F group. The decay may be explained as a molecule, since the decay mode is OZI suppressed. From E852, kinematically fit results of $\pi^- p \to K\bar{K}\pi^0 n$ events, peaks are discernible for $\phi(1020) \to K^+K^-$ and both charged states of the K^* meson decaying $K\pi$. Partial wave analysis of these events provided evidence of $\eta(1295)$, $f_1(1285)$, and $\eta(1416)$ decaying $a_0(980)\pi^0$. It also shows evidence of $\eta(1416)$, $\eta(1485)$, and $f_1(1420)$ decaying $K^*(892)\bar{K}$ (Adams *et al.*, 2001).

Two conclusions can be made under the assumption that the $\eta(1295)$, $\eta(1405)$, and $\eta(1475)$ exist. If the $\eta(1295)$ and $\eta(1475)$ exist, then they are the first radial excitations of the η and η', respectively. Furthermore, it can be argued that the $\eta(1475)$ is the $s\bar{s}$ contribution to the 0^{-+} nonet. The second conclusion based on the same assumption that the $\eta(1295)$ and $\eta(1475)$ exist is that the $\eta(1405)$ is not a meson, but a 0^{-+} glueball. This is supported by the fact that it is not seen in the $\gamma\gamma$ collisions of L3 and by the upper limits provided by CLEO. Although the content of these meson states is supported by the flux tube model, it is not supported by lattice gauge theory (Gutsche *et al.*, 2009).

The photoproduction of states decaying $K^*\bar{K}$ is of great interest in the search for hybrid mesons. Theoretically, it is believed that the η_1' hybrid meson candidate

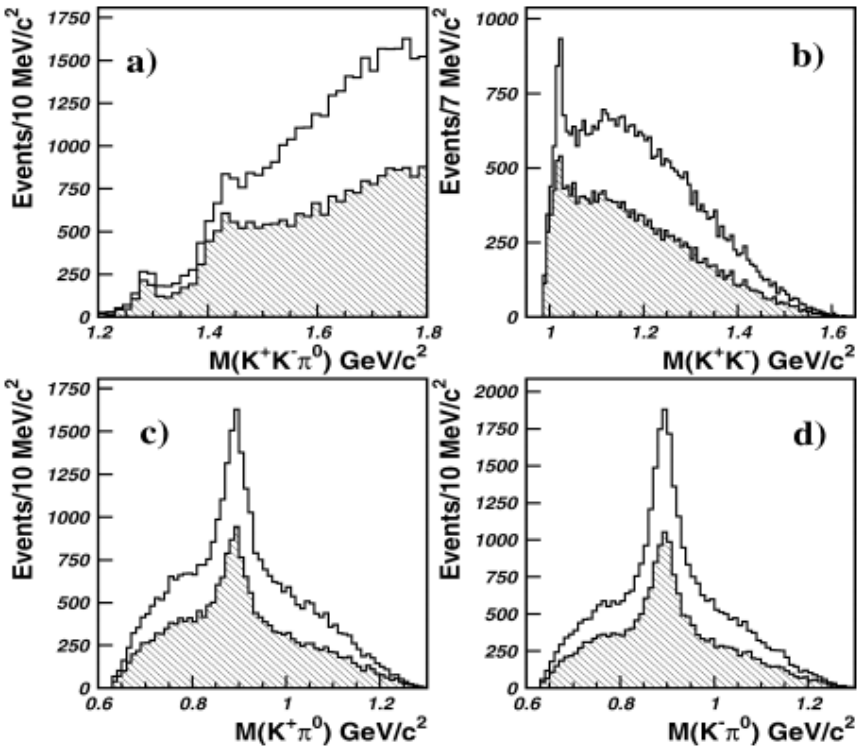

Figure 1.3: E852 invariant mass for (a) $K^+K^-\pi^0$, (b) K^+K^-, (c) $K^+\pi^0$, and (d) $K^-\pi^0$ where shaded regions include a $|t| > 0.1$ GeV^2 constraint. (a) shows evidence for resonances ∼1.3 GeV and ∼1.45 GeV. (b) shows evidence of an intermediate ϕ resonance. (c) and (d) show evidence of $K^{*\pm}(892)$ resonances, respectively (Adams *et al.*, 2001).

with a predicted mass ∼2.3 GeV will decay through $K^*\bar{K}$. Since this hybrid meson candidate belongs to the 1^{-+} nonet, evidence of this resonance would not only help solidify the results reported for the $\pi_1(1600)$, but also help confirm the existence of the $\pi_1(1600)$. Beyond the η_1' with $J^{PC} = 1^{-+}$, the $K^*\bar{K}$ decay mode is relevant to search for hybrid meson candidates with non-exotic quantum numbers (Meyer and Swanson, 2015).

1.4.2 Angular distribution

The angular distributions used by the partial wave analysis to determine the spin quantum numbers of a meson decaying into $K^*(892)\bar{K}$ are defined following

Particle	$I^G(J^{PC})$	Decays	Mass (MeV)	Width (MeV)
$b_1(1235)$	$1^+(1^{+-})$	$K^{*\pm}K^{\mp}\dagger$	1229.5 ± 3.2	142 ± 9
$a_1(1260)$	$1^-(1^{++})$	$KK\pi\dagger / K^*K\dagger$	1230 ± 40	$250 - 600$
$f_2(1270)$	$0^+(2^{++})$	$K^0K^-\pi^+ + c.c.$	1275.5 ± 0.8	$186.7 \pm 2.2/2.5$
$f_1(1285)$	$0^+(1^{++})$	$KK\pi/K^*K\star/a_0(980)\pi(E852)$	1281.9 ± 0.5	22.7 ± 1.1
$\eta(1295)$	$0^+(0^{-+})$	$a_0(980)\pi(E852)$	1294 ± 4	55 ± 5
$\eta(1405)$	$0^+(0^{-+})$	$KK\pi\dagger/K^*K^{\dagger}/a_0(980)\pi(E852)$	1408.8 ± 1.8	51.0 ± 2.9
$f_1(1420)$	$0^+(1^{++})$	$KK\pi\ddagger/K^*K\ddagger$	1426.4 ± 0.9	54.9 ± 2.6
$\rho(1450)$	$1^+(1^{--})$	$K^*K + c.c.*$	1476 ± 4	85 ± 9
$\eta(1475)$	$0^+(0^{-+})$	$KK\pi\dagger/K^*K\dagger/a_0(980)\pi\dagger$	1475 ± 4	90 ± 9
$\eta_2(1645)$	$0^+(2^{-+})$	$KK\pi\dagger/K^*K\dagger$	1617 ± 5	181 ± 11
$\pi_2(1670)$	$1^-(2^{-+})$	$K*K + c.c.$	1672.2 ± 3.0	260 ± 9
$\phi(1680)$	$0^-(1^{--})$	$K^*K + c.c.\ddagger/K^0_SK\pi\dagger$	1680 ± 20	150 ± 50
$\rho_3(1690)$	$1^+(3^{--})$	$K\bar{K}\pi$	1688.8 ± 2.1	161 ± 10
$\rho(1700)$	$1^+(1^{--})$	$K^*K + c.c.\dagger$	1720 ± 20	250 ± 100
$\pi(1800)$	$1^-(0^{-+})$	$K^*_0(1430)K^-\dagger/K^*K^-\star$	$1810 \pm 9/11$	$215 \pm 7/8$
$\phi(1850)$	$0^-(3^{--})$	$K^*K + c.c.\dagger$	1854 ± 7	$87 \pm 28/23$
$\phi(2170)$	$0^-(1^{--})$	$K^{*0}K^{\pm}\pi^{\mp}\star$	2160 ± 80	125 ± 65

Table 1.1: Meson states that decay to $K^+K^-\pi^0$ final states as presented by the P.D.G. Marker in the table are as follows: no marker - defined branching fraction, $*$ - possibly seen, † - seen, ‡ - dominant, $\star$ - not seen (Group *et al.*, 2020).

the formalism of A. Atkinson (Atkinson *et al.*, 1984). It begins by defining two sets of angles, $\Omega = (\theta, \phi)$ and $\Omega_H = (\theta_H, \phi_H)$, where Ω describes the $K^*(892)$ in the resonance's helicity frame and Ω_H describes the $\bar{K}$ in the vector-meson's helicity frame. According to the helicity formalism, the z-direction is defined as the unit vector along the direction of travel of the resonance in the center-of-mass frame (C.M.) of the system. Defining the z-direction as $\hat{z}$, the y-direction ($\hat{y}$) is defined normal to the resonance and beam γ directions. In other words, the y-direction is normal to the production plane defined by the meson resonance and the incident beam directions. To produce a right-handed system, the x-direction is defined by the cross product of $\hat{y}$ and $\hat{z}$. The initial coordinate system is defined as

$$\hat{z} = \frac{\mathbf{p}_{K^*\bar{K},C.M.}}{|\mathbf{p}_{K^*\bar{K},C.M.}|} \tag{1.3}$$

$$\hat{y} = \frac{\mathbf{p}_\gamma \times \hat{z}}{|\mathbf{p}_\gamma \times \hat{z}|} \tag{1.4}$$

$$\hat{x} = \hat{y} \times \hat{z}, \tag{1.5}$$

where $\mathbf{p}_{K^*\bar{K},C.M.}$ is the 3-momentum of the resonance in the C.M. frame and $\mathbf{p}_\gamma$ is the 3-momentum of the beam photon.

To determine the direction of travel of the $K^*(892)$ in this coordinate system, a boost along the z-direction is performed to move into the meson resonance's rest frame. Using the 3-momentum vector of the $K^*(892)$ in the resonance rest frame ($\mathbf{p}_{K^*,Res.}$), θ and ϕ can be determined by

$$\cos\theta = \frac{\mathbf{p}_{K^*,Res.} \cdot \hat{z}}{|\mathbf{p}_{K^*,Res.}|} \tag{1.6}$$

$$\phi = \tan^{-1}\left(\frac{\mathbf{p}_{K^*,Res.} \cdot \hat{y}}{\mathbf{p}_{K^*,Res.} \cdot \hat{x}}\right). \tag{1.7}$$

To determine the second set of angles, describing the decay of the K^*, a new coordinate system is established for the helicity frame of the photoproduced meson resonance. Specifically, the z-direction ($\hat{z}_H$) is defined as the direction of the $K^*(892)$ in the rest frame of the meson resonance. The decay plane of the resonance is establish by the z-directions of the resonance and the $K^*(892)$ helicity frames, such that the y-direction ($\hat{y}_H$) is perpendicular to this plane. As before, the x-direction ($\hat{x}_H$) is defined to establish a right handed coordinate system. This coordinate system is defined as

$$\hat{z}_H = \frac{\mathbf{p}_{K^*,Res.}}{|\mathbf{p}_{K^*,Res.}|} \tag{1.8}$$

$$\hat{y}_H = \frac{\hat{z} \times \hat{z}_H}{|\hat{z} \times \hat{z}_H|} \tag{1.9}$$

$$\hat{x}_H = \hat{y}_H \times \hat{z}_H, \tag{1.10}$$

Similar to the determination of $\cos\theta$ and ϕ, $\cos\theta_H$ and ϕ_H are defined as

$$\cos\theta_H = \frac{\mathbf{p}_{K,Vec.} \cdot \hat{z}_H}{|\mathbf{p}_{K,Vec.}|} \tag{1.11}$$

$$\phi_H = \tan^{-1}\left(\frac{\mathbf{p}_{K,Vec.} \cdot \hat{y}_H}{\mathbf{p}_{K,Vec.} \cdot \hat{x}_H}\right), \tag{1.12}$$

where $\mathbf{p}_{K,Vec.}$ is the momentum of a kaon decaying from the K^* in the vector meson's rest frame.

Since a polarized photon beam is used in the experiment, a fifth angle (Φ) is established to describe the direction of the polarization with respect a vector normal to the production plane. First, a photon beam polarization vector is established in the lab frame using the polarization angle ϕ_{pol} by

$$\epsilon' = \cos\phi_{pol}\hat{i} + \sin\phi_{pol}\hat{j}. \tag{1.13}$$

The initial coordinate system used to determine the Ω angles defines the y-direction as perpendicular to the production plane. The projection of $\hat{y}$ onto ϵ' and the projection of $\mathbf{p}_{\gamma,C.M.}$ onto $\epsilon' \times \hat{y}$ define the legs of the right triangle for determining Φ such that

$$\Phi = \tan^{-1}\left(\frac{\frac{\mathbf{p}_{\gamma,C.M.}}{|\mathbf{p}_{\gamma,C.M.}|} \cdot (\epsilon' \times \hat{y})}{\hat{y} \cdot \epsilon'}\right), \tag{1.14}$$

where $\mathbf{p}_{\gamma,C.M.}$ is the incident photon beam's momentum in the C.M. frame of the system.

1.4.3 Intensity function in helicity basis

A cross section (σ) for a given process is defined as the number of interaction per unit time per target particle over the incident flux. With respect to particular kinematic variables, the intensity for the production of meson states can be defined using the differential cross section. The intensity is

$$I(\Omega, \Omega_H, \Phi) \equiv \frac{d\sigma}{dt dm_{K^*\bar{K}} d\Omega d\Omega_H d\Phi}, \tag{1.15}$$

where Ω is the direction of the K^* in the system's helicity frame, Ω_H is the direction of the K in the photoproduced meson's helicity frame, Φ the direction of the photon beam polarization with respect to the production plane, $m_{K^*\bar{K}}$ is the mass of the meson resonance, and t is the Mandelstam momentum transfer, as outlined in Section 1.4.2.

Using the formalism introduced by V. Mathieu (Mathieu *et al.*, 2019), and expanded by M. Shepherd (Shepherd, 2019) and J. Stevens (Stevens, 2021), the intensity can be defined in helicity space. For polarized beams, the intensity is

$$I(\Omega, \Omega_H, \Phi) = I^0(\Omega, \Omega_H) - P_\gamma I^1(\Omega, \Omega_H)\cos(2\Phi) - P_\gamma I^2 \sin(2\Phi), \tag{1.16}$$

where P_γ is the degree of the linear polarization of the incident photon beam. Each I in Equation 1.16 can be defined in terms of decay amplitudes providing

$$I^0(\Omega, \Omega_H) = \frac{\kappa}{2} \sum_\lambda A_\lambda(\Omega, \Omega_H) A^*_\lambda(\Omega, \Omega_H) \tag{1.17}$$

$$I^1(\Omega, \Omega_H) = \frac{\kappa}{2} \sum_\lambda A_{-\lambda}(\Omega, \Omega_H) A^*_\lambda(\Omega, \Omega_H) \tag{1.18}$$

$$I^2(\Omega, \Omega_H) = i\frac{\kappa}{2} \sum_\lambda \lambda A_{-\lambda}(\Omega, \Omega_H) A^*_\lambda(\Omega, \Omega_H), \tag{1.19}$$

where A defines the decay amplitudes and λ defines the photon beam helicity, of which $+, -$ terms are expected. Substituting the definitions of I^0, I^1, and I^2 in terms of the decay amplitudes into Equation 1.16, summing over helicity states, and applying Euler's formula, the intensity becomes

$$\begin{aligned} I(\Omega, \Omega_H, \Phi) = \frac{\kappa}{2}[&A_-(\Omega, \Omega_H) A^*_-(\Omega, \Omega_H) + A_+(\Omega, \Omega_H) A^*_+(\Omega, \Omega_H) \\ &- P_\gamma (A_-(\Omega, \Omega_H) A^*_+(\Omega, \Omega_H) + A_+(\Omega, \Omega_H) A^*_-(\Omega, \Omega_H)) e^{i2\Phi}]. \end{aligned} \tag{1.20}$$

If the decay amplitudes are defined with rotations of Φ about the photon beam direction as $\tilde{A}_\pm(\Omega, \Omega_H, \Phi) = e^{\mp i\Phi} A_\pm(\Omega, \Omega_H, \Phi)$, the rotation is distributed through all decay amplitude terms. With further algebraic manipulation, the intensity is defined by

$$\begin{aligned} I(\Omega, \Omega_H, \Phi) = \frac{\kappa}{4}[&(1 - P_\gamma)|\tilde{A}_+(\Omega, \Omega_H, \Phi) + \tilde{A}_-(\Omega, \Omega_H, \Phi)|^2 \\ &+ (1 + P_\gamma)|\tilde{A}_+(\Omega, \Omega_H, \Phi) - \tilde{A}_-(\Omega, \Omega_H, \Phi)|^2]. \end{aligned} \tag{1.21}$$

The decay amplitudes are expanded in terms of partial waves

$$A_\lambda = \sum_i \sum_m T^i_{\lambda,m} \sum_\lambda D^{J_i *}_{m,\lambda}(\Omega) F^i_\lambda D^{1*}_{m,\lambda}(\Omega_H), \tag{1.22}$$

where T are the partial wave amplitudes, D are Wigner D-functions, and F is a decay amplitude of an intermediate state.

1.4.4 The decay amplitude

The decay amplitude defined in Equation 1.22 used to determine the intensity is defined in terms of two rotations on spin-space. Let B be the matrix element associated with the two rotations of interest:

$$B \equiv \langle j_1 m_1 j_2 m_2 | R^{(1)} R^{(2)} | J m \rangle, \tag{1.23}$$

such that $R^{(1)}$ and $R^{(2)}$ act on $|j_1 m_1\rangle$ and $|j_2 m_2\rangle$, respectively. For the vector-pseudoscalar decay of interest, rotations with respect to the angles θ, ϕ, θ_H, and ϕ_H are defined in the resonance and vector meson frames. As a result, $R^{(1)}$ is the roation in the resonance frame, $R_r(\theta, \phi)$, and $R^{(2)}$ is the rotation in the vector meson frame, $R^{(2)}_v R^{(2)}_r$. Therefore, the matrix element can be written as

$$B = \langle j_1 m_1 j_2 m_2 | R^{(1)}_r R^{(2)}_v R^{(2)}_r | J m \rangle. \tag{1.24}$$

If a complete set of spin projections with respect to j_1 and j_2 is introduced to Equation 1.24, it can be written in terms of Wigner D-functions.

The Wigner D-functions are related to the spin-weighted spherical harmonics, operating to move between frames of a meson state's sequential decay using rotations

on the spin space. Section 1.4.2 defines Euler angles (α, β, γ) for which the Wigner D-function is defined

$$\begin{aligned} D^J_{m\lambda} &= \langle Jm|e^{-i\alpha J_z}e^{-i\beta J_y}e^{-i\gamma J_z}|J\lambda\rangle \\ &= e^{-im\alpha}d^J_{m\lambda}e^{-i\lambda\gamma}, \end{aligned} \tag{1.25}$$

where $d^J_{m\lambda} = \langle Jm|e^{-i\beta J_y}|J\lambda\rangle$ or Wigner D-small. The convention of this work assumes $\gamma = 0$ because a particle's direction only needs the polar coordinates (α, β) to be completely defined (Salgado and Weygand, 2014).

With the complete set introduced, the matrix element is

$$\begin{aligned} B &= \langle j_1 m_1 j_2 m_2|R^{(1)}_r R^{(2)}_v R^{(2)}_r| \left[\sum_{m'_1}\sum_{m'_2}|j_1 m'_1 j_2 m'_2\rangle\langle j_1 m'_1 j_2 m'_2|\right] Jm\rangle \\ &= \sum_{m'_1}\sum_{m'_2}\langle j_1 m_1|R^{(1)}_r|j_1 m'_1\rangle\langle j_2 m_2|R^{(2)}_v R^{(2)}_r|j_2 m'_2\rangle\langle j_1 m'_2 j_2 m'_2|Jm\rangle, \end{aligned} \tag{1.26}$$

where the first term in the sum is the Wigner D-function, $D^{j_1}_{m'_1 m'_2}(R_r)$. A second complete set can be introduced

$$\begin{aligned} B &= \sum_{m'_1}\sum_{m'_2} D^{j_1}_{m'_1 m'_2}(R_r)\langle j_2 m_2|R^{(2)}_v \left[\sum_{m''_2}|j_2 m''_2\rangle\langle j_2 m''_2|\right] R^{(2)}_r|j_2 m'_2\rangle\langle j_1 m'_2 j_2 m'_2|Jm\rangle \\ &= \sum_{m'_1}\sum_{m'_2}\sum_{m''_2} D^{j_1}_{m'_1 m'_2}(R_r)\langle j_2 m_2|R^{(2)}_v|j_2 m''_2\rangle\langle j_2 m''_2|R^{(2)}_r|j_2 m'_2\rangle\langle j_1 m'_2 j_2 m'_2|Jm\rangle. \end{aligned} \tag{1.27}$$

which introduces two more Wigner D-functions to the decay amplitude:

$$B = \sum_{m'_1}\sum_{m'_2}\sum_{m''_2} D^{j_1}_{m'_1 m'_2}(R_r) D^{j_2}_{m''_2 m'_2}(R_r) D_{m'_2 m''_2}(R_v)\langle j_1 m'_2 j_2 m'_2|JM\rangle. \tag{1.28}$$

The two rotations of j_1 and j_2 in the resonance frame can be combined to a single rotation on J' using the Clebsch-Gordon series, specifically

$$D^{j_1}_{m_1 m_1'} D^{j_2}_{m_2'' m_2'} = \sum_{J'} \sum_{M'} \sum_{m''} \langle j_1 m_1 j_2 m_2'' | J' m' \rangle \langle j_1 m_1' j_2 m_2' | J' m'' \rangle D^{J'}_{m' m''}(R_r),$$

which gives

$$B = \sum_{m_1'} \sum_{m_2'} \sum_{m_2''} \sum_{J'} \sum_{m'} \sum_{m''} \langle j_1 m_1 j_2 m_2'' | J' m' \rangle \langle j_1 m_1' j_2 m_2' | J' m'' \rangle \langle j_1 m_1' j_2 m_2' | J m \rangle D^{J'}_{m' m''}(R_r) D^{j_2}_{m_2'' m_2'}(R_v). \quad (1.29)$$

The completeness relation

$$\delta_{J' J} \delta_{m'' m} = \sum_{m_1'} \sum_{m_2'} \langle j_1 m_1' j_2 m_2' | J' m'' \rangle \langle j_1 m_1' j_2 m_2' | J m \rangle$$

simplifies the decay amplitude to its final expression, such that is only involves a rotation on spin space in the meson resonance and the vector meson's rest frame. The decay amplitude is

$$B = \sum_{m_2'} \sum_{m_2''} \sum_{m'} \langle j_1 m_1 j_2 m_2'' | J m' \rangle D^{J}_{m' m}(R_r) D^{j_2}_{m_2'' m_2'}(R_v), \quad (1.30)$$

from which F in Equation 1.22 is defined as

$$F = \sum_{m_2'} \sum_{m_2''} \sum_{m'} \langle j_1 m_1 j_2 m_2'' | J m' \rangle. \quad (1.31)$$

1.4.5 Intensity function in reflectivity basis

The intensity function developed to this point is built in terms of a helicity basis. Due to the $e^{im\phi}$ term in the amplitudes, the helicity is not an eigenstate of parity. Therefore, it is necessary to transform to the reflectivity basis, a quantum number representing the mirror reflection through the production plane. As a result, an explicit symmetry with parity is introduced, which assists in investigating the parity conserving strong interaction (Salgado and Weygand, 2014).

The reflectivity amplitudes for a vector-pseudoscalar decay are related to the helicity amplitudes by

$$ {}^{(\epsilon)}T^i_m = \frac{1}{2}(T^i_{+1,m} - \epsilon\tau_i(-1)^m T^i_{-1,-m}), \tag{1.32} $$

where ϵ is the reflectivity quantum number and τ is the naturality of the meson resonance. Both ϵ and τ have possible values of ± 1, and the sign of the reflectivity defines the sign of the spin projection m. This relationship is used to transform the decay amplitudes from the helicity basis to the reflectivity basis (Stevens, 2021).

Beyond the transformation from the helicity basis to the reflectivity basis, it is necessary to convert to a sum over spin flip and non-flip. This introduces the J^P quantum number necessary to identify spin-parity of particles. In order to convert the sum, the parity invariance is defined as

$$ {}^{(\epsilon)}T^i_{m;-\lambda_1-\lambda_2} = \tau_i\epsilon(-1)^{\lambda_1-\lambda_2}{}^{(\epsilon)}T^i_{m;\lambda_1\lambda_2}, \tag{1.33} $$

where $[J_i]^{(\epsilon)}_{m,0} =^{(\epsilon)} T^i_{m;+-}$ and $[J_i]^{(\epsilon)}_{m,1} =^{(\epsilon)} T^i_{m;++}$ define the spin flip and non-flip amplitudes, respectively (Stevens, 2021). This information is used to build the final form of the intensity function

$$I(\Omega,\Omega_H,\Phi) = 2\kappa\sum_k[(1-P_\gamma)[|\sum_{i_N,m}[J_i^N]^{(+)}_{m,k}Im(Z)+\sum_{i_U,m}[J_i^U]^{(-)}_{m,k}Im(Z)|^2$$
$$+|\sum_{i_N,m}[J_i^N]^{(-)}_{m,k}Re(Z)+\sum_{i_U,m}[J_i^U]^{(+)}_{m,k}Re(Z)|^2]+(1+P_\gamma)[|\sum_{i_N,m}[J_i^N]^{(-)}_{m,k}Im(Z)$$
$$+\sum_{i_U,m}[J_i^U]^{(+)}_{m,k}Im(Z)|^2+|\sum_{i_N,m}[J_i^N]^{(+)}_{m,k}Re(Z)+\sum_{i_U,m}[J_i^U]^{(-)}_{m,k}Re(Z)|^2]]. \quad (1.34)$$

1.5 Summary

With the historical context of $K\bar{K}\pi$ system, there is a clear motivation for analyzing $\gamma p \to pK^+K^-\gamma\gamma$ events in GlueX. This work can attempt to answer two questions:(1) Do two psuedoscalar mesons exist in the 1400 MeV region seen in production mechanisms: $\pi^- p$, radiative $J/\psi(1S)$ decay, and $\bar{p}p$ annihilation at rest? (2) What additional states can be found in the mass range used in this analysis? To begin to answer these questions, the GlueX experiment must be discussed.

Chapter 2

EXPERIMENTAL TECHNIQUES

This chapter discusses the experimental techniques used in the search for photoproduced hybrid mesons off a proton target. Probing final states that may arise from hybrid meson candidates is made possible by the CEBAF upgrade, which allows the accelerator to provide electrons with energies up to 12 GeV that can be utilized to produce 11.6 GeV polarized photons via Bremsstrahlung off a diamond. The incident photon four-vector information is determined using a photon tagging system comprised of a tagger microscope (TAGM) and tagger hodoscope (TAGH). Downstream of the tagging system, the triplet polarimeter (TPOL) detects ejected atomic electrons from the triplet process within a beryllium foil to determine the polarization of the incident photon beam. Photon interaction with the beryllium foil also produces electron-positron pairs detected by a pair spectrometer (PS) used in determining the flux of the incident photon beam. Reconstruction of the decay products from photon interactions with protons in the liquid hydrogen target is accomplished using information provided by the start counter (ST), central drift chambers (CDC), forward drift chambers (FDC), barrel calorimeter (BCAL), time of flight (TOF), and forward calorimeter (FCAL). Future runs will include the detection of internally reflected Cherenkov light via the DIRC detector, which will improve identification of kaon final states.

2.1 The continuous electron beam accelerator facility

In the 1980s it became clear that a new accelerator was necessary to investigate a relatively unexplored energy regime. Specifically, physicists are interested in under-

standing nucleon based matter, and the quark-gluon structure of mesons and baryons. CERN and other experiments have passed over this energy region in search of new physics and to assist in the attempt to develop a universal theory. However, our understanding of the strong interaction is incomplete and the continuous electron beam accelerator facility (CEBAF) assists in uncovering properties of hadronic matter.

The desires for CEBAF were outlined in the nuclear long-range plans of the Nuclear Science Advisory Committee (NSAC) of 1979 and 1983, resulting in its approval in the late 1980s. CEBAF construction began in 1989 with commissioning throughout the early 1990s. In 1998, CEBAF simultaneously provided an electron beam with a maximum energy of 4 GeV to three experimental halls, which was increased to 6 GeV in 2000 with developments in superconducting radio-frequency (srf) cavities (Leemann *et al.*, 2001). The desire for further CEBAF upgrades to bring the energy limit to 12 GeV and the construction of a fourth experimental hall to map the light meson spectrum was approved in 2008. By 2016, the 12 GeV era began with delivery of beam to three experimental halls, and the first physic's data collected in hall D by the GlueX collaboration (Freyberger, 2015). Plans to double CEBAF's maximum energy to 24 GeV exist, which will be critical for near threshold production of charmonium states and to fill an energy gap that will be created by the implementation of an electron-ion collider being built at Brookhaven National Laboratory (BNL).

2.1.1 The accelerator

Since the 12 GeV upgrade, CEBAF's electron beam now supports experiments conducted in four experimental halls. It begins with one of two DC high voltage gallium arsenide (GaAs) photoguns generating an electron beam by way of the photoelectric effect, accomplished by illuminating a GaAs photocathode with 780 nm light pulsed at a 1497 MHz repetition rate. The beam is a continuous wave with 1497 MHz

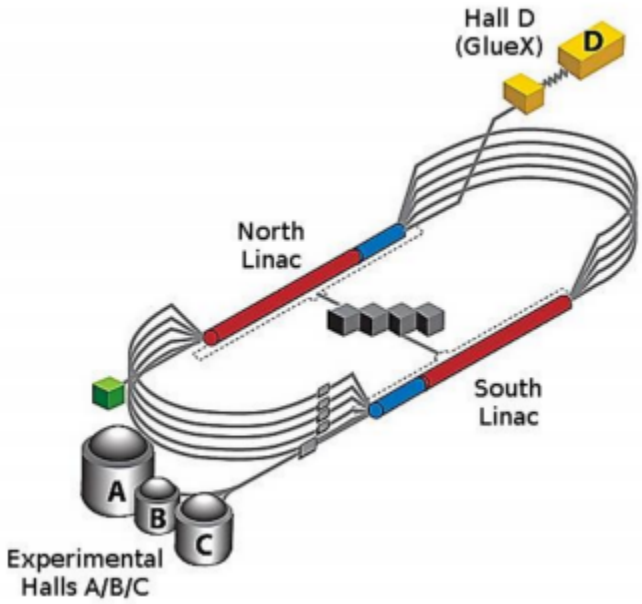

Figure 2.1: Model of the CEBAF accelerator after the 12 GeV upgrade, showing the north and south linacs, the hall D tagger and spectrometer buildings, and the Central Helium Liquefier (CHL) buildings at the center of the racetrack. The original experimental halls are also shown.

fundamental frequency achieved by combining multiple sub-harmonic beams, with frequencies 499 MHz or 249.5 MHz. Electrons over a small energy range are selected using vertical and horizontal Wien filters before being chopped and bunched to allow only distinctly phased sub-harmonic beams to pass. After accelerating to 123 MeV, the carefully constructed beam is injected into the main accelerator.

CEBAF is an ∼1.4 km racetrack-shaped electron accelerator consisting of two linear accelerators (linacs) and ten recirculating arcs. It is capable of delivering an 11 GeV electron beam from 5 passes to halls A, B, and C, and a 12 GeV electron beam from 5.5 passes to hall D. These energies are indicative of a ∼2.2 GeV energy gain per pass, or ∼1.1 GeV per linac (See Figure 2.1). The north and south linacs consist of 25 cryomodules each, 40 from the 6 GeV era and 10 added for the 12 GeV era. Each cryomodule contains eight superconductive radio frequency (RF) cavities used to accelerate electrons through the linacs. The superconductive RF cavities consist

of seven niobium cells supercooled to 2 K using 400 gallons of liquid helium provided by the Central Helium Liquifier (CHL). Consistent with the generated electron beam, the niobium cells operate at a natural frequency of 1497 MHz* .

At the end of the north and south linacs are RF spreaders and recombiners that take the beam from one linac and recirculate it to the opposing linac. This is accomplished using a combination of dipoles to complete the 180° bend, such that higher arcs receive the lower energy electrons and lower arcs receive the higher energy electrons. After a number of passes that are less than five, a hall can receive the beam using a 499 MHz RF separator. However, the fifth pass uses a 750 MHz separator to deliver a 249.5 MHz beam to hall D and to allow for four hall operation of CEBAF. These conditions supply an electron beam bunch to hall D every 4.008 ns. That electron beam is then utilized to generate a secondary photon beam for GlueX (Leemann *et al.*, 2001; Freyberger, 2015; Reece, 2016).*

2.2 The GlueX Bremsstrahlung photon beam line

The GlueX experiment uses a polarized photon beam incident on a liquid hydrogen target to photoproduce hadronic forms of matter. This section will outline methods used to characterize the GlueX Bremsstrahlung photon beam, with discussion of detectors as they would appear while an observer moves down the beam line. To create the polarized photon beam, the accelerator's electron beam is passed through a diamond held by a goniometer upstream of the tagger. As described in Section 1.3.1, the interaction of the electrons with the atomic nuclei of the diamond creates photons from the lost kinetic energy of the electrons. The photon beam continues downstream on its way to the collimator cave, while the electron beam is subject to

* The original RF cavities consist of five niobium cells, 40 of which are still in use. If these were upgraded to the seven cell version, a maximum energy of 24 GeV could be achieved by CEBAF.

* The bunch timing is determined by 1/249.5 MHz = 4.008 ns.

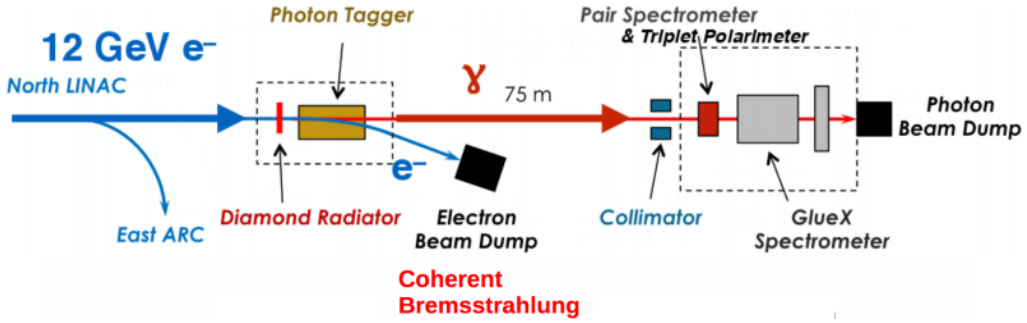

Figure 2.2: The GlueX beam line with downstream to the right. This shows the CEBAF electron beam incident on the diamond radiator generating a photon beam to be delivered to the GlueX spectrometer. The radiated electrons are tagged by the photon tagger and sent to the electron beam dump.

the tagger magnet, resulting in the electron beam taking a curved path towards the tagger. As the photon beam travels downstream, it becomes incident on Beryllium foil. Discussed in Section 1.3.2, the interaction of the photons with the atomic nuclei or an atomic electron can result in pair or triplet photoproduction, respectively. In the case of tiplet photoproduction, the recoil electrons interact with a silicon strip detector used for polarization determination. The photoproduced pairs travel further downstream, become subject to the pair spectrometer magnet, and interact with the pair spectrometer. After the pair spectrometer, the photon beam is incident on a liquid hydrogen target, the details of which will be discussed alongside the GlueX spectrometer.

2.2.1 Tagger hall

The accelerator's electron beam can interact with a diamond radiator and undergo a Bremsstrahlung process that generates a photon beam in the GlueX tagger hall. The electrons become subject to the tagger magnet's magnetic field and take a curved path to the tagger hodoscope (TAGH), tagger microscope (TAGM), or to the beam dump. The TAGH and TAGM instrumentation measure the incident photon beam's energy and timing.

Diamond

GlueX's photon beam is generated from a Bremstrahlung process off a diamond radiator held by a goniometer in the tagger hall. The experiment calls for a photon beam polarization near 40%, which necessitates a diamond with Miller indices $< 001 >$, mosaic spread less than 20 μrad r.m.s. (determined by rocking curve width), and thickness less than 20 ± 5 μm. However, the GlueX experiment has used a $\sim$50 μm thick, 5.6 mm $\times$ 5.6 mm diamond wafer, since no 20 μm thick diamond have met the standards for the experiment (Barbosa *et al.*, 2014). As determined by TPOL, the measured polarization is $\sim$35% with the $\sim$50 μm diamond Dugger *et al.* (2017).

Tagger magnet

The tagger magnet consists of two dipole magnets in series separated by 3.0 cm producing a 1.5 T magnetic field. The 38 ton magnets provide a 9.0 m focal plane, which is consistent with 65% coverage of possible electron energies coincident on the tagger. This magnet arrangement means detected electron energies subject to the first magnet will fall within $1 - 4.3$ GeV, from photons with an energy range of $7.7 - 11$ GeV. For the second magnet, the energies ranges are $4.3 - 9$ GeV and $3 - 7.7$ GeV, respectively (Barbosa *et al.*, 2014).

Tagger hodoscope

The tagger hodoscope (TAGH) is comprised of scintillating detectors used to tag photons outside the peak region of the coherent Bremsstrahlung process. Specifically, TAGH monitors the low and high energy photons created by incoherent Bremsstrahlung or from less intense coherent Bremsstrahlung that create parasitic peaks in the photon energy distribution. It was built to surround the coherent-peak energy region with an intentional gap for the higher resolution TAGM. Figure 2.3 shows the arrangement of

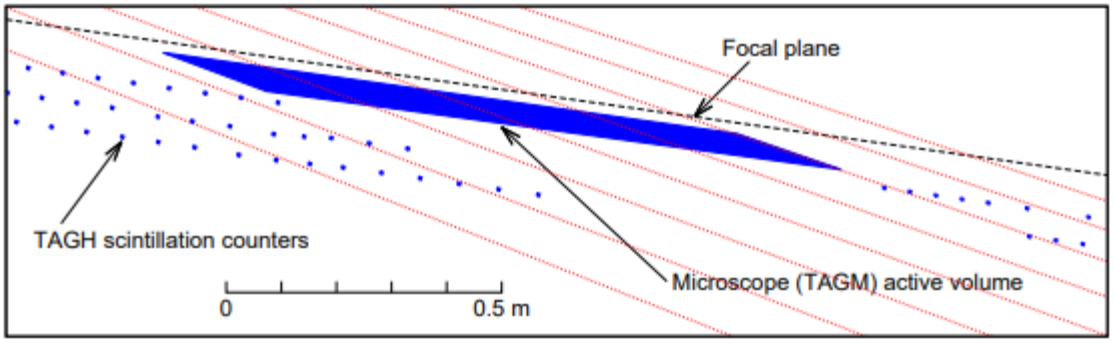

Figure 2.3: Schematic of the tagger hodoscope with respect to the tagger microscope. The TAGH counters are arranged in three columns such that the electrons are incident normal to the counters, ensuring complete dispersion coverage. Gaps between counters ensure reduced rates for less stress of hardware (Adhikari *et al.*, 2021).

TAGH around TAGM, with three rows of scintillating counters arranged normal to incident electrons. The ceiling mount of TAGH allows re-positioning of the counters to account for changes to the location of the coherent peak (Adhikari *et al.*, 2021).

Using 222 scintillating counters distributed over 9.25 m, TAGH determines the energy of photons from $3.05 - 8.10$ GeV and $9.10 - 11.78$ GeV with a resolution of $10 - 30$ MeV and timing resolution of 200 ps. Each counter is 6 mm thick with a height of 40 mm constructed from EJ-228 scintillator. The widths vary as one moves downstream from 21 mm to 3 mm and gaps are placed between counters to decrease the detection rate. These widths correspond to an energy range of 8.5 MeV to 30 MeV. The counters are connected to cylindrical acrylic light guides to deliver scintillating light to Hamamatsu R9800 photomultiplier tubes (Barbosa *et al.*, 2014).

Tagger microscope

The tagger microscope (TAGM) is a scintillating detector used to tag photons within the energy region of the coherent Bremsstrahlung peak. This energy region of the photon beam consists of polarized photons which are critical to the success of the GlueX experiment and its search for hybrid mesons. As a result, TAGM is a high

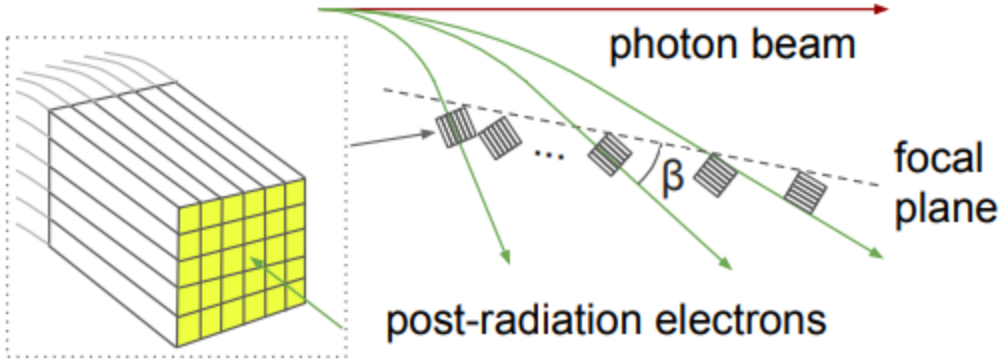

Figure 2.4: Tagger microscope's design characteristics showing that bundles consist of 6×5 dense arrays (left) oriented with respect to the cross angle (β) to ensure electrons are incident normal to the face of the bundle (right) (Adhikari *et al.*, 2021).

resolution hodoscope that can be moved to accommodate changes in the primary coherent peak position (Adhikari *et al.*, 2021).

TAGM is divided into 102 energy bins, or columns, along the horizontal, with each column having 5 rows along the vertical, making the TAGM dimensions 102×5. By these dimensions, TAGM consists of 510 2×2 mm^2 square, scintillating fibers packaged into 17 dense arrays with 6 columns. As shown in Figure 2.4, the 6×5 arrays are staggered to cover the dispersion of electrons, similar to TAGH, ensuring they are incident normal to the focal plane. The scintillating fibers are 10 mm long connected to clear light guides that pass scintillating light to Hamatsu S10931-050P silicon photomultiplier tubes. This setup results in a 5 MeV energy resolution and 230 ps timing resolution (Barbosa *et al.*, 2014).

2.2.2 Collimator cave

The collimator cave is directly downstream of the tagger hall in hall D. Instruments within the collimator cave provide a collimated beam with background reduction, and measurements for polarization determination. The collimator cave contains the active collimator, quadrupole magnet, triplet polarimeter. Directly outside the

collimator cave is the pair spectrometer (PS), providing a trigger for the coincidence of lepton pairs and a means for calibrating the tagger from time, energy, and position measurements of the pairs.

Triplet polarimeter

The triplet polarimeter (TPOL) is used to determine the polarization of the incident photon beam. It accomplishes this by measuring the azimuthal distribution of recoil electrons ejected from a beryllium (Be) foil in a triplet photoproduction process (See Section 1.3.2). In this process, recoil electrons will have a fraction of the momentum of the produced pair and a large opening angle (θ). The recoil electrons are detected by a double-sided silicon strip detector (SSD) with 32 azimuthal sectors and 24 concentric rings that provide azimuthal and radial position measurements, respectively. Providing a $\sim$35 cm^2 active area for the recoil electrons, the SSD is statically mounted inside a vacuum chamber downstream of a motorized converter tray that holds a Be foil converter. The ring side of the silicon strip detector is shown in Figure 2.5a housed inside a $12 \times 12 \times 12$ in^3 vacuum chamber.

Outside the vacuum chamber is a preamplifier enclosure that houses the SSD electronics. Signals are passed from the vacuum chamber interior using a feedthrough flange to electronic filters and amplifiers that are utilized to reduce noise and shape the signal, respectively. The SSD electronics are housed in a Faraday cage to further prevent electrical interference from the environment. Figure 2.5b shows the preamplifier enclosure with the feedthrough flange, the amplifiers attached to stands, and the copper lining of the Faraday cage. The signals are distributed from the amplifiers through a distribution box shown in Figure 2.5c, which pass the signals to the readout electronics of the experiment.

As discussed in Section 1.3.2, the triplet photoproduction cross section for a po-

larized beam can be written as a function of the triplet photoproduction cross section for an unpolarized beam. Equation 1.2 further defines the dependence of triplet cross section on a $\cos(2\phi)$ distribution, which is produced by analysis of TPOL data from the sectors of the SSD. Accounting for background contributions from δ-rays, the TPOL azimuthal distribution is fit with $A(1 - B\cos(2\phi))$ to obtain parameter $B = P\Sigma_A$. In this case, Σ_A is the analyzing power used to determine the photon beam polarization obtained from GEANT4 simulation of a $8 - 9$ GeV photon beam incident on a 76.2 μm-thick Be converter using the eight possible QED processes that govern triplet photoproduction (See Figure 2.5d). With the extraction of Σ_A for a particular converter thickness, the incident photon beam polarization is $P = B/\Sigma_A$. Despite the simplicity of the detector and analysis, the rate of triplet photoproduction in experiment is small, making it difficult to determine the polarization with relative statistical uncertainty <1%. Systematic contributions to this measurement are 1.5% (Dugger *et al.*, 2017).

(a)

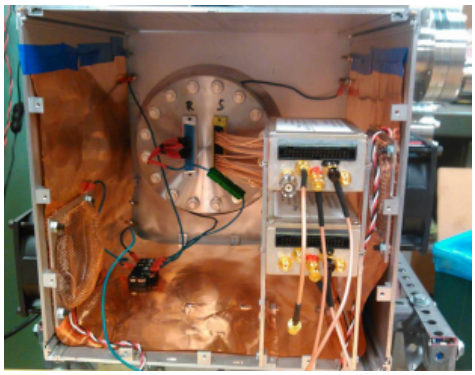

(b)

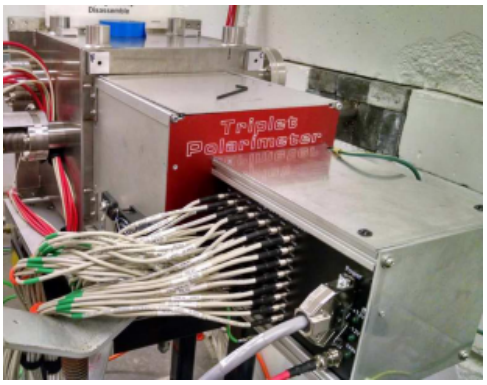

(c)

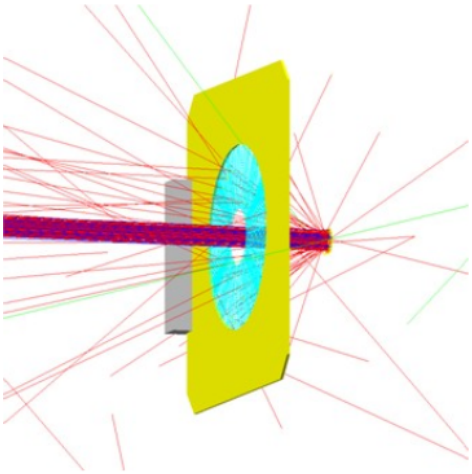

(d)

Figure 2.5: (a) A view inside the vacuum chamber showing the silicon strip detector and the converter tray. (b) A view inside the preamplifier enclosure showing the feedthrough flange, the electronics stand, and the Faraday cage. (c) A view of the distribution box that receives and sends signal to the readout electronics. (d) Image from the simulation of a $8-9$ GeV photon beam incident on a Be converter and the potential interaction of recoil electrons with the silicon strip detector (Dugger *et al.*, 2017).

Pair spectrometer magnet

The pair spectrometer magnet is a 1 m long dipole magnet from Brookhaven National Laboratory. This dipole magnet produces a magnetic field of 1.8 T, ensuring electron-positron pairs move along curved paths through a 1.5 m vacuum chamber (Barbosa *et al.*, 2014).

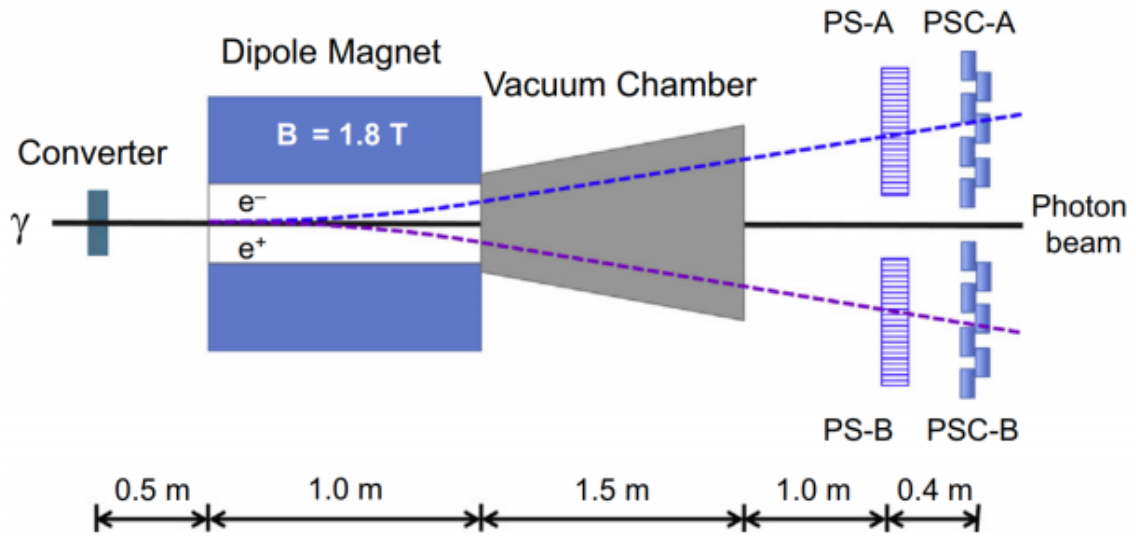

Figure 2.6: Schematic of the GlueX pair spectrometer directly downstream of the collimator cave. The converter to the left is held in the converter tray of TPOL. The dipole magnet separates the pair sending them to specific parts of the PS and PSC for energy determination and coincidence matching with the taggers (Barbosa *et al.*, 2015).

Pair spectrometer

The pair spectrometer is just outside the collimator cave, upstream of the liquid hydrogen target. Electron-positron pairs, created from photon interaction with beryllium nuclei or beryllium atomic electrons (See Section 1.3.2), take curved paths towards two arms left and right of the beam line. Each arm consists of a coarse and fine set of counters, providing 3.0 GeV to 6.2 GeV momentum coverage (Adhikari *et al.*, 2021).

The fine counters are made up of a high-granularity hodoscope (PS) with 145 EJ-212 scintillator tiles optically isolated by 10 μm of aluminum. The tiles vary in thickness between 1 mm for the coherent peak region and 2 mm elsewhere. Scintillating light collected from electron-positron interactions with the PS are passed to two 20 cm square double-clad BCF-92 wavelength-shifting fibers. Furthermore, light is collected for measurement of produced electromagnetic showers with 3 mm $\times$ 3 mm

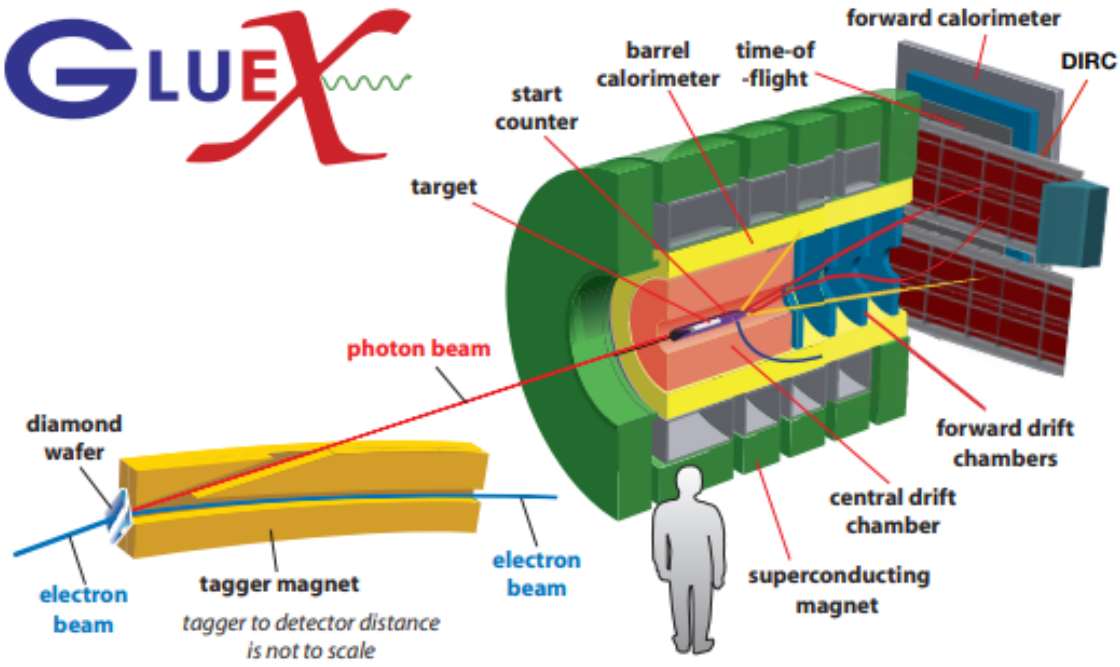

Figure 2.7: Model of the GlueX tagger and GlueX spectrometer, showing the locations of the target, ST, solenoid, BCAL, CDC, FDC, DIRC, FCAL, and TOF to scale (Freyberger, 2015).

Hamatsu surface mount S10931-050P silicon photomultiplier tubes that are processed by a 12-bit multi-channel flash analog-to-digital converter (fADC) with 250 MHz frequency. The PS measures the energy, position, and time of the incident lepton pairs with an efficiency of 20%.

The coarse counters of the pair spectrometer are 40 cm behind the PS. Eight coarse counters per arm are distributed such that lepton pairs will be incident perpendicular to the counters, with corresponding Hamamatsu-R6427-01 PMTs to detect scintillating light produced by the leptons in the counters. The coarse counters use the same fADCs as the fine, but also uses TDCs (time to digital converters). The coincidence of two hits in the two detector arms of the coarse pair spectrometer (PSC) are used as a trigger for the tagger (Barbosa *et al.*, 2014).

Figure 2.8: Photograph of experimental hall D showing the GlueX spectrometer (Freyberger, 2015).

2.3 The GlueX spectrometer

The GlueX spectrometer consists of a straw and multiwire drift chamber, a lead glass and lead scintillator calorimeter, two detectors based off plastic scintillators, and in the future, a Cherenkov light detector. The photon beam incident on the liquid hydrogen target of GlueX, originating from the tagger hall, has a chance of photoproducing hadronic forms of matter. This process results in the creation of short lived particles decaying to particles with lifetimes sufficient for detection. The decay products of these reactions are subject to the $\sim$2 T magnetic field of the superconducting solenoid. As a result, charged particles follow a helical trajectory as they move through the tracking volume, while neutrals move along straight lines. Charged particles can first interact with a plastic scintillating start-counter that surrounds

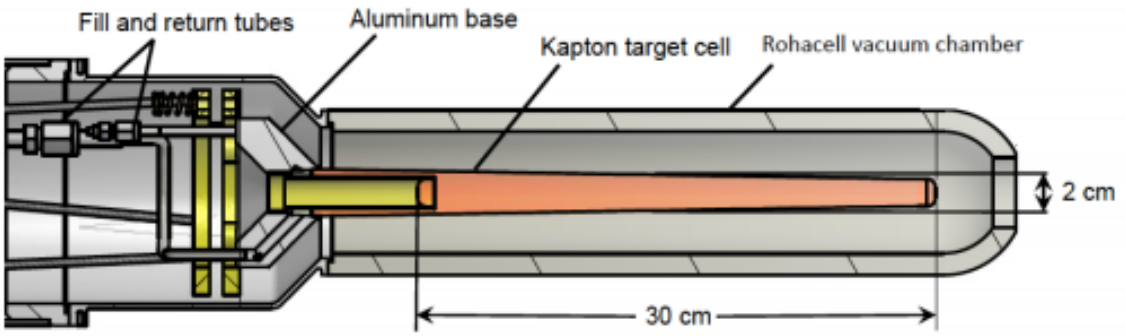

Figure 2.9: Schematic of the GlueX liquid hydrogen target that is inserted in the tracking volume (Albrow *et al.*, 2016).

the target to mark the beginning of an event, in order to match the beam bunch. Inside the solenoid, energy, position, and timing of charged particles are measured in the tracking volume by the central and forward drift chambers that are comprised of straw-and multiwire-drift chambers, respectively. Also inside the solenoid, charged and neutral particles interact with the barrel calorimeter's lead scintillators, producing electromagnetic showers used to determined particle energy, timing, and position. The barrel calorimeter also provides timing information for charged particles. Upon leaving the magnetic field of the solenoid, particles with polar angles less than 11° are subject to the lead glass forward calorimeter and the time-of-flight plastic scintillator. The forward calorimeter provides energy, timing, and position measurements of neutrals, as well as timing measurements of charged tracks. The time-of-flight system provides timing information of charged tracks. GlueX running from Fall 2018 and beyond include the DIRC, which is installed upstream of FCAL and TOF. Remnants of the photon beam are eliminated via a lead beam dump at the end of the beam line in the hall.

2.3.1 Target

The GlueX target is a 30 cm cone made from Kapton foil. It is held inside a vacuum chamber, nominally operates at a temperature 18 K, and pressure of 16 psia. The target cell can be filled with cryogenic hydrogen, helium, or deuterium supplied by stainless steel tubes at the base of the target. A schematic of the target is shown in Figure 2.9 (Barbosa *et al.*, 2014; Adhikari *et al.*, 2021).

2.3.2 Superconducting solenoid

Built in the early 1970's, the GlueX superconducting solenoid was obtained from SLAC. It consists of four separate superconducting toroidal coils connected in series that operates at 1350 A to produce a magnetic field of magnitude 2 T oriented parallel to the beam line. The solenoid can be seen in the photograph of Figure 2.8 (Barbosa *et al.*, 2014; Adhikari *et al.*, 2021).

2.3.3 Tracking

Tracking reconstruction in particle physics is necessary for the determination of particle momentum, energy, and charge, as well as the event vertex from which these particles originate. Determination of physical quantities such as these assist in particle identification of charged tracks moving helically through the magnetic field of the GlueX solenoid. The tracking is an integral part of the GlueX experiment and requires data from the the GlueX central drift chamber (CDC) and forward drift chamber (FDC).

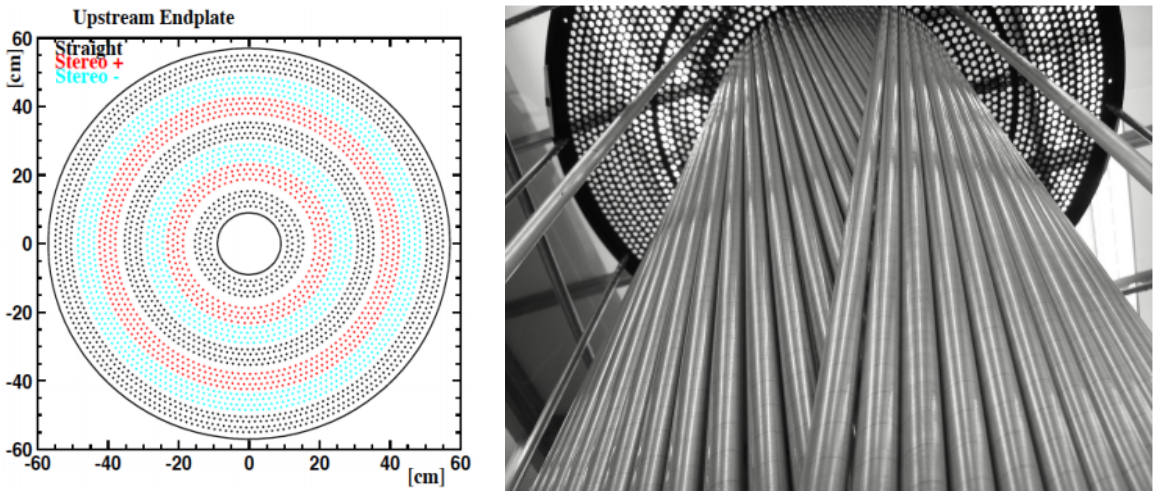

(a) (b)

Figure 2.10: (a) Front view schematic of the CDC showing the orientation of the different straw tubes. (b) Photograph of the side of the CDC during construction showing the stereo straw tubes (Barbosa *et al.*, 2014; Adhikari *et al.*, 2021).

Central drift chamber

A major detector within the tracking system of the GlueX experiment is the Central Drift Chamber (CDC). The CDC consists of $3,522$, 1.5 m long Lamina straw tubes arranged cylindrically over 28 layers, 12 axial and 16 stereo. The Lamina straws are 1.6 cm in diameter and are 50 μm thick made from four layers of mylar tape with the inner-most layer containing 100 nm of vapor-deposited aluminum that acts as a cathode. The anode sense wires contained within each straw tube are 20 μm diameter gold plated tungsten tensioned to 37 g. Straw tube and sense wire choice and design prevent sagging, ensuring uniformity in the electric field around each sense wire. Arranging the straw tubes in this manner creates a cylindrical tracking volume with upstream G-10 inner wall, aluminum endplate, and downstream carbon fiber endplate with specifically machined holes to hold the straw tubes.

A cylindrical gas plenum enclose each endplate of the tracking volume with the upstream consisting of polycarbonate, and the downstream consisting of Rohacell

sidewalls and a ring-shaped end-wall of aluminum coated mylar, ensuring a nominal $60\% - 40\%$ argon-CO_2 gas mixture at 1 atm in each straw tube. The chamber's center is placed 25 cm downstream of the target within the solenoid, providing a 6° to 165° polar angular coverage, and position resolution of 150 μm tranversely and 1.5 mm longitudinally.

The 28 layers of the CDC are arranged to provide optimal tracking measurements free of ambiguity. The stereo straw tubes are set at 6° and -6°, with two layers of each. From center and in sets of four, the CDC is arranged with axial, positive stereo, and negative stereo straw tubes as shown in Figure 2.10b. Each straw tube is held between 1400 and 2300 V with preamplified outputs sent to 12 bit flash ADCs operating at 125 MHz (Barbosa *et al.*, 2014; Van Haarlem *et al.*, 2010).

According to the Lorentz force, charged particles originiating from the decay of photoproduced hadrons move through the solenoid's magnetic field, B, along a curved path with radius of curvature, R. Therefore, particles with transverse momentum, p_T, will have a radius of curvature $R = p_T/qB$ where q is the particle's charge. The size of the radius of curvature and the direction of the particle's rotation in the magnetic field are measured via the CDC to determine the transverse momentum, path-length, polar and azimuthal angles of the event vertex, and the particle's charge.

Beyond these measurements, hit patterns within the CDC are used to determine the position of particles as they move helically through the CDC. These positions are used alongside a helical fit from which the energy deposition, dE/dx, is determined. Measurements of the dE/dx can be used in particle identification for low momentum particles, such as pions and kaons with approximately 250 MeV momentum (Jarvis *et al.*, 2020). As supported by the Bethe-Bloch formula, energy deposition measurements do not provide sufficient separation between pions, kaons, and protons for particle identification at high momentums.

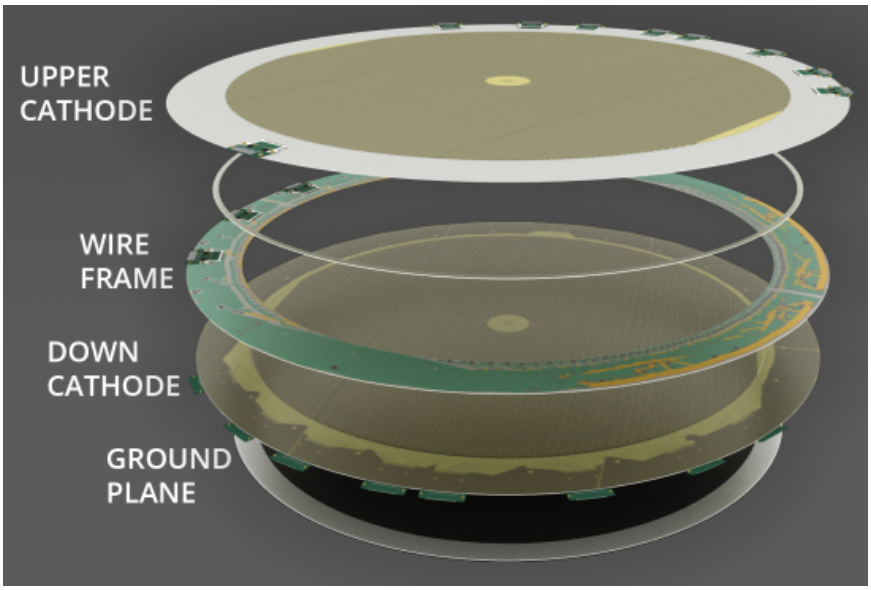

Figure 2.11: Image of the layers for one of the six drift chambers that make up the FDC (Adhikari *et al.*, 2021).

Forward drift chamber

Another detector that contributes to tracking in GlueX is the forward drift chamber (FDC). The FDC consists of four circular sections facing perpendicular to the beam line and located downstream of the CDC within the solenoid (See Figure 2.11). Each section contains six independent flat drift chambers rotated by 60° with respect to each other about the symmetry axis, such that the azimuthal orientation assists in removing tracking ambiguities.

The six drift chambers that make up each section of the FDC have a wire and cathode plane. Wire planes are located between sets of cathode planes with a 5 mm gap. Each wire plane is constructed by alternating 96 20 μm diameter gold-plated tungsten signal wires and 97 80 μm diameter gold-plated copper-beryllium alloy field wires with 5 mm spacing. An approximately 5×10^4 gain is ensured by a 2200 V applied to the signal wires, and a -500 V applied to the field wires ensures the electric field maintains its circular symmetry. The cathode planes consist of 25 μm

thick kapton with 216 $29 - 100$cm long strips of 2 μm thick, pure ^{29}Cu. The FDC design operates under the same gas conditions as the CDC (Barbosa *et al.*, 2014; Pentchev *et al.*, 2017).

2.3.4 Calorimetry

Two types of calorimeters exist in particle physics, electromagnetic and hadronic, which are further classified into sampling or homogeneous. Electromagnetic calorimeters measure electron and photon electromagnetic interactions with matter, while hadronic calorimeters measure strong interactions with matter. Sampling calorimeters contain alternating layers of high density material and a material that produces a signal from the expected interaction, while homogeneous calorimeters consist of a single material that performs both roles. In general, energy deposited by particles traversing the medium result in electrical signals from nuclear effects, which is analagous to measuring temperature in a heat transfer calorimetry method. The GlueX spectrometer has two calorimeters, the barrel calorimeter (BCAL) and the forward calorimeter (FCAL).

Barrel calorimeter

The barrel calorimeter (BCAL) is a sampling, electromagnetic calorimeter modeled after KLOE at DAΦNE that surrounds the CDC and FDC within the solenoid magnet. With complete azimuthal coverage, BCAL measures energy, timing, and position of photon-produced electromagnetic showers and charged-track timing information, for particles with shower energies greater than 0.5 GeV and polar angles between $11^\circ - 126^\circ$. The cylindrical detector is 390 cm long with an inner diameter of 130 cm and outer of 180 cm.

Two black Tedlar-wrapped light-guides per column collect scintillating light to

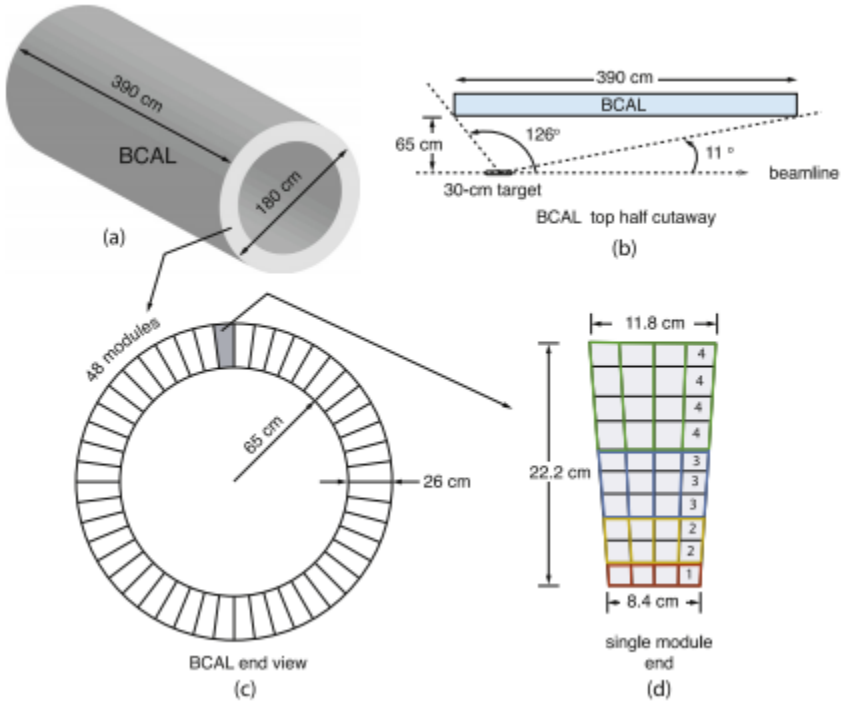

Figure 2.12: (a) Barrel showing the dimensions of BCAL. (b) Cross section of the barrel providing further information on the dimension of BCAL with respect to the beamline. (c) Front cross section of BCAL showing the arrangement of the 48 modules around the beam line. (d) Schematic of a single module with the four layers arranged to provide a trapezoidal shape Barbosa *et al.* (2014).

pass to their corresponding SiPMs, providing 10 light guides per column and 16 summed readout cells per module. The readout cells are summed by columns in a 1:2:3:4 scheme: no summing if shower begins in layer 1, summing 2 if in layer 2, summing 3 if in layer 3, and summing 4 if in layer 4. Due to the trapezoidal shape of a module at a 3.75° incline, the light guides's input cross section increases in size radially outward from an inner of $21 \times 21\text{mm}^2$ to an outer of $27 \times 25\text{mm}^2$ (Beattie *et al.*, 2018).

As determined through Gaussian fits of timing differences between the RF bunch and the particles time propagated back to the event vertex for radiative decays of $\pi^0$and η, the time resolution for neutrals is 150 ps from 1 GeV shower simulations.

The energy resolution of an electromagnetic calorimeter is determined by

$$\frac{\sigma_E}{E} = \frac{a}{\sqrt{E}} \oplus b \oplus \frac{c'}{E} \tag{2.1}$$

where $\oplus$ defines addition in quadrature, $a/\sqrt{E}$ is the stochastic term whose contribution is mainly from sampling fluctuation effects and some photoelectron statistic effects, b is the constant term from energy dependent uncerainties such as module calibration variation, and c'/E contributes effects due to high rates. At 1 GeV, Gaussian fits of invariant mass distributions for π^0 and η, of Monte Carlo and collected data, produce an energy resolution of $\sigma_E/E = 5.0\%/\sqrt{E} \oplus 4.4\%$ (Adhikari *et al.*, 2021).

Forward calorimeter

As shown in Figure 2.13, the forward calorimeter (FCAL) is an electromagnetic calorimeter covering a circular, vertical area 2.4 m in diameter and located 5.6 m downstream of the target's center. FCAL uses 2800 $4 \times 4 \times 45$ cm^3 lead glass blocks decommissioned from the E852 experiment at Brookhaven National Laboratory and the RadPhi Experiment in Hall-B at JLab to measure energy, position, and time of charged and neutral particles. Particles with energies greater than 0.1 GeV and polar angles between $1^\circ - 11^\circ$ interact with the lead glass blocks to produce electromagnetic showers that flow through acrylic cylindrical light guides to FEU 84-3 photomultiplier tubes. Cockroft-Walton bases deliver $1500 - 1800$ V to the PMTs and monitor their voltage, temperature, and current (Barbosa *et al.*, 2014).

Similar to the neutral timing resolution obtained for BCAL, FCAL's > 1.1 cm neutral transverse position resolution is obtained from a 1 GeV shower simulation. Furthermore, the neutral energy resolution is $\sigma_E/E = 6.2\%/\sqrt{E} \oplus 4.7\%$ as determined by Monte Carlo and data for π^0 and η (Adhikari *et al.*, 2021).

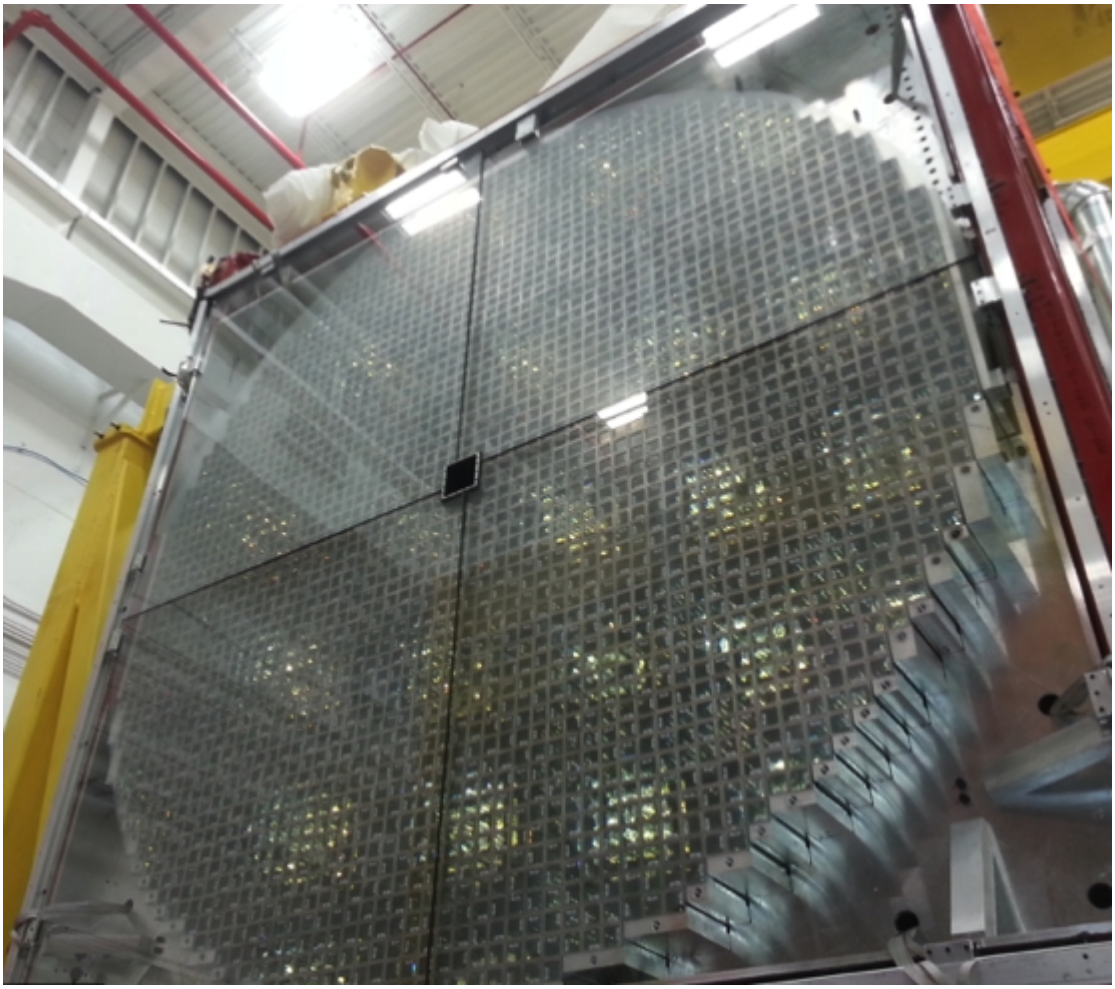

Figure 2.13: Photograph of FCAL during construction showing the arrangement of the lead crystals.

2.3.5 Charged particle identification detectors

At the time of commissioning, the GlueX spectrometer had two scintillator based detectors used for charged particle identification. These detectors supported separation of pions and protons to assist in the initial phase of the GlueX experiment which relied on the analysis of final states decaying to protons, pions, and neutrals. As of 2019, the DIRC, or detection of internally reflected Cherenkov light, was added to assist in the separation of pions and kaons and initiate phase II of GlueX which includes the investigation of final states decaying to protons, pions, kaons, and neutrals. This

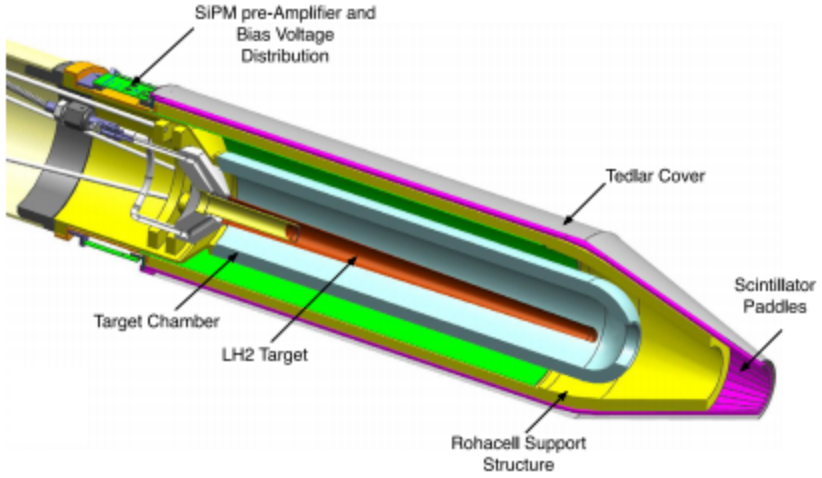

Figure 2.14: Schematic of the start counter depicting its arrangement around the GlueX liquid hydrogen target (Adhikari *et al.*, 2021).

section will focus on the scintillating detectors of GlueX, the start counter (ST) and the time of flight (TOF).

Start counter

The start counter (ST) consists of scintillating paddles arranged in a barrel around the GlueX liquid hydrogen target. It is used to obtain the start time of an event that is consistent with tagged photons and to obtain energy loss (dE/dx) of particles as they move through scintillator. The ST's barrel shape constructed from 30 EJ-200 scintillator paddles has a radius of 78 mm which decreases to 20 mm downstream, as shown in Figure 2.14. Support for the ST's scintillating paddles is provided by 11 mm thick Rohacell foam. Tedlar wrapping creates a light tight environment for the light to be passed to four Hamamatsu S109031-050P SiPMs per paddle (Barbosa *et al.*, 2014).

The time resolution of the ST is determined by comparing the event time measured by ST paddles and the accelerator RF time, producing an average resolution of 234 ps. Beyond producing timing information for matching to tagger photons, the ST also

Figure 2.15: Photograph of TOF showing the horizontal paddles and location of the PMTs.

contributes to particle identification through energy deposition (dE/dx). The dE/dx measured by ST can assist in separating pions and protons up to 0.9 GeV. However, the dE/dx resolution is not sufficient to assist in the identification of kaons (Pooser *et al.*, 2019).

Time of flight

As shown in Figure 2.15, the time of flight (TOF) detector consists of a vertical upstream plane and a horizontal downstream plane each made from 46 scintillating paddles arranged with an effective 2.52×2.52 m^2 area. Located just downstream of FCAL, 5.5 m from target center, TOF obtains timing and energy loss information for charged particles. Each paddle is EJ-200 scintillator approximately $252 \times 6 \times 2.54$ cm^3 with the exception of those near the beam line for a 12×12 cm^2 beam hole and a 3 cm

width to reduce detection rate. The paddles are made light-tight with black Tedlar and have UV transmitting plastic light-guides attached to H10534 Hamamatsu PMTs on both sides of the paddles. The timing resolution of a paddle is ~ 95 ps (Barbosa *et al.*, 2014; Denisov *et al.*, 2002).

Like ST, TOF is used to help identify particles. TOF can be used to separate pions, kaons, and protons. For pions and protons, TOF can produce separation for momentum up to 4.5 GeV/c. Unlike with ST, TOF can actually separate pions and kaons for momentum up to 2 GeV/c. Despite this ability, many meson states decay to kaons with high momentum that the TOF cannot effectively identify (Adhikari *et al.*, 2021).

Chapter 3

DATA SELECTION AND $\gamma P \to PK\bar{K}\pi^0$ SURVEY

This chapter focuses on analysis techniques used to select $\gamma p \to pK^{*\pm}(892)K^{\mp}$ events in GlueX to produce physical observables. It begins with a discussion of the run conditions for the data sets, before outlining the reconstruction of the tagged photons and triggered events in GlueX. With the common analysis techniques outlined, the event selection is presented.

3.1 Run periods

The GlueX data used in the presented analysis was collected during two 2018 run periods, which consist of 145 billion, and 78 billion total events, respectively. As discussed, each run period used an approximately 11.6 GeV electron beam to produce a polarized and unpolarized photon beam via the Bremstrahhlung process. The linear polarization of the photon beam can be oriented 0°, 45°, 90°, and 135° azimuthally relative to the floor. The unpolarized photon beam is generated via incoherent Bremstrahhlung using an aluminum foil radiator and was used for a portion of each run period.

Over the course of the first phase of the GlueX experiment, the beam intensity increased. Compared to 2017 run conditions with 100 nA and 150 nA average electron beam currents, the 2018 run periods saw increases in the intensity to 250 nA and 350 nA average electron beam currents. The flux increases not only provide an ability to reduce statistical uncertainties in results, but also prepares GlueX for the second phase of running at high rate.

3.2 Reconstruction and event selection

The reconstructed data sets undergo a selection process to obtain $\gamma p \to pK^+K^-\gamma\gamma$ events that meet specific criteria. During spectrometer operations, hit recording depends on a trigger that select events conforming to underlying physics. For the GlueX spectrometer, the trigger requires an energy threshold for FCAL and BCAL. Hit information is recorded when enough energy is deposited in the GlueX calorimeters according to clearly defined criteria. Specifically, if a particle deposits energy in FCAL and BCAL, such that $E_{FCAL} + 0.5E_{BCAL} > 0.5$ GeV, then BCAL and FCAL are checked for interactions with other particles. If another particle interacts with FCAL, such that $E_{FCAL} > 0$ GeV, or if a particle deposits energy in only BCAL, such that $E_{BCAL} > 1.2$ GeV, then information is recorded.

The raw hit data for charged particles is reconstructed through a helical fitting routine, which accounts for those particles swimming through the ST, BCAL, CDC, FDC, FCAL, and TOF. The tracking routine run through a list of a charged particle identities, specifically proton, π^+, K^+, positron, antiproton, π^-, K^-, or electron, to produce kinematic information for each particle type (if the fit converges). This means that each charged track may have multiple hypotheses for a particle's identity. The reconstruction also accounts for photons by determining their energies from electromagnetic showers produced in BCAL and FCAL.

When looking at specific topologies, such as $\gamma p \to pK^+K^-\gamma\gamma$, all events with possible combinations of $pK^+K^-\gamma\gamma$ are investigated. This means, if within the positive charged tracks there is a hypothesis of proton for the first positive track and K^+ for the second charged track, and a vice versa hypothesis, it will be true that the pK^+ within the desired $pK^+K^-\gamma\gamma$ is satisfied by both hypotheses. In fact, initially events with up to 6 charged tracks with multiple identification hypotheses and

10 neutrals are used to produce all possible combinations of $\gamma p \to pK^+K^-\gamma\gamma$. The number of charged tracks and neutrals used to produce these combinations is later reduced to 3 and 2, respectively, allowing for the possibility of ghost tracks (tracks reconstructed from spurious accidentals and noise), and tracks or neutrals from cosmics to be eliminated by other methods.

3.2.1 Beam photons

Reconstructed beam photons incident on the liquid hydrogen target are selected for each event. Since photons are generated via the Bremstrahhlung process from 249.5 MHz electron beam pulses, many photons may match an event seen in the GlueX spectrometer. In reality, only one photon is responsible for an event, but all photons consistent with the accelerators RF time are analyzed. The difference in the vertex time of an event and the tagged photon time produces peaks separated 4.008 ns apart that are used to select signal events and side-band events. The signal peak is centered over 0 ns with boundaries of -2.004 ns and 2.004 ns. Accidental peaks are smaller with peaks spaced every 4.008 ns. Figure 3.1 shows the difference in the vertex time and RF times for $\gamma p \to pK^{*\pm}(892)K^{\mp}$ events. When performing analysis, a statistical correction is made to account for the accidentals by weighting combinations with accidental photons by a factor of $-1/N_a$, where N_a is the number of side bands used in the analysis. Due to bleed-through of the side-band peak adjacent to the signal peak, the first set of side-bands are left out of the subtraction.

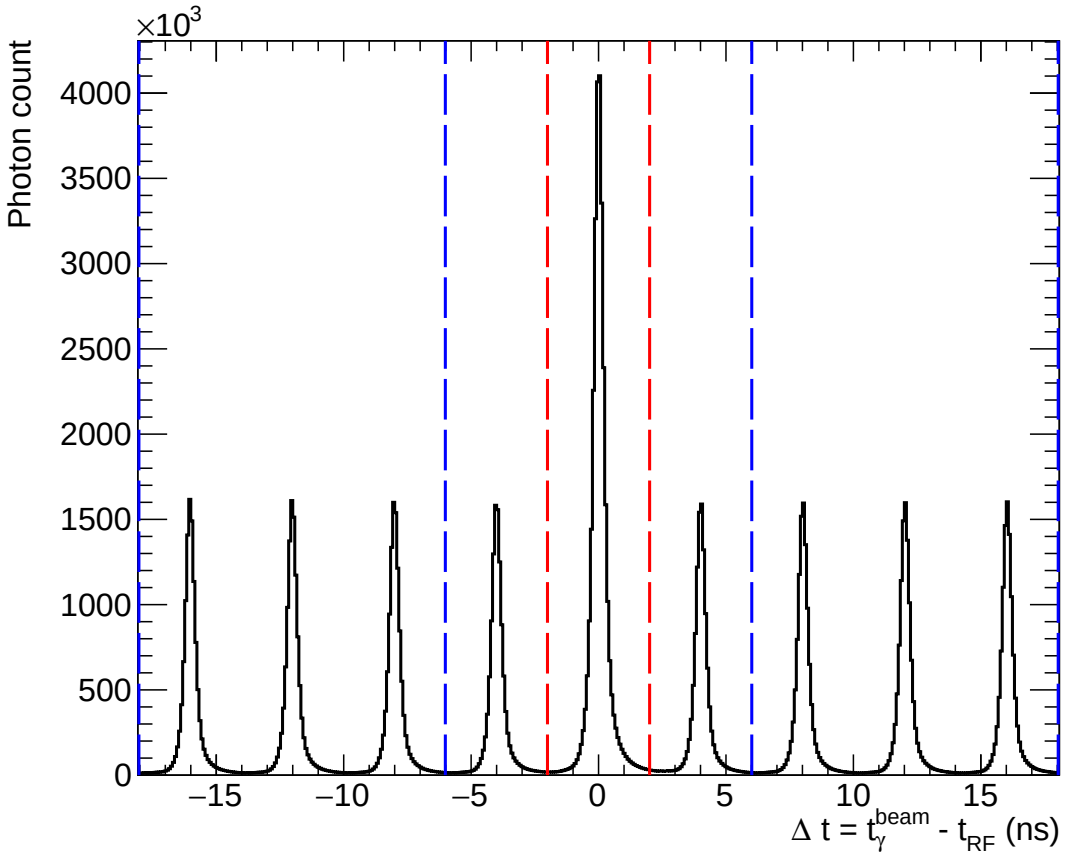

Figure 3.1: Tagged photons are selected from the timing distribution where incident photons are in 4.008 ns beam bunches. The signal peak between −2.004 ns and 2.004 ns are for prompt photons in time with events produced on target (selection shown by vertical red, dashed lines). The adjacent beam bunches are accidentals used for background subtraction because they should be representative of the background under the signal peak (selection shown by vertical blue, dashed lines).

The accidental subtraction technique relies on the fact that the side bands are representative of the background beneath the signal peak and that the side-band peaks are of the same size. However, different numbers of electrons are produced by CEBAF's electron guns for each pulse. As a result, the accidentals do not truly represent the accidental background without a correction factor. The correction factor (f) is determined by direct analysis of tagged electrons in time with the pair spectrometer. Signal combinations are given a weight of 1, while side-band combinations are given a weight of $-f/N_a$.

3.2.2 Initial selection

Analysis of reconstructed charged tracks and neutrals seen in the GlueX spectrometer undergo an initial selection process. This is first accomplished with cuts on the timing for charged tracks and neutrals to ensure they are consistent with the event time. Beyond the timing cuts, a missing-mass-squared cut, a minimum proton momentum cut, and a requirement regarding the distance between the detected neutrals are included. Combinations that survive the selection criteria are used to select events for further analysis.

Similar to the photon timing, the difference between the time propagated back to the vertex for reconstructed tracks and the RF time is used to select combinations in time with photons on the target. This timing difference is used as an initial particle identification. It is expected that for the correct particle identification in the tracking reconstruction, the timing distribution will be centered over zero. Figure 3.3 shows the BCAL, FCAL, and TOF timing distributions for each detected particle type versus momentum with black lines indicating cuts that could be applied to select tracks and neutrals. The cuts used in this analysis are defined in Table 3.1.

Due to the timing resolution of detectors and the detector's rate of particle detection, the timing of track candidates is ordered according to the detectors that provide timing information. For charged tracks, if a particle is detected in BCAL and TOF, the propageted time determined from the BCAL hit time is used instead of that determined by the TOF hit time. The order of preference for charged tracks is BCAL, FCAL, TOF, ST, and NULL, where NULL indicates that the track only interacted with the drift chambers. For neutrals, this order of preference is BCAL and FCAL. Due to the difficulties in identifying kaons, events where the charged track timing propagation is determined from ST and NULL are removed. Without the implemen-

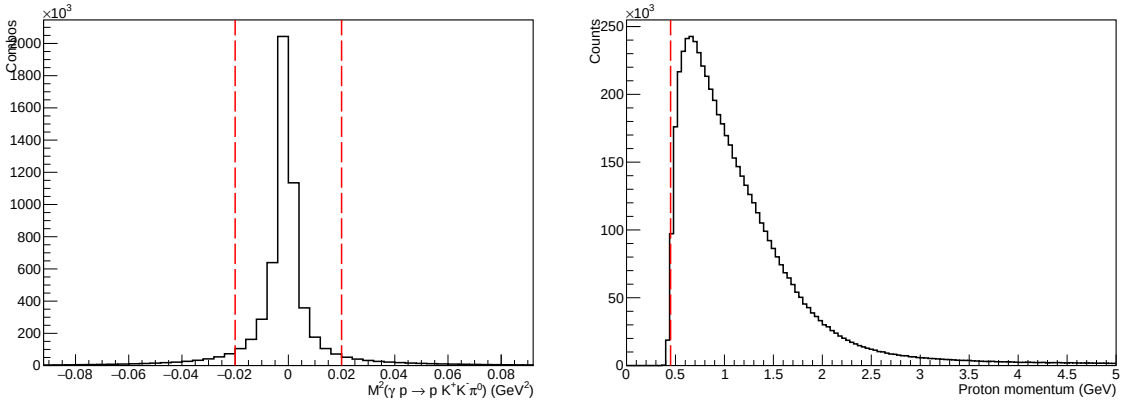

(a) (b)

Figure 3.2: (a) Measured missing mass squared, and (b) proton momentum $\gamma p \to pK^+K^-\gamma\gamma$ events in GlueX.

Detector	Δt_p (ns)	$\Delta t_{K^\pm}$ (ns)	Δt_γ (ns)
BCAL	± 0.5	± 0.2	± 2.0
FCAL	± 1.0	± 0.5	± 2.0
TOF	± 0.3	± 0.15	NA
ST	None	None	NA
NULL	None	None	NA

Table 3.1: Cut values that ensure charged tracks and neutrals are in time with beam photons on target for protons and kaons detected by BCAL, FCAL, and TOF, and neutrals detected by BCAL and TOF. ST and NULL charged tracks are completely removed.

tation of additional particle identification methods, the kaon samples are overwhelmed by pion contamination for events with charged track hit times determined by ST and NULL.

The GlueX spectrometer has acceptance gaps for neutrals particles around the beam hole and the space between BCAL and FCAL. To remove reconstructed neutrals in these regions, a cut is placed on polar angles that are less than 1.5°, or are between 10.3° and 11.5°. Neutrals with these polar angles traveled through the beam hole or

through the space between BCAL and FCAL, respectively. The photons with these conditions are removed because they originate from areas of no neutral acceptance and are an artifact of the neutral reconstruction.

To improve the reconstructed photons in the $\gamma p \to pK^+K^-\gamma\gamma$ topology detected by BCAL and FCAL, a minimum neutral shower energy cut and a neutral shower quality cut are applied, respectively. By requiring a minimum energy threshold of 0.5 GeV for photon showers, the quality of the reconstructed photons detected by BCAL is improved. The quality cut for FCAL neutral showers is a fiducial cut that improves the reconstructed photon energies for those neutrals detected by FCAL, by ensuring realistic results from the clustering algorithm. Furthermore, it is required that a combination has no unused energy from neutral showers.

Beyond the cuts applied to neutral showers, a cut is applied to the distance between the two photons of $\gamma p \to pK^+K^-\gamma\gamma$ events. This cut removes combinations with quality of reconstructed photons originating from a single photon, significantly improving the reconstructed photons detected in FCAL around the beam pipe where neutral detection rates are high.

A missing mass squared cut is applied to select events consistent with the expected kinematics for a reaction. The missing-mass-squared cut, MM^2, is

$$\begin{aligned} MM^2(\gamma p \to pK^+K^-\gamma\gamma) &= (p_i - p_f)^2 \\ &= (p_\gamma^{beam} + p_p^{target} - (p_p^{recoil} + p_{K^+} + p_{K^-} + p_\gamma + p_\gamma))^2 \end{aligned} \tag{3.1}$$

where p is the four-momentum vectors for each particle in the reaction. The invariant mass squared of the $\gamma p \to pK^+K^-\gamma\gamma$ combinations as determined from the measured momentum and energy is shown in Figure 3.2a with the red lines indicating the cut applied to select combinations around zero. The conservation of momentum and

energy is ensured by kinematic fitting, which will be discussed in Section 3.2.3.

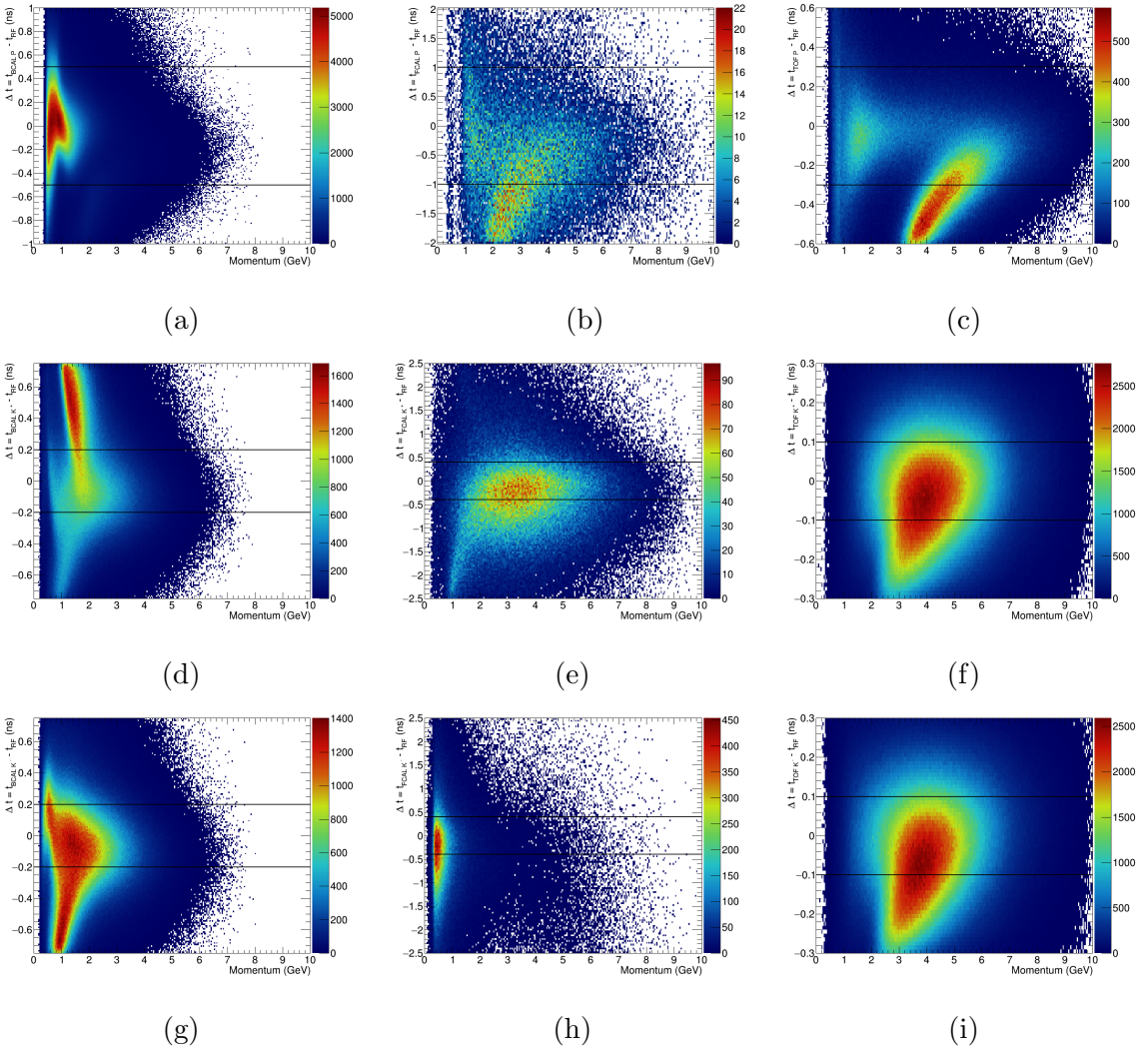

Figure 3.3: Difference in propagated time to the vertex and the RF time versus the momentum for charged particles in $\gamma p \to pK^{\pm}K^{\mp}\pi^0$ events from the 2018-01 run period. The first row (a-c) shows proton track candidate timing differences for BCAL, FCAL, and TOF from left to right. Similarly, row 2 (d-f) and row 3 (g-i) for K^+ and K^- track candidate timing differences for BCAL, FCAL, and TOF, respectively. The black lines indicate cuts applied to select candidates most in time with the vertex, around a time difference of 0 ns.

A recoil proton momentum cut requiring $p_p^{recoil} > 0.45$ GeV is applied to improve proton selection. Although the fitting routine of the tracking reconstruction may converge for momentum below the cut value, this cut value is just above the momentum resolution of the CDC. Figure 3.2b shows the proton momentum with a red line

Removal conditions
$\chi^2/n.d.f. > 5$
$\theta_\gamma^{beam} - \theta_{vertex} < 1.5^\circ$
$10.3^\circ > \theta_\gamma^{beam} - \theta_{vertex} < 11.5^\circ$
$E_{BCAL}^{min} < 0.05$ GeV
Shower quality FCAL < 0.5
$d_{\gamma_1,\gamma_2} < 12.5$ cm
$MM^2 > 0.2$ GeV
$p_p^{recoil} < 0.45$
52 cm $< z_{vertex} >$ 78 cm
$r_{vertex} > 1$ cm

Table 3.2: Cut values to select events that meet conditions for further analysis and the production of physical observables.

indicating the cut used to select combinations for further analysis.

3.2.3 Kinematic fitting

The GlueX experiment employs a kinematic fitter to constrain physical quantities within measured uncertainties to enforce conservation of momentum, conservation of energy, and ensure consistent vertex positions* . A mass constraint on particles may also be included for particles with small mass-widths and insignificant background contributions. Kinematic fitting is performed through a χ^2 minimization, determined by

$$\chi^2 = (\eta_\mathbf{0} - \eta_\mathbf{f})^T \mathbf{G_y} (\eta_\mathbf{0} - \eta_\mathbf{f}), \tag{3.2}$$

* It is possible to include time in the vertex fit to enforce a space-time constraint, but this has yet to be rendered functional.

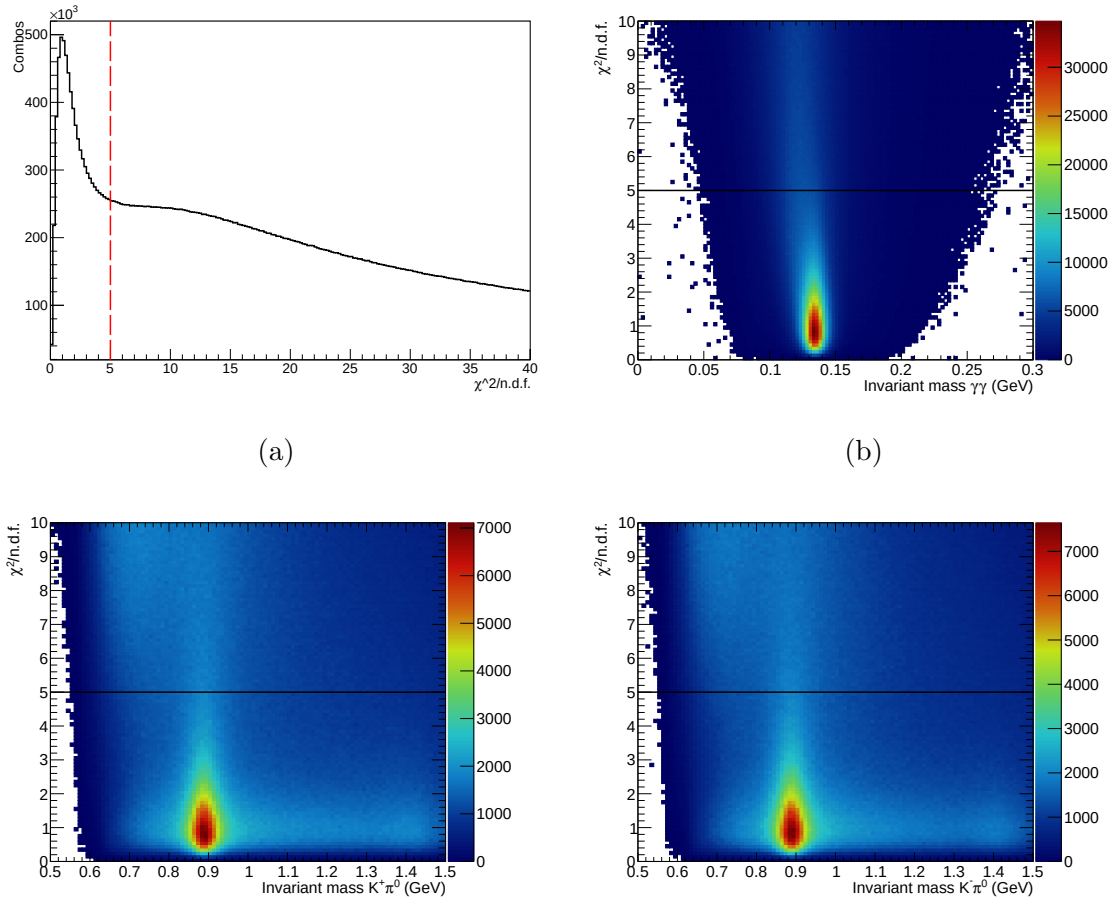

(a) (b)

(c) (d)

Figure 3.4: (a) Kinematic fit χ^2/n.d.f. for $\gamma p \to pK^+K^-\gamma\gamma$ events with vertical dashed line showing the selection criteria at $5\chi^s/n.d.f.$. Kinematic fit χ^2/n.d.f. versus the invariant mass of (b) $\gamma\gamma$, (c) $K^+\pi^0$, and (d) $K^-\pi^0$. The invariant mass distributions show evidence of a (b) π^0 meson, (c) $K^{*+}(892)$ meson, and (d) $K^{*-}(892)$, which are used to establish χ^2/n.d.f. cut as shown by the black lines.

where η_0 is the vector of the kinematic/vertex values before the fit, η_f is the vector of the kinematic/vertex values after the fit, and G_y is the inverse of the covariance matrix for those quantities. A cut is placed on the χ^2 per degrees of freedom. In the analysis, the combination with the best $\chi^2/n.d.f.$ is selected for each event. Although methods can be employed to analyze all combinations, the tools built for the PWA are currently not built to handle these approaches

For the $\gamma p \to pK^+K^-\gamma\gamma$ events of interest, a four momentum and vertex fit is

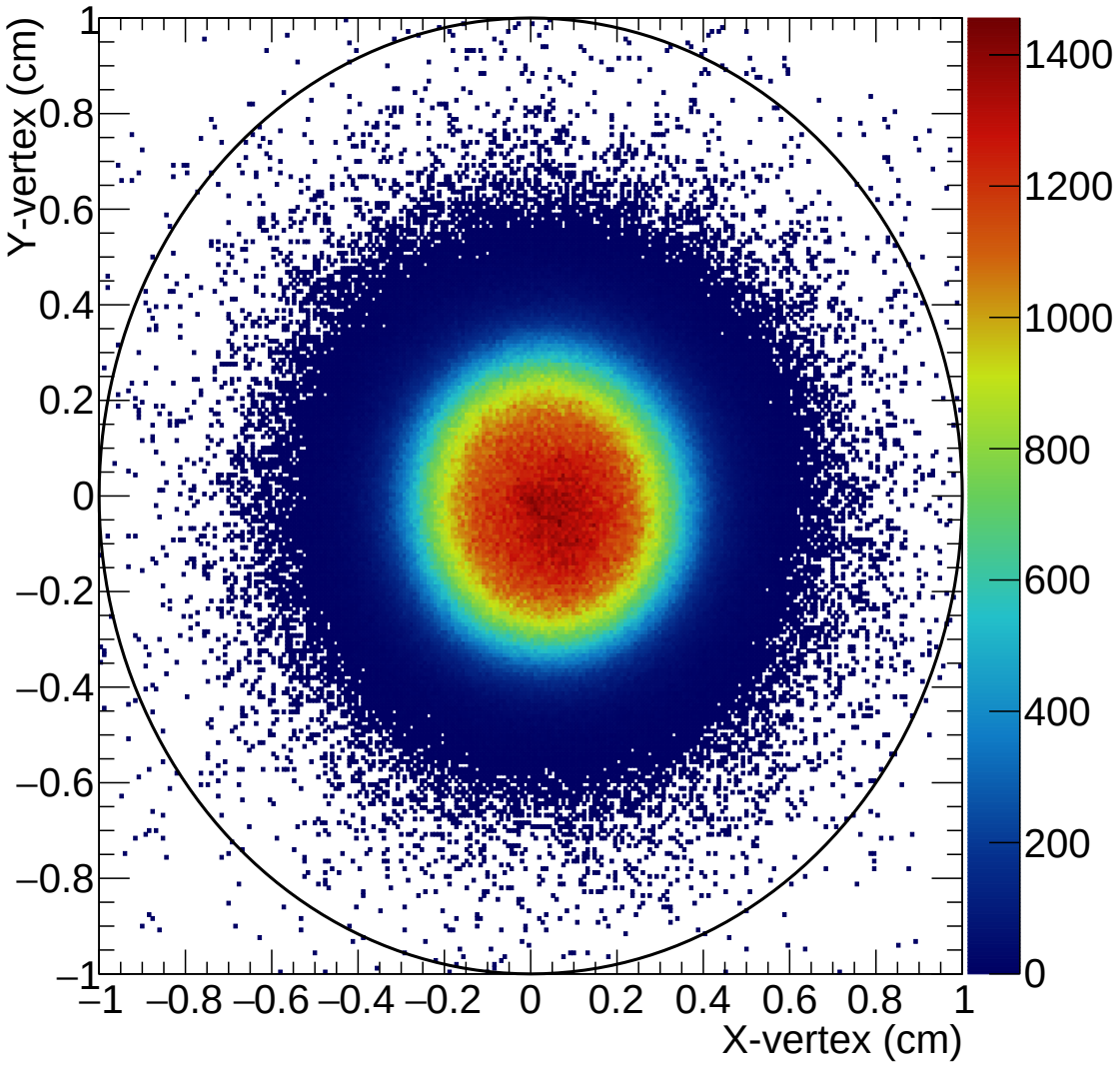

Figure 3.5: X-vertex versus y-vertex as determined by the kinematic fitter for $\gamma p \to pK^+K^-\gamma\gamma$ events. The black circle show the selection of the data to ensure events come from the hydrogen target.

applied. A mass constraint for a π^0 decaying to two photons is not applied within the kinematic fitting routine. Events with $\chi^2/n.d.f. < 5$ are selected for further analysis. Figure 3.4 show the confidence level versus invariant mass of particle combinations from $\gamma p \to pK^+K^-\gamma\gamma$. Clear enhancements for $\pi^0 \to \gamma\gamma$ and $K^{*\pm}(892) \to K^\pm\pi^0$ are discernible in these histograms.

Beyond a confidence level cut, it is necessary to ensure events originate from

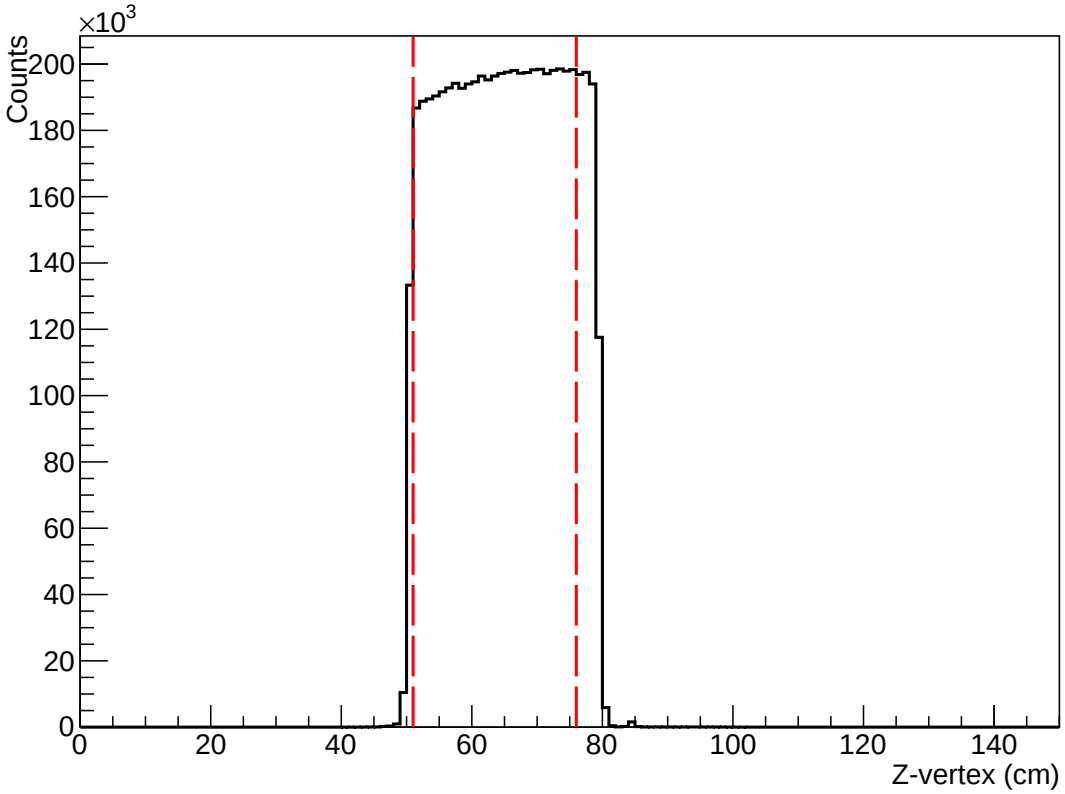

Figure 3.6: Z-vertex for $\gamma p \to pK^+K^-\pi^0$ in GlueX as produced by the kinematic fitter. The vertical red lines show the selection of the data to ensure events come from the hydrogen target.

the target, since this reaction does not contain long lived particles that produce displaced vertices. Events with vertices with radial position $r < 1$ cm and z-position 52 cm $< z <$ 78 cm are selected. The selections for these criteria are depicted in Figures 3.6 and 3.5.

3.3 Events resulting from the selection criteria

The selection of events that meet the criteria outlined in Sections 3.2.1, 3.2.2, and 3.2.3 is used to reconstruct particles that can be further processed to obtain invariant mass distributions. As stated, the $\gamma p \to pK^+K^-\gamma\gamma$ topology is rich with both meson and baryon states. This section focuses on dissecting the richness of states through the

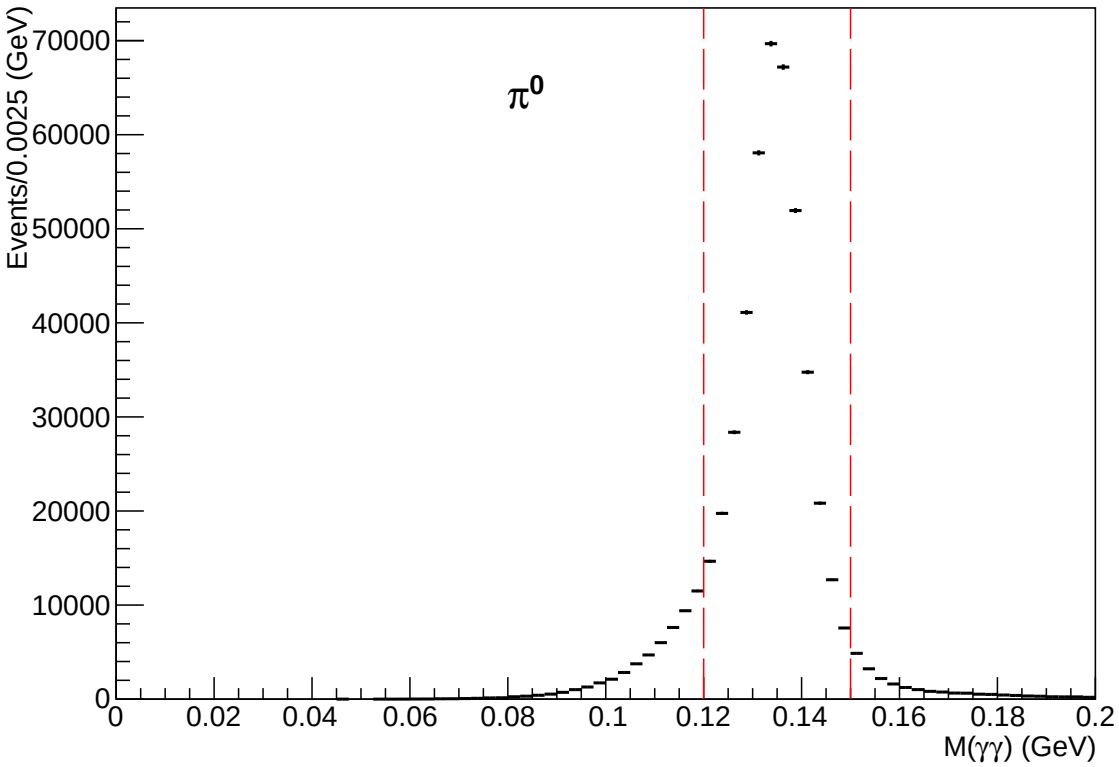

Figure 3.7: The invariant mass of $\gamma\gamma$ from $\gamma p \to pK^+K^-\gamma\gamma$ events. The vertical red lines at 0.12 GeV and 0.15 GeV indicating the selection of events with a π^0 meson.

reconstruction of the π^0 meson state, the background contributions to meson states decaying $K\bar{K}\pi^0$, $a_0\pi^0$, and $K^*\bar{K}$, and their invariant mass distributions. Discussion of this material is in preparation for presentation of PWA results for mesons decaying $K^*\bar{K}$ in the $\gamma p \to pK^+K^-\gamma\gamma$ events of GlueX.

3.3.1 The two photons

Each event contains two photons from the decay of a meson state, specifically the neutral pion. The π^0 meson decays to two photons $\sim$99% of the time. The invariant mass of the two photons produced from their kinematically fit four-momentum vectors is used to select events consistent with a π^0. A Gaussian fit with a third degree

polynomial background produces a center of 134.441(8) MeV, which is not consistent with the PDG reported mass of 134.9768(5) MeV within error (Group *et al.* (2020)). The π^0 is selected $\sim 2\sigma$ from center between 120 MeV and 150 MeV as shown in Figure 3.7.

3.3.2 The K^* mesons

With the selection of the π^0 meson, the $K^*(892)$ strange meson state that decays $K\pi$ nearly 100% of the time is reconstructed. It is produced in $\gamma p \to pK^+K^-\gamma\gamma$ events through the combination of both $K^+\pi^0$ and $K^-\pi^0$ four-momentum. A Gaussian fit with a third degree polynomial background produces a center of 890.5(1) MeV for the $K^+\pi^0$ invariant mass distribution and 890.7(1) MeV for the $K^-\pi^0$ invariant mass distribution. The PDG reports a mass of 891.7(2) MeV for hadroproduced charged $K^*(892)$ mesons, which is inconsistent with the fit values within error (Group *et al.* (2020)). The full width at half maximum (FWHM) is 53.2(4) MeV and 53.5(4) MeV for the $K^+\pi^0$ and $K^-\pi^0$ invariant mass distributions, respectively. The FWHM is inconsistent with the PDG width of 50.8(9) MeV, which indicates effects of the detector resolution. The distributions for such combinations with dashed lines depicting the selection of $K^{*\pm}(892)$ $\sim 2\sigma$ around center from 840 to 940 MeV are shown in Figures 3.8a and 3.8b.

Beyond the $K^*(892)$ meson, evidence of the $K_0^*(1430)$ and $K_2^*(1430)$ mesons are also discernible in the distributions. These charged excited K^* states decay $K\pi$ $\sim$93% and $\sim$50% of the time, respectively. The PDG reports their masses as 1425 MeV and 1427 MeV with widths 270 MeV and 100 MeV (Group *et al.* (2020)). These states can only be separated using a PWA, which would be of use in a search for η_1' decaying $K_1^*(1410)K$ as predicted by LQCD (Meyer and Swanson (2015)).

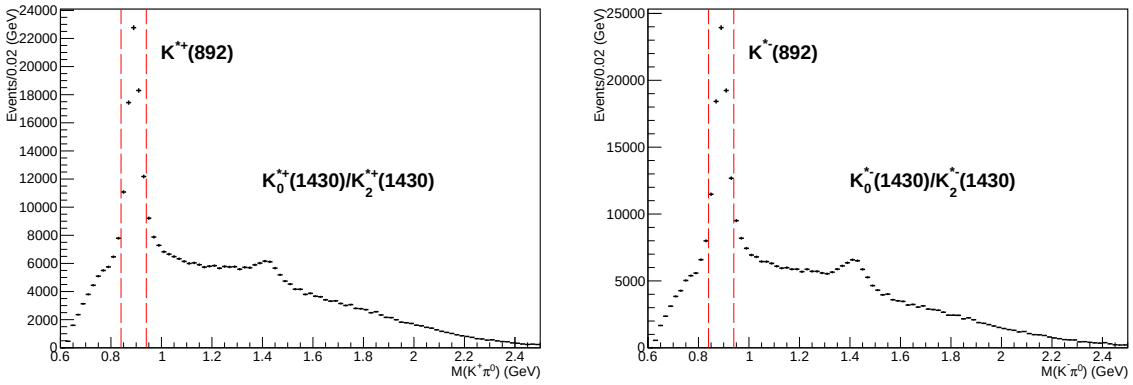

(a) (b)

Figure 3.8: Invariant mass of (a) $K^+\pi^0$ and (b) $K^-\pi^0$ from $\gamma p \to pK^+K^-\gamma\gamma$ events. The vertical red lines at 0.8 GeV and 1.0 GeV indicating the selection of events with a $K^{*+}(892)$ and $K^{*-}(892)$ meson.

3.3.3 Meson and baryon background contributions

The reconstruction of the K^* mesons decaying to $K\pi$ is not the only possible intermediate state found in the $\gamma p \to pK^+K^-\gamma\gamma$ topology. To the detriment of analyses of meson states decaying $a_0(980)\pi^0$, $K^*\bar{K}$, or directly to $K^+K^-\pi^0$, other well known mesons and baryons can be reconstructed from the decay products. Although these other states are of interest to other analysis efforts, they are background contributions to this analysis effort. These other states include, but are not limited to, a potential $\phi(1020)\pi^0$ hadronic molecule candidate, Σ baryons decaying $\Lambda(1520)\pi^0$, Σ baryons decaying Δ^+K^-, Λ and Σ baryons decaying pK^{-*}, and 3π from kaon misidentification.

The first of these background contributions includes the $\phi(1020)\pi^0$ where the $\phi(1020)$ meson decays K^+K^-. Using a 70 GeV pion beam, the Serpukhov-142 experiment first reported a $C(1480)$ exotic meson with isospin $I = 1$ and $J^{PC} = 1^{--}$ decaying $\phi(1020)\pi^0$. E852 collaboration out of Brookhaven found no evidence of this state from side-band subtraction methods and PWA, similar results are reported by

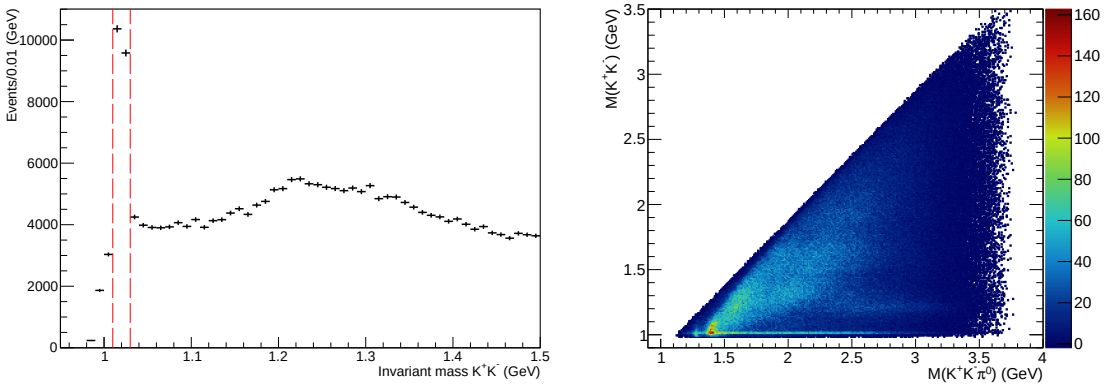

(a) (b)

Figure 3.9: (a) Invariant mass of K^+K^- from $\gamma p \to pK^+K^-\gamma\gamma$ events. (b) Invariant mass of K^+K^- versus invariant mass of $K^+\pi^0$ from $\gamma p \to pK^+K^-\gamma\gamma$ events. Vertical enhancements for $K^{+*}(892)$ and $K_0^{+*}(1430)/K_2^{+*}(1430)$ mesons are discernible, as well as the horizontal enhancement for the $\phi(1020)$ meson. The curved enhancement at low invariant mass is likely pion contamination.

experiments involving pp central production and $p\bar{p}$ annihilation at rest (Adams *et al.* (2001)). The GlueX experiment can also report no evidence of peaks in $\phi(1020)\pi^0$ using a side-band subtraction method like that of the E852 collaboration. OZI-suppression argues against the existence of a meson decaying $\phi(1020)\pi^0$. Despite the lack of evidence for a meson, the $\phi\pi^0$ could be a hadronic molecule, but this possibility lacks theoretical description.

Figure 3.9a shows the K^+K^- invariant mass distribution seen in $\gamma p \to pK^+K^-\gamma\gamma$ events. A Gaussian fit with a third degree polynomial produces a 1019.51(4) MeV center, which is consistent with the PDG reported mass of 1019.46(1) MeV. However, the measured FWHM from this method is 8.9(1) MeV, which is more than double the PDG reported width of 4.25(1) MeV Group *et al.* (2020). The dashed lines are $\sim 2\sigma$ around center from $1010 - 1030$ MeV to show the cut used to remove the $\phi(1020)$ for later analysis, and is used to select the $\phi(1020)$ when searching for the $C(1480)$ meson (Adams *et al.* (2001)). Complete partial wave analysis of the $\phi\pi^0$ decay mode

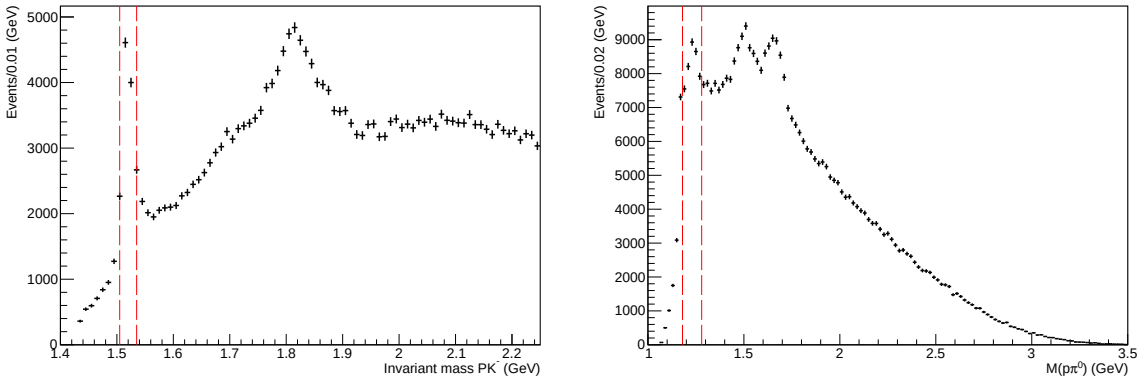

(a) (b)

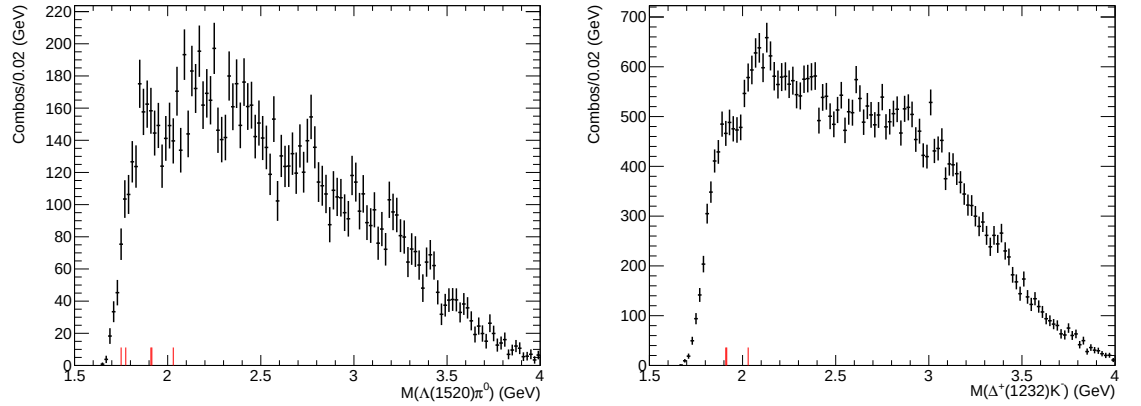

(c) (d)

Figure 3.10: (a) Invariant mass of pK^- from $\gamma p \to pK^+K^-\gamma\gamma$ events. (b) Invariant mass of $p\pi^0$ from $\gamma p \to pK^+K^-\gamma\gamma$ events. (c) Invariant mass of $\Lambda(1520)\pi^0$ from $\gamma p \to pK^+K^-\gamma\gamma$ events. (d) Invariant mass of $\Delta(1232)K^-$ from $\gamma p \to pK^+K^-\gamma\gamma$ events.

should be pursued in order to search for the $\rho(1570)$ or determine whether it is an OZI-violating decay mode of the $\rho(1700)$.

The second major background contribution involves the photoproduction of baryon states from target fragmentation. Unlike the photoproduction of mesons from beam fragmentation that result in a recoil proton, photoproduced strange baryons will contain a proton in the baryonic decay. Σ baryons decaying $\Lambda(1520)\pi^0$ where the $\Lambda(1520)$ decays pK^- are one cause of this background contribution, specifically $\Sigma(1750)1/2^-$,

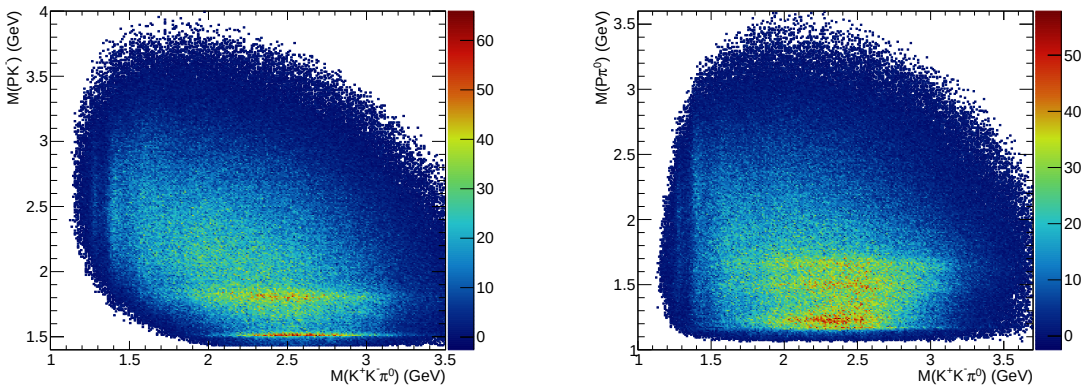

(a) (b)

Figure 3.11: (a) Invariant mass of pK^- from $\gamma p \to pK^+K^-\gamma\gamma$ events. (b) Invariant mass of $p\pi^0$ from $\gamma p \to pK^+K^-\gamma\gamma$ events.

$\Sigma(1775)5/2^-$ through a P-wave, $\Sigma(1910)3/2-$, $\Sigma(1915)5/2+$ through a D-wave, and $\Sigma(2030)7/2^+$. The $\Lambda(1520)$ and heavier overlapping Λ states, including multiple instances within the 1600 to 1800 MeV mass regions, are shown in Figure 3.10a. The PDG reports the $\Lambda(1520)$ mass as $1518-1520$ MeV and width as $15-17$ MeV, which is consistent with the measured mass from a Gaussian with third degree polynomial fit of 1518.5(1) MeV and FWHM of 15.5(3) MeV (Group *et al.* (2020)). Therefore, it is selected or vetoed $\sim 2\sigma$ around center from $1505-1535$ MeV to produce distributions for $\Lambda(1520)\pi^0$, and to produce distributions for $K^+K^-\pi^0$ and $K^{*\pm}K^{\mp}$, respectively. Figure 3.10c shows the invariant mass distribution $\Lambda(1520)\pi^0$ decaying $pK^-\pi^0$ from which narrow peaks for Σ baryons are discernible, along with peaks between 2.0 and 2.5 GeV that have not been reported by the PDG.

The third background contribution includes Σ baryons decaying Δ^+K^-. A clear signal for $\Delta^+(1232)$ is seen in Figure 3.10b, which as before is selected $\sim 2\sigma$ around the measured mass of 1229(1) MeV from $1180-1280$ MeV. The measured mass is consistent with the PDG reported mass of $1230-1234$ MeV, but the FWHM of 53(5) MeV is not consistent with the reported width of $114-120$ MeV (Group

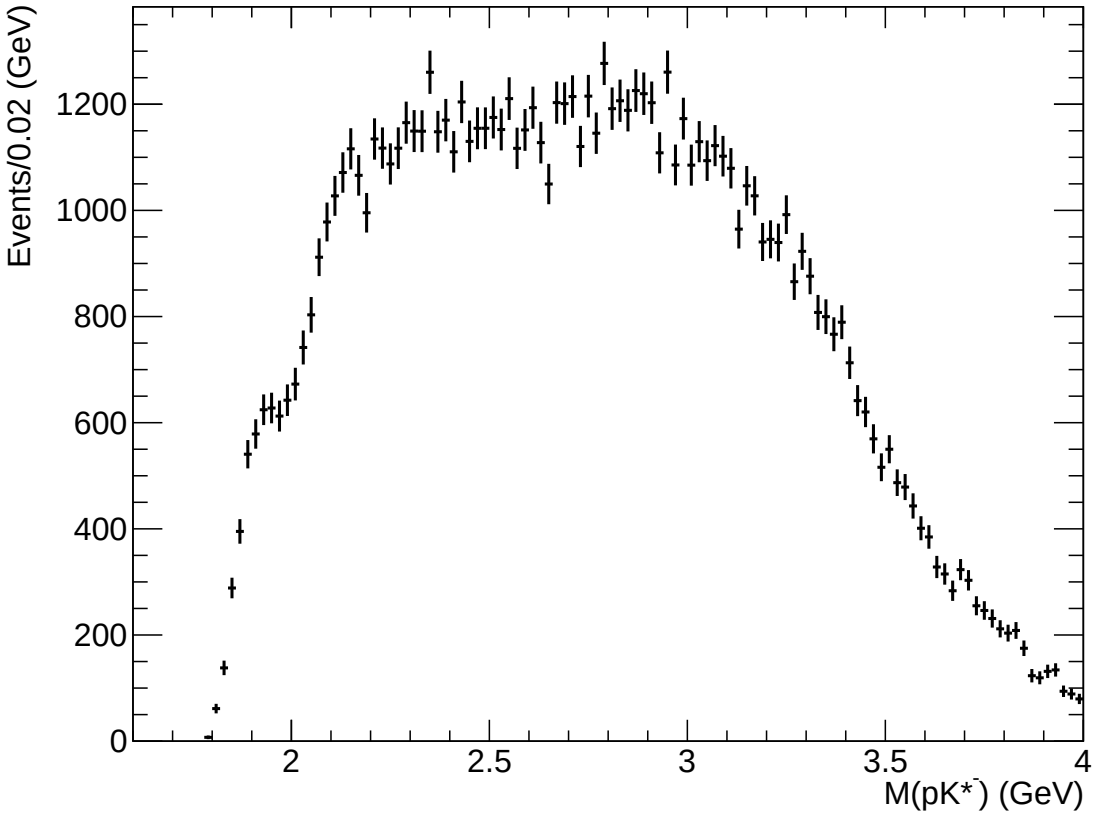

Figure 3.12: Invariant mass of pK^{*-} from $\gamma p \to pK^+K^-\gamma\gamma$ events.

et al. (2020)). Since the cross section of this process is small compared to other baryonic background contributions, a veto cut similar to the $\phi(1020)$ meson and $\Lambda(1520)$ baryon is not used because it would remove a large part of the phase space for $K^+K^-\pi^0$ and $K^{*\pm}K^{\mp}$. Figure 3.10b also shows evidence for N^* and Δ^* states between 1400 MeV and 1800 MeV, which are difficult to identify because of the many overlapping nucleon states in this mass region. Figure 3.10d shows the invariant mass for $\Delta^+(1232)K^-$ from which Σ baryon peaks are discernible.

The last background contribution resulting from particles that decay to the final states of this topology involve the Λ and Σ baryons decaying pK^{*-}. Using the selection of the K^{*-} previously discussed, one can search for the myriad of Λ and Σ states that decay via this branch, specifically $\Lambda(1670)1/2^-$, $\Sigma(1750)1/2^-$, $\Lambda(1810)1/2^+$,

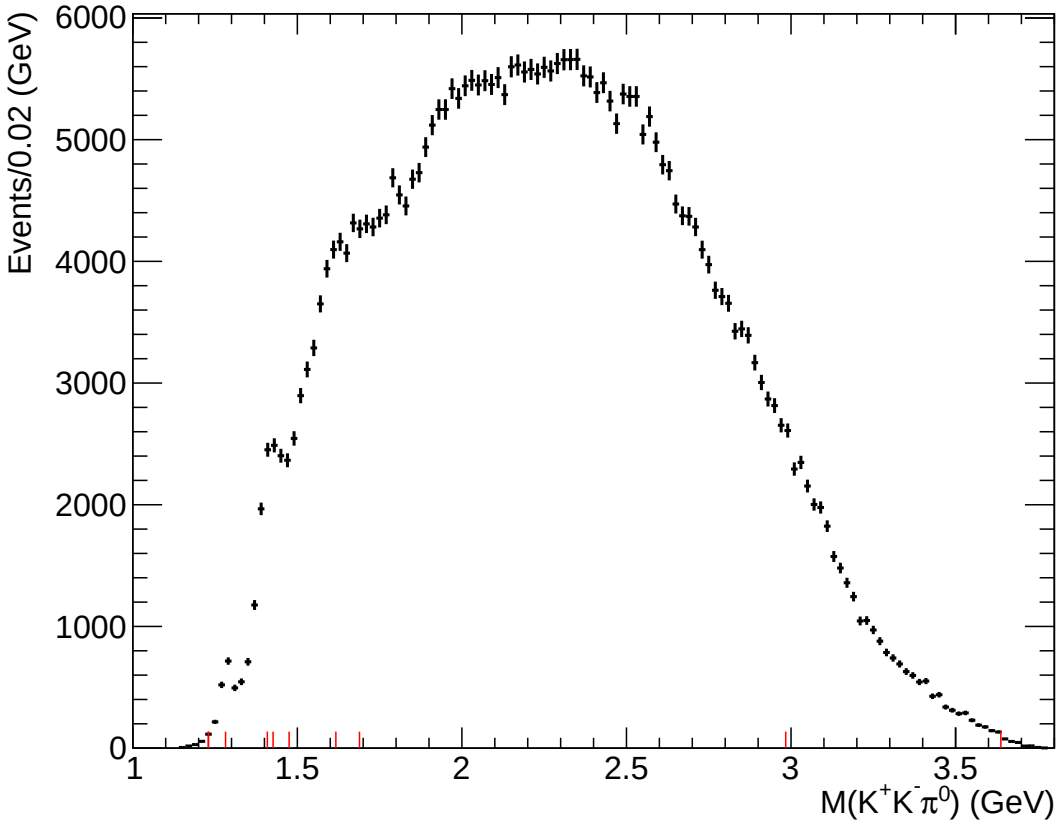

Figure 3.13: Invariant mass of $K^+K^-\pi^0$ from $\gamma p \to pK^+K^-\gamma\gamma$ events.

$\Lambda(1800)1/2^-$, $\Lambda(1820)5/2^+$, $\Lambda(1890)3/2^+$, $\Sigma(1910)3/2^-$, $\Sigma(1915)5/2^+$, $\Sigma(2030)7/2^+$, $\Lambda(2110)5/2^+$, and $\Lambda(2100)7/2^-$. Figure 3.12 shows the $pK^{*-}(892)$ invariant mass distribution showing evidence for many of these overlapping states, as well as possible unknown higher mass states. The PDG does not report any baryons beyond ∼2100 MeV, where evidence for other Λ and Σ states can be seen, specifically at ∼2500 MeV and ∼3000 MeV.

Beyond the background contributions discussed to now, the $K^+K^-\pi^0$ and $K^{*\pm}K^{\mp}$ distributions are also affected by the misidentification of pions as kaons, meaning 3π phase space and the ω^0 decaying to $\pi^+\pi^-\pi^0$. If ω^0 background is present, it will produce a peak around 1500 MeV, which is discernible in Figures 3.13, 3.15, and 3.16. This problem can be remedied by analyzing data that include the DIRC, which should

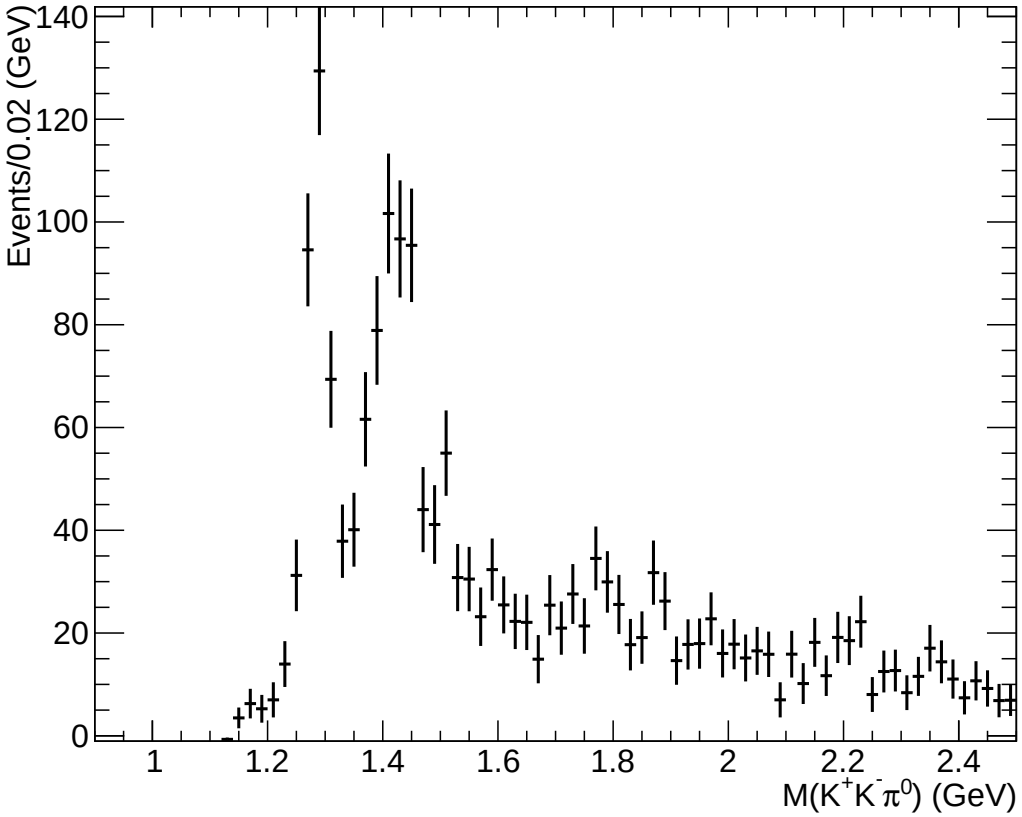

Figure 3.14: Invariant mass of $K^+K^-\pi^0$ from $\gamma p \to pK^+K^-\gamma\gamma$ events where $M(K^+K^-) < 1.0$ GeV.

improve the K/π separation, by selecting kaons with momentums less than 3 GeV, performing a background subtraction from Monte Carlo produced $\omega \to \pi^+\pi^-\pi^0$ events treating the decay products as $K^+K^-\pi^0$, or possibly through particle identification using machine learning.

3.3.4 $K\bar{K}\pi^0$, $a_0\pi^0$, and $K^*\bar{K}$

The ultimate goal of this analysis effort is to obtain PWA results for $K^*\bar{K}$, with significant focus on the low mass region where peaks for known particles are discernible. As discussed in Section 1.4.1, the goal is to contribute to the discussion of psuedoscalar meson contributions to the 1400 MeV region. Furthermore, producing

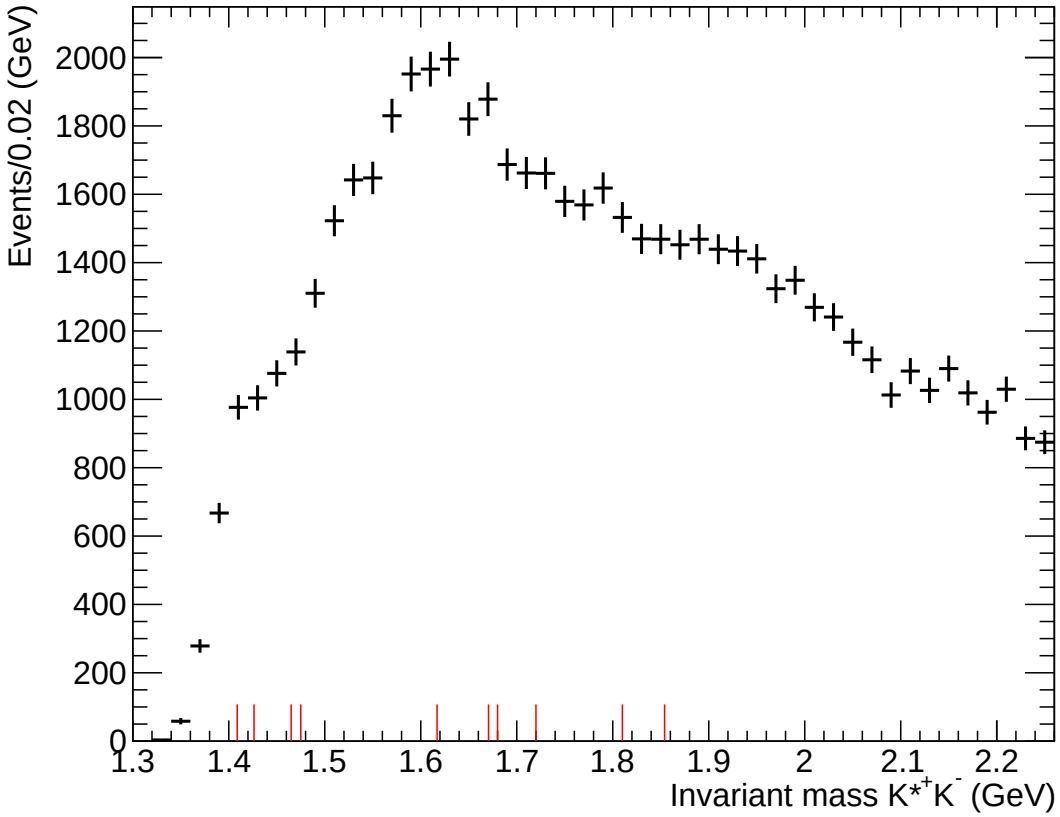

Figure 3.15: Invariant mas of $K^{*+}(892)K^-$ from $\gamma p \to pK^+K^-\gamma\gamma$ events.

results consistent with previous experiments gives confidence to searches for particles at higher masses, specifically the η_1' hybrid meson candidate.

Clear signal peaks for particles near threshold are discernible for the three body decay of mesons to $K^+K^-\pi^0$ in Figure 3.13. Signals for meson states ∼1300 MeV and ∼1500 MeV are evident indicating the possibility of $b_1(1235)$, $a_1(1260)$, $f_2(1270)$, $f_1(1285)$, $\eta(1405)$, $f_1(1420)$, and $\eta(1475)$ meson states being photoproduced. The FWHM of the peak between 1300 and 1400 MeV is ∼36.5 MeV from a Gaussian plus third degree polynomial fit. The FWHM of the peak in the 1400 MeV mass region is ∼84.59 MeV which is consistent with multiple contributions to this peak, mainly the $\eta(1405)$, $f_1(1420)$, and $\eta(1475)$ mesons Group *et al.* (2020).

It is not possible to identify higher mass peaks without PWA. The peaks between 2

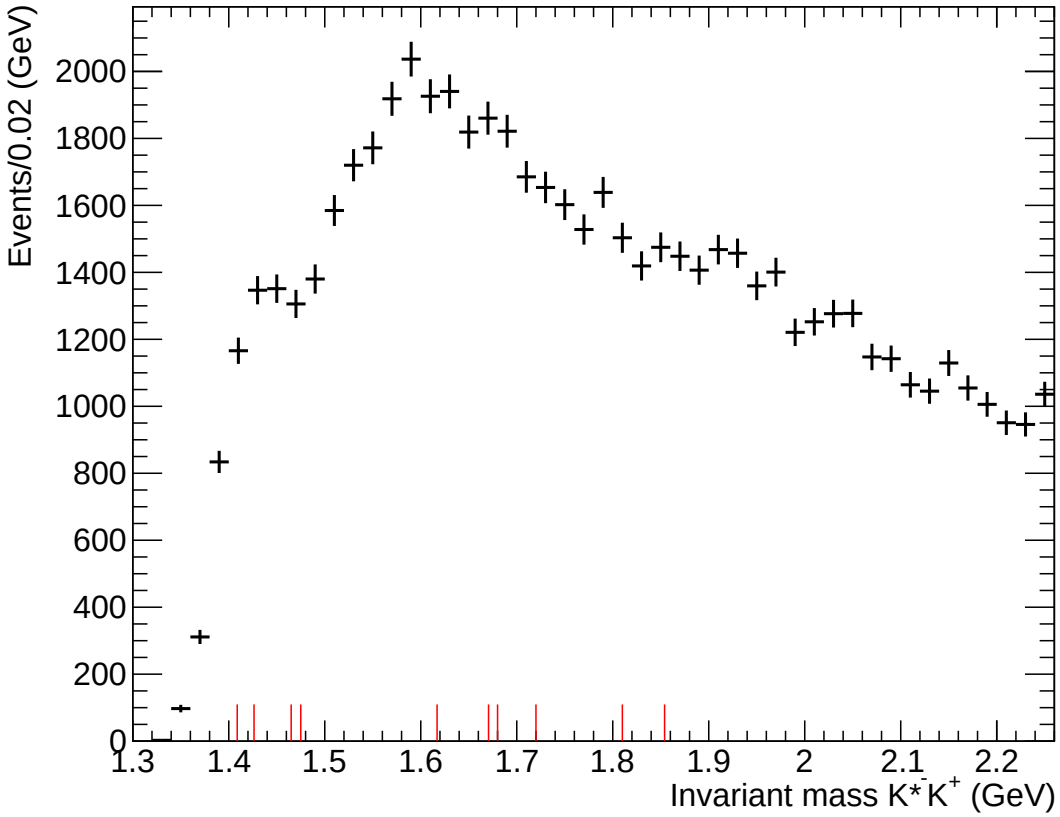

Figure 3.16: Invariant mass of $K^{*-}(892)K^{+}$ from $\gamma p \to pK^{+}K^{-}\gamma\gamma$ events.

and 2.5 GeV are of particular interest to future work because these are in the region of LQCD η_1' hybrid meson candidate. Furthermore, there is interest in searching for the η_c meson decaying $K^{+}K^{-}\pi^{0}$ because it has yet to be seen in photoproduction experiments. A small edge is visible near the η_c mass at 2983.9 MeV, but it is difficult to make any conclusions because this region of the distribution is dominated by pion contamination Group *et al.* (2020).

The two body decays of mesons to $K^{*+}(892)K^{-}$ in Figure 3.15 does not show any discernible signal peaks, except for the possibility of something near threshold as seen by the edge near 1400 MeV. However, the two body decays of mesons to $K^{*-}(892)K^{+}$ in Figure 3.15 does seem to have a visible signal peak ∼1400 MeV. This peak would be consistent with the possible production of $\eta(1405)$, $f_1(1420)$, $\rho(1450)$, and $\eta(1475)$.

Like the produced mesons decaying $K^+K^-\pi^0$, this is only resolvable through a PWA to determine the J^{PC} quantum numbers of the states.

Beyond the meson decays involving the $K^*(892)$ visible states, E852 and other experiments report mesons decaying $a_0(980)\pi^0$ where the $a_0(980)$ decays K^+K^- in this reaction topology. Despite no evidence of the $a_0(980)$ meson in the K^+K^- invariant mass distribution shown in Figure 3.9a, it is possible to select events where the invariant mass of K^+K is less than 1 GeV. If it is assumed that these include mainly the a_0 meson, then it is possible that $b_1(1235)$, $a_1(1260)$, $f_2(1270)$, $f_1(1285)$, $\eta(1405)$, $f_1(1420)$, and $\eta(1475)$ meson states are included in this decay modes, as is discernible from Figure 3.14.

3.4 Summary

It is clear that the $\gamma p \to pK^+K^-\pi^0$ reaction topology is rich with both meson and baryon states. Attention now turns to resolving what meson resonances, that decay $K^*\bar{K}$, contribute to the 1400 MeV mass region.

Chapter 4

PARTIAL WAVE ANALYSIS OF $K^*\bar{K}$,

In order to identify meson resonances that have similar masses, it is necessary to include additional information such as the J, P, and C quantum numbers of the states. The invariant mass distributions discussed in Chapter 3 contain many overlapping meson states. This is illustrated by the reported states that decay $K\bar{K}\pi^0$ within the PDG, as shown in Table 1.1. The goal is to identify low mass meson states in the $K^*\bar{K}$ invariant mass distribution using a partial wave analysis. It is important to identify these states to provide confidence in the methods used and to assist in the future search for the η_1' hybrid meson candidate. This chapter will discuss the work being done to accomplish this goal.

4.0.1 Monte Carlo

A Monte Carlo (MC) simulation was built to randomly generate samples of $K^*\bar{K}$ events isotropically through phase space. The generated events are processed through a simulation of the GlueX spectrometer to obtain efficiency corrections used within the PWA to account for trigger, detector, and reconstruction effects. Efficiency corrections are crucial to this analysis because the detector acceptance and efficiency, along with analysis cuts, help shape the mass distributions. Section 3.2.2 outlines the charged track selection criteria, which includes criteria that the kaons from an event must include one of the forward detectors. It is also required that the protons are identified by BCAL, FCAL, or TOF, meaning that the ST, CDC, and FDC are not sufficient to identify protons.

The MC for the analysis of resonances decaying $K^*\bar{K}$ required a custom generator.

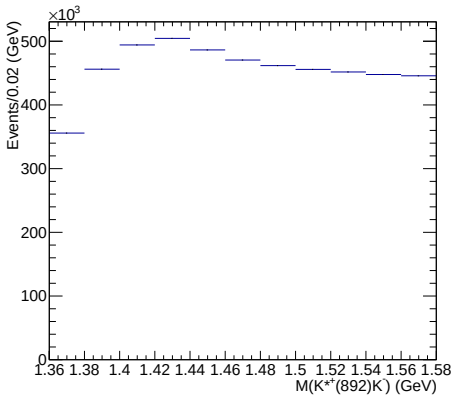

(a)

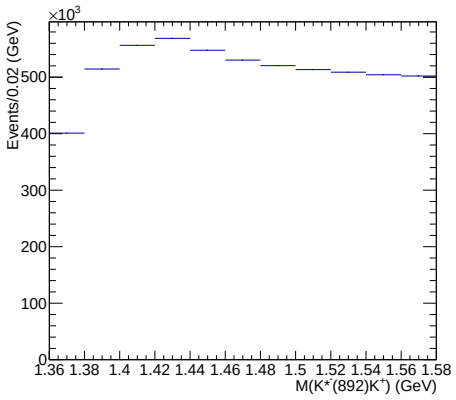

(b)

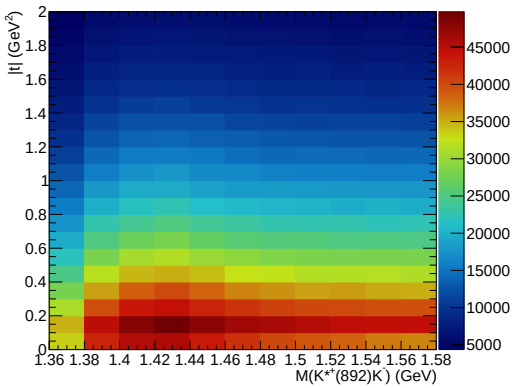

(c)

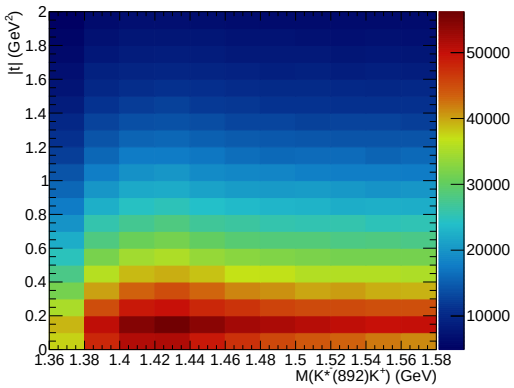

(d)

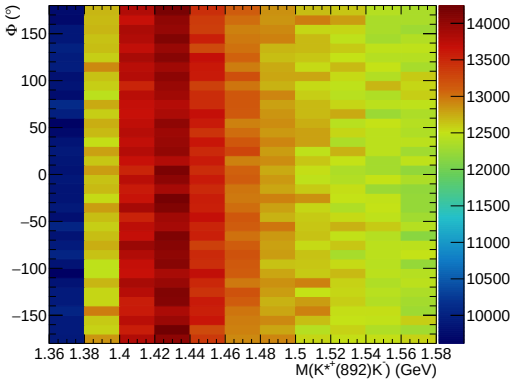

(e)

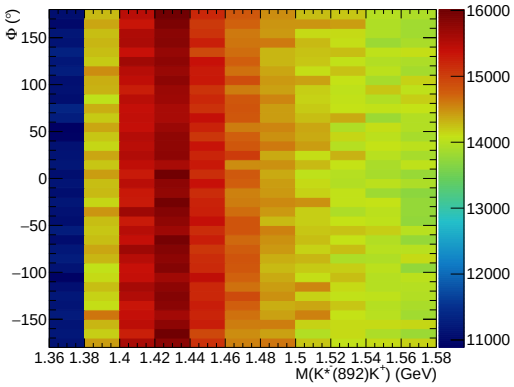

(f)

Figure 4.1: Invariant mass distribution for generated (a) $K^{*+}K^{-}$ and (b) $K^{*-}K^{+}$ events. $|t|$-Mandelstam versus invariant mass distribution for generated (c) $K^{*+}K^{-}$ and $K^{*-}K^{+}$ events. Φ versus invariant mass distribution for generated (e) $K^{*+}K^{-}$ and (f) $K^{*-}K^{+}$ events.

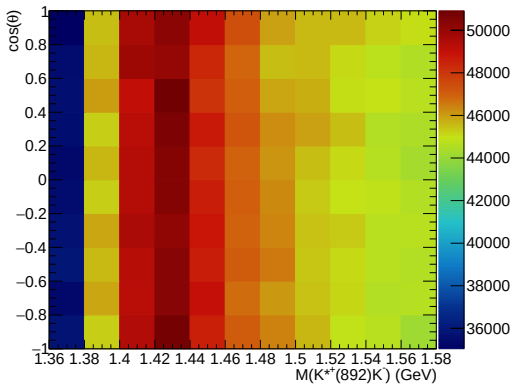

(a)

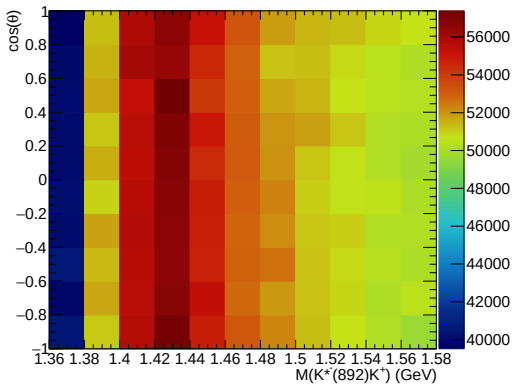

(b)

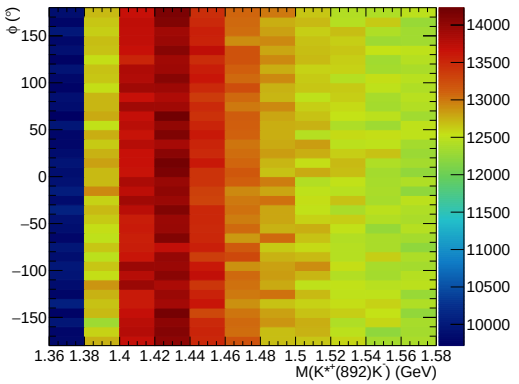

(c)

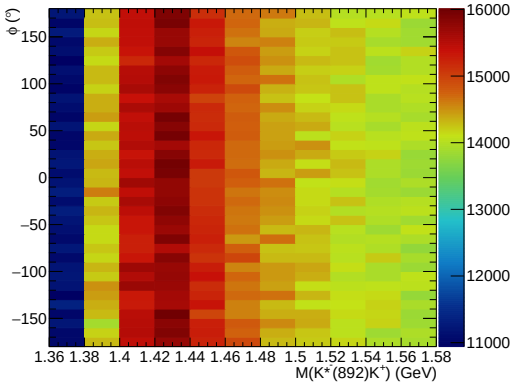

(d)

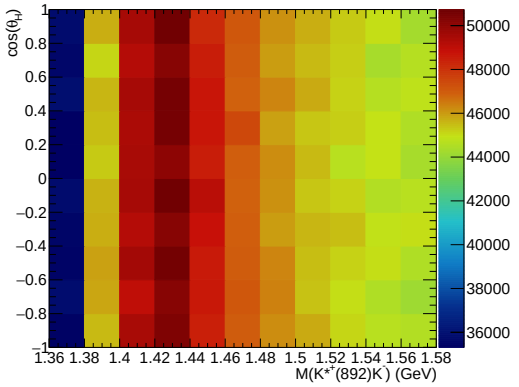

(e)

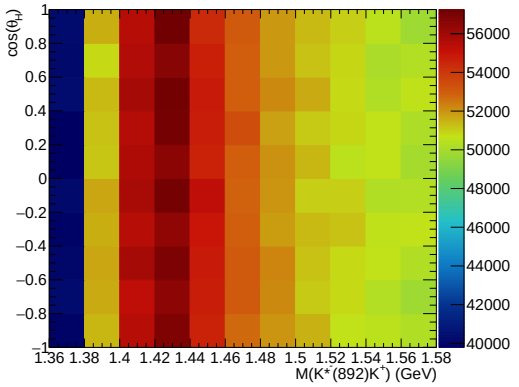

(f)

Figure 4.2: $\cos\theta$ versus invariant mass distribution for generated (a) $K^{*+}K^-$ and (b) $K^{*-}K^+$ events. ϕ versus invariant mass distribution for generated (c) $K^{*+}K^-$ and (d) $K^{*-}K^+$ events. $\cos\theta_H$ versus invariant mass distribution for generated (e) $K^{*+}K^-$ events and (f) $K^{*-}K^+$ events.

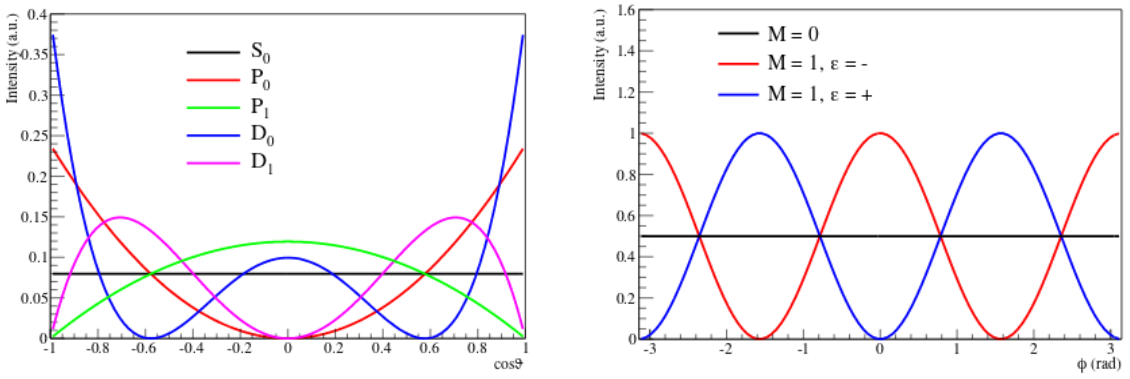

(a) (b)

Figure 4.3: (a) Expected shape for $\cos\theta$ distributions based on associated Legendre polynomials. (b) Expected shape for ϕ distributions based on different reflectivities of $e^{im\phi}$ for $m = 0, 1$.

It generates a flat incident photon energy distribution for energies from 8.2 to 8.6 GeV. With these energies, the generator produces wide mass distributions for $K^*\bar{K}$. The K^* mass distribution is given a Breit-Wigner shape defined by PDG center and width. As measured by the data, a t-slope of $1.3/\text{GeV}^2$ is used to define the momentum transfer of the production process. Figure 4.4c and 4.4d show the Madelstam $|t|$ versus the invariant mass of $K^{*+}K^-$ of the thrown MC events.

Figures 4.4a and 4.4b show the invariant mass of the $K^{*+}K^-$ and $K^{*-}K^-$ as produced by the thrown MC events. Due to the lack of *a priori* knowledge of the meson states decaying $K^*\bar{K}$ in the GlueX data, Breit-Wigner shapes are not included to model meson resonances. Future iterations of the MC could include meson resonances seen in the PWA to better model the data. This could be used to extract cross sections, as well as the t-dependence of a meson resonances beam asymmetry. These observables would assist in identifying the production process for the produced meson states.

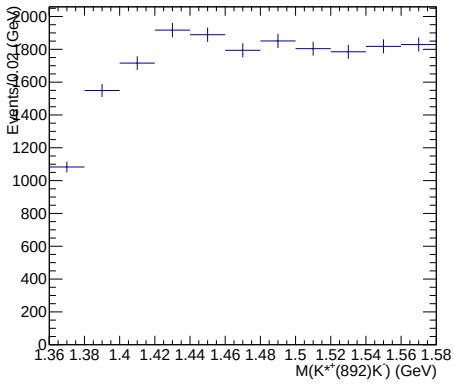

(a)

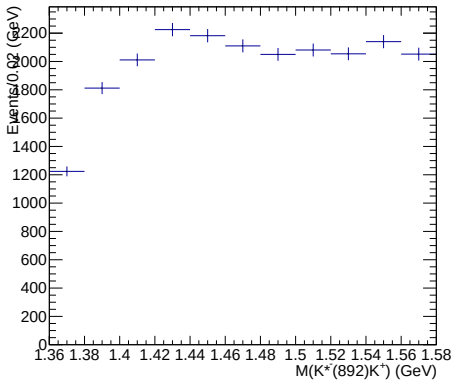

(b)

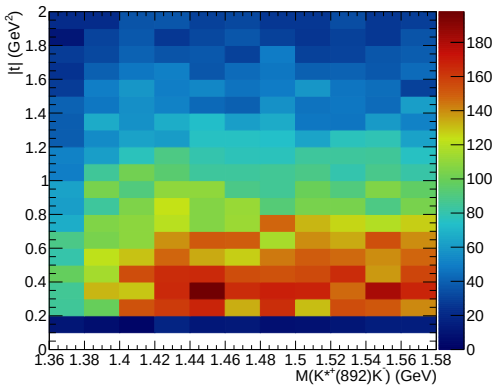

(c)

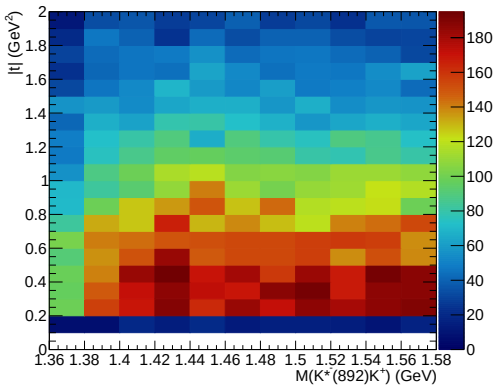

(d)

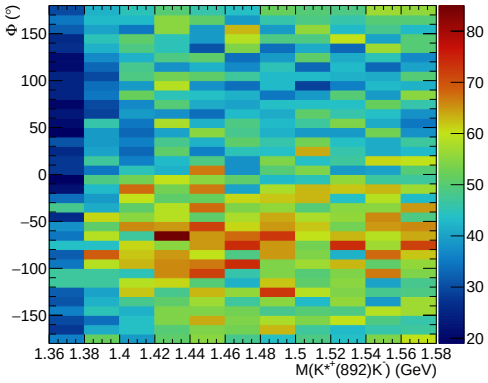

(e)

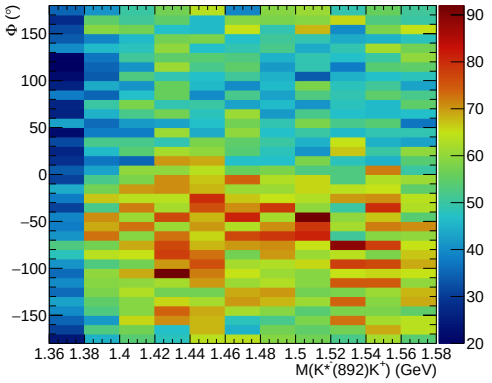

(f)

Figure 4.4: Invariant mass distribution for accepted MC (a)$K^{*+}K^-$ and (b) $K^{*-}K^+$ events. $|t|$-Mandelstam versus invariant mass distribution for accepted MC (c) $K^{*+}K^-$ and (d) $K^{*-}K^+$ events. Φ versus invariant mass distribution for accepted MC (e) $K^{*+}K^-$ and (f) $K^{*-}K^+$ events.

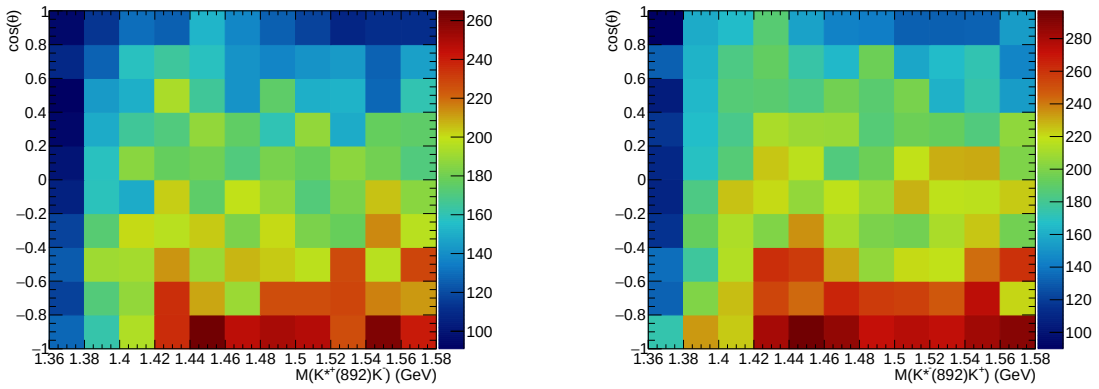

(a)

(b)

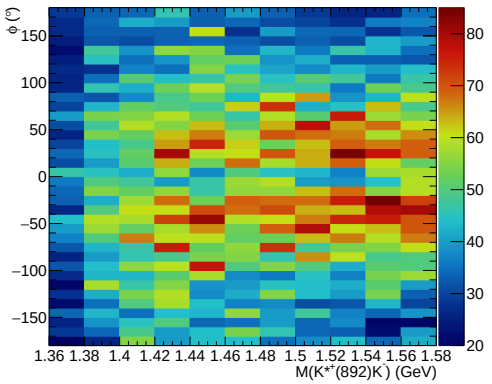

(c)

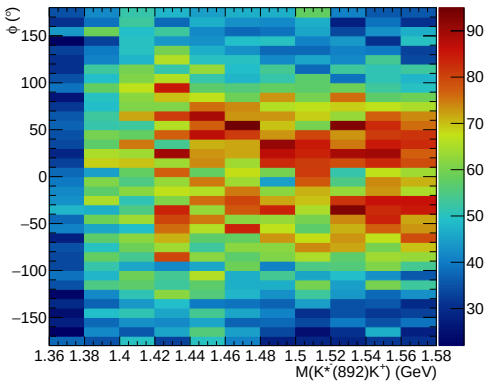

(d)

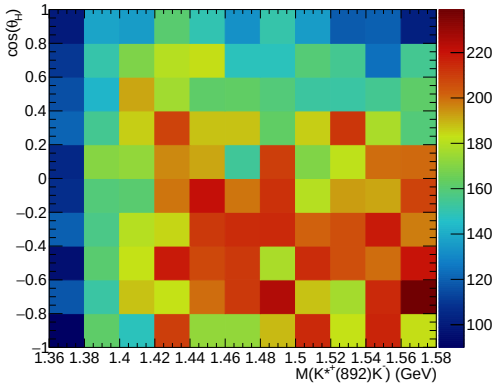

(e)

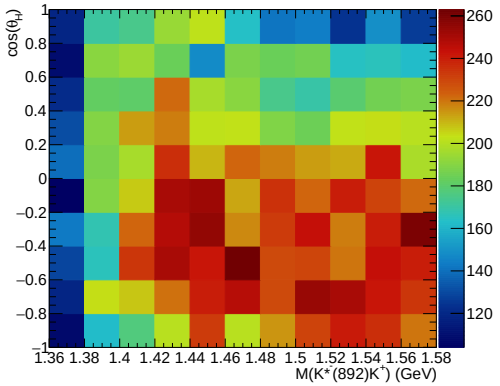

(f)

Figure 4.5: $\cos\theta$ versus invariant mass distribution for accepted (a) MC $K^{*+}K^-$ and (b) $K^{*-}K^+$ events. ϕ versus invariant mass distribution for accepted MC (c) $K^{*+}K^-$ and (d) $K^{*-}K^+$ events. $\cos\theta_H$ versus invariant mass distribution for accepted MC (e) $K^{*+}K^-$ and (f) $K^{*-}K^+$ events.

4.0.2 Angular distributions

To determine the J quantum numbers for particles that decay $K^*\bar{K}$, it is necessary to apply fits to the angular distributions described in Section 1.4.2. Before fitting the distributions, the efficiency corrected angular distributions are investigated for expected wave contributions defined in Figure 4.3 and for possible background contributions consistent with those discussed in Section 3.3.3. It is important to note that the baryon vetoes for the $\Lambda(1520)$ and $\Delta^+(1232)$ are not applied, unlike the distributions shown in Chapter 3. Figure 3.11 shows that these baryonic states hardly affect the low mass region, unlike masses greater than 2.0 GeV. Furthermore, in order to maintain the integrity of the $K^*\bar{K}$ phase space, the veto for the ϕ is not include. Future work could included methods to account for both these contributions, as well as the $a_0\pi^0$ and $K^+K^-\pi^0$ decay modes.

For incident photon beam energies within the coherent peak from 8.2 to 8.6 GeV, $K^{*\pm}K^{\mp}$ events are divided into 20 MeV bins for all $|t|$ less than 10.0 GeV^2. Binning in $|t|$ is not included due to a lack of statistics. Using the definitions of the angular distributions in Section 1.4.2, the mass dependent efficiencies are determined as the number of accepted MC events over the number of thrown events. These bin dependent efficiencies are shown Figure 4.7.

A similar trend is discernible for efficiencies of the K^* meson's polar angle in the meson resonance's rest frame for both charged states. Figures 4.7a and 4.7b show a lack of efficiency near the beam hole. The meson resonances are expected to be created mainly through t-channel processes, meaning they will have small opening angles. A K^* meson decaying from the resonance moving in a similar direction to the meson resonance may succumb to the lack of acceptance around the beam hole, and between BCAL and FCAL/TOF. If the K^* decay components or the $\bar{K}$ have

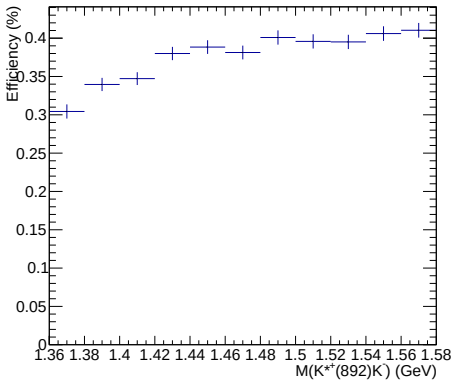

(a)

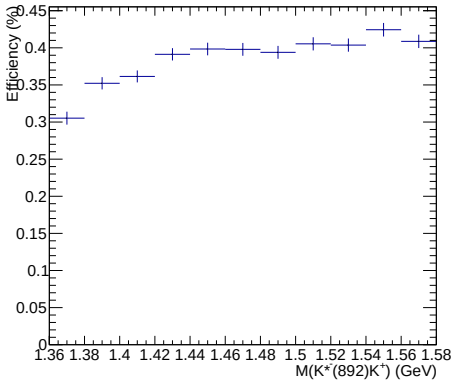

(b)

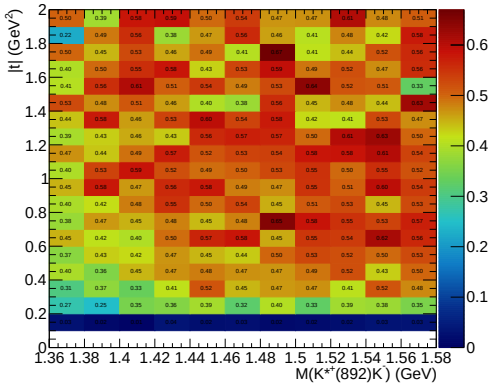

(c)

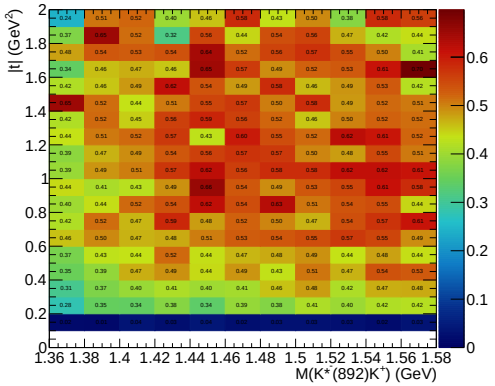

(d)

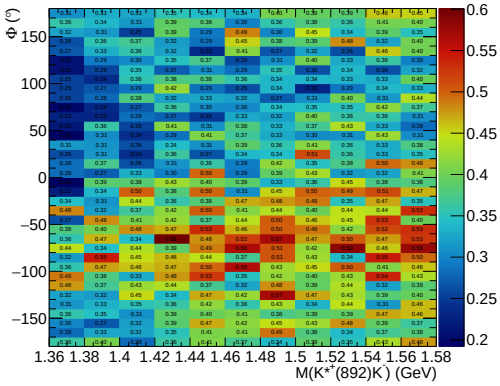

(e)

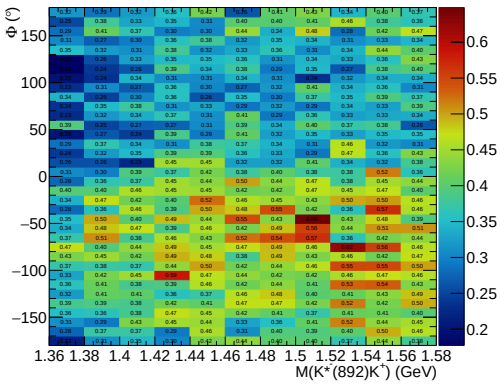

(f)

Figure 4.6: Percent efficiency for invariant mass distribution of (a) $K^{*+}K^-$ and (b) $K^{*-}K^+$ events. (c) Percent efficiency for $|t|$-Mandelstam versus invariant mass distribution of $K^{*+}K^-$ and (d) $K^{*-}K^+$ events. Percent efficiency for Φ versus invariant mass distribution of (e) $K^{*+}K^-$ and (f) $K^{*-}K^+$ events.

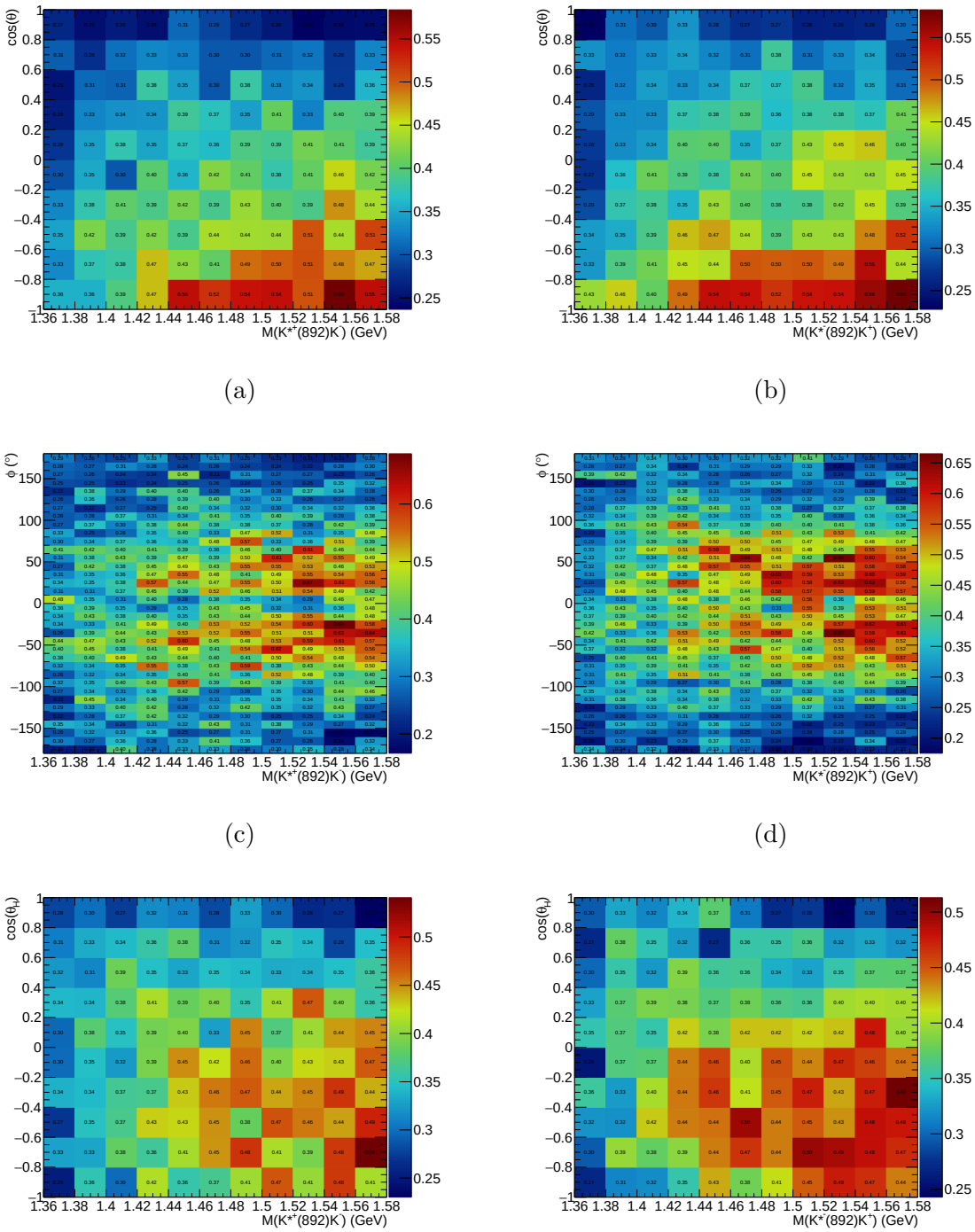

Figure 4.7: Percent efficiency for $\cos\theta$ versus invariant mass distribution of (a) $K^{*+}K^-$ and (b) $K^{*-}K^+$ events. Percent efficiency for ϕ versus invariant mass distribution of (c) $K^{*+}K^-$ and (d) $K^{*-}K^+$ events. Percent efficiency for $\cos\theta_H$ versus invariant mass distribution of (e) $K^{*+}K^-$ and (f) $K^{*-}K^+$ events.

polar angles less than 1.5°, or between 10.3° and 11.5° in the lab frame, they are removed by the analysis cuts. The efficiency increases for instances where the K^* travels transverse or anti-parallel to the resonance meson. Arguments regarding the efficiencies obtained for the K meson's polar angle in the K^* meson's rest frame follows similar logic, but to a lesser degree.

The efficiency corrected angular distributions provide some knowledge as to what waves may be contributing to the $K^*\bar{K}$ decay mode. The $cos(\theta)$ distribution in Figures 4.9a and 4.9b can be used to determine the total angular momentum of states in that mass region. It is known that the data may contain two pseudoscalar and one axial vector meson in the low mass regions. For the case of the 0^{-+} $\eta(1405)$ and $\eta(1475)$, the $\cos(\theta)$ distribution should resemble a P wave to counter the unit of angular momentum carried by the K^*. For the 1^{++} $f_1(1420)$, the $\cos(\theta)$ distribution should resemble a S_0 wave where the total angular momentum is passed through to the K^* spin.

The ϕ distributions in Figures 4.9c and 4.9d provide information regarding the reflectivity of the states. These corrected distributions indicate positive reflectivity over the mass range. If the naturality of the states were also determined, it would be possible to determine their parirty, but this requires knowledge of the production process.

4.0.3 Fitting

The PWA involves fitting a decaying particle's angular distribution with different wave contributions for varying mass bins of $K^*\bar{K}$. With the angular distributions defined in Section 1.4.2 the expected number of events seen (μ) is defined as

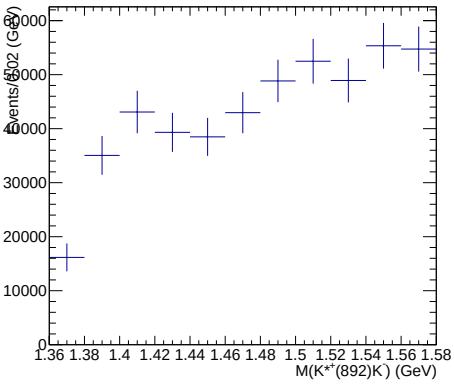

(a)

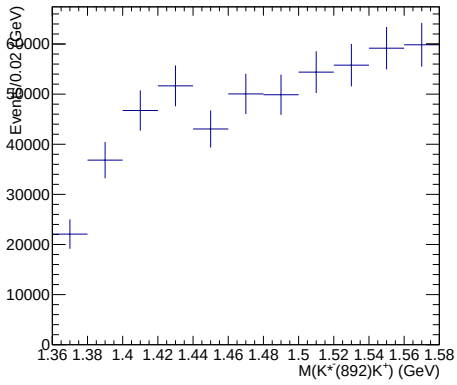

(b)

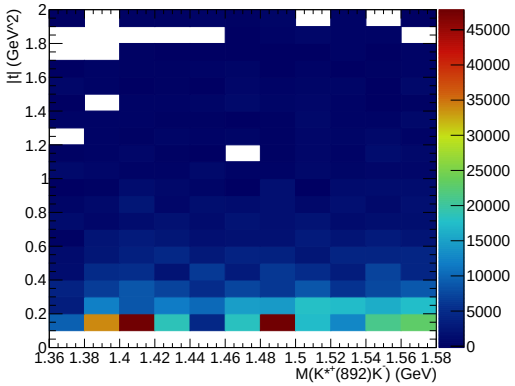

(c)

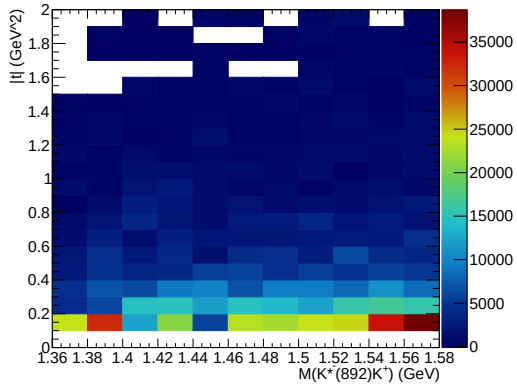

(d)

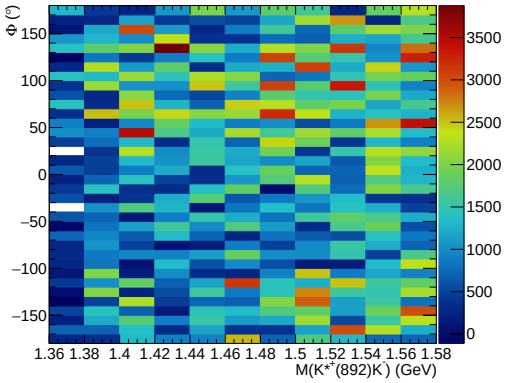

(e)

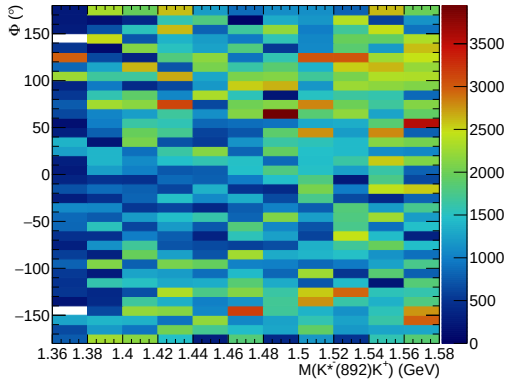

(f)

Figure 4.8: Efficiency corrected invariant mass distribution of (a) $K^{*+}K^-$ and (b) $K^{*-}K^+$ events. Efficiency corrected $|t|$-Mandelstam versus invariant mass distribution of (c) $K^{*+}K^-$ and (d) $K^{*-}K^+$ events. Efficiency corrected Φ versus invariant mass distribution of (e) $K^{*+}K^-$ and (f) $K^{*-}K^+$ events.

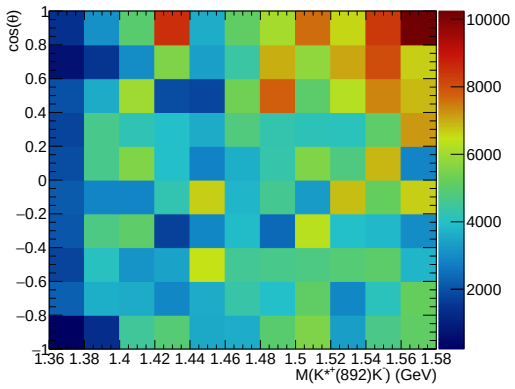

(a)

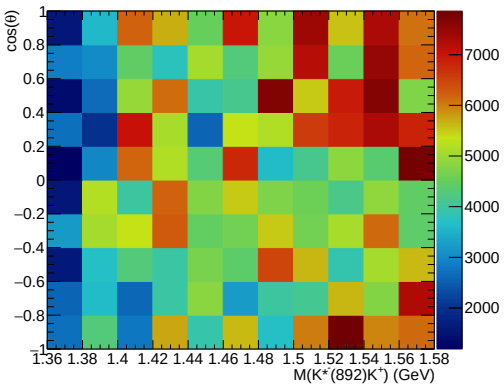

(b)

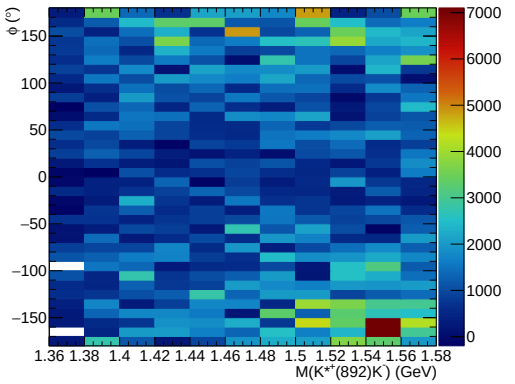

(c)

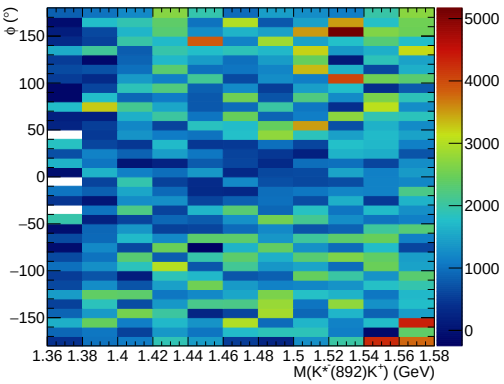

(d)

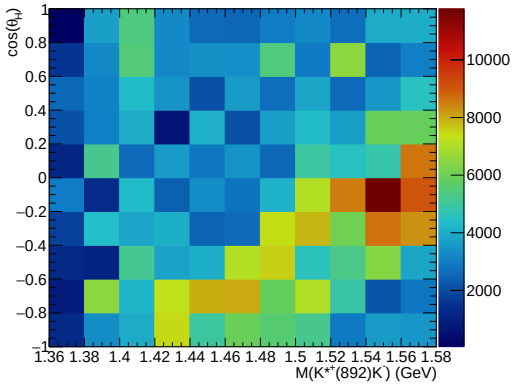

(e)

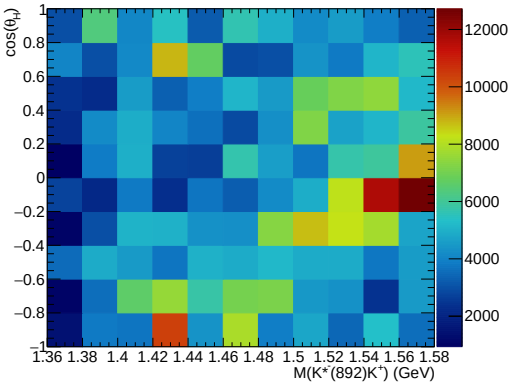

(f)

Figure 4.9: Efficiency corrected $\cos\theta$ versus invariant mass distribution of (a) $K^{*+}K^-$ and (b) $K^{*-}K^+$ events. Efficiency corrected ϕ versus invariant mass distribution of (c) $K^{*+}K^-$ and (d) $K^{*-}K^+$ events. Efficiency corrected $\cos\theta_H$ versus invariant mass distribution of (e) $K^{*+}K^-$ and (f) $K^{*-}K^+$ events.

$$\mu = \int d\Omega I(\Omega)\eta(\Omega), \tag{4.1}$$

where $\eta(\Omega)$ represents the detection efficiency. For each mass bin, an unbinned extended maximum likelihood fit is performed to determine the number of events with particular wave contributions. The likelihood function is given by

$$\mathcal{L} = \frac{e^{-\mu}}{n!} \prod_{i=1}^{n} I(\Omega_i), \tag{4.2}$$

where n is the number of $K^*\bar{K}$ mass bins. The likelihood function is minimized through its logarithmic approximation according to Sterling

$$-2\ln\mathcal{L} = 2\mu - 2\sum_{i=1}^{n} \ln I(\Omega_i) + \text{constant}, \tag{4.3}$$

where 2μ is a normalization determined by Monte Carlo integration, the sum is produced from the data, and the constant is ignored since it has no effect on minimization.

Using the intensity function defined in Equation 1.4.2, the fitting parameters are the J quantum numbers. Four sums were used for the intensity function which based on the assumption that only positive reflectivity was present, means

$$\begin{aligned} I(\Omega, \Omega_H, \Phi) = 2\kappa \sum_k [(1-P_\gamma)[|\sum_{i_N,m} [J_i^N]^{(+)}_{m,k} Im(Z)|^2 + |\sum_{i_U,m} [J_i^U]^{(+)}_{m,k} Re(Z)|^2] \\ + (1+P_\gamma)[|\sum_{i_U,m} [J_i^U]^{(+)}_{m,k} Im(Z)|^2 + |\sum_{i_N,m} [J_i^N]^{(+)}_{m,k} Re(Z)|^2]] \end{aligned} \tag{4.4}$$

is used to describe the system. The Z functions in Equation 4.4 were built according to Equations 1.22 and 1.30.

To reduce the number of fitting parameters given the lack of statistics, three sets of quantum numbers were used to fit the data for 20 MeV mass bins from 1.34 GeV to 1.58 MeV. The set of quantum numbers is presented in Table A.1. These quantum numbers were chosen based on the particles reported to decay $K^*\bar{K}$ in the PDG. Specifically, meson states with $J = 0$, 1, and 2 with their respective spin projection M from $-J$ to J were included. For the orbital angular momentum of meson resonance's decay (L), it was decided a P, S, and D wave would be included. This implies that for $J = 0$ meson states the angular momentum of the beam photon would be the orbital angular momentum of the state's break up, unlike for the $J = 1$ states where it is transferred to the meson state. As for the $J = 2$ states, the extra unit of orbital angular momentum comes from in the production process. Similar to M, the projection of orbital angular momentum (m_L) is iterated from $-L$ to L. Finally, S is the spin of the vector meson in the decay and m_S is its spin projection from $-S$ to S. It should also be noted that $M = m_L + m_S$ to maintain angular momentum conservation.

The Spring and Fall 2018 GlueX data sets were combined for fitting of the data to provide sufficient statistics given the chosen binning. Attempts to reduce the binning to 10 MeV caused failures in the fitting of the angular distributions. Eight subsets of this data were created consisting of the four polarization angles, and the decay modes $K^{*+}K^-$ or $K^{*-}K^+$. A simultaneous fit was applied to the angular distributions with constraints applied to identical fitting parameters between the eight data subsets. To reduce fit parameters, the $[J_i^N]_{m,k}^{(+)}$ terms in the first and third sum of Equation 4.4 are constrained. Similarly, $[J_i^U]_{m,k}^{(+)}$ terms in the second and fourth sum are also constrained. The simultaneous fitting is conducted to decrease statistical uncertainties by combining as many of the polarization and decay modes possible. Furthermore, it is expected that observed states should decay through both $K^{*+}K^-$

and $K^{*-}K^{+}$.

To clarify details of PWA fit, 96 fitting parameters are required to fit the data with three sets of waves each having four terms in Equation 4.4 for the eight data subsets. By simultaneously fitting the eight data subsets this becomes 12 fitting parameters. By constraining the like $[J]^{+}_{m,k}$ terms in Equation 4.4, only 6 unique parameters are required in the fit. Finally, the imaginary part of the $J = 0$ wave set is fixed at zero, meaning its contribution is only real. Therefore, the PWA only requires 5 parameters to complete the fit, which are used to determine the fractional contributions of each total angular momentum J in the data.

A sample of the PWA fit results for the 1520 to 1540 MeV mass bin are shown in Figure 4.10. The $\cos\theta$ fit shows evidence of interfering P waves of differing m_L on top of an incoherent additional S wave. These wave types are consistent with an $L = 1$ $\eta(1405)$ and $\eta(1475)$, and $L = 0$ $f_1(1420)$ as reported by E852. The ϕ distribution is consistent with positive reflectivity, meaning knowledge of the naturality of the particle exchange would make obtaining the parity of a state in this region possible. The $\cos\theta_H$ distributions parabolic shape for a P wave supports a vector meson being the decay component as expected for the K^*.

Results for the rest of the fits are shown in Appendix B. Before presenting results of the fit, it is necessary to explain how the errors are determined from the fitting.

4.0.4 Error determination

The uncertainties produced by the PWA tools are inaccurate. As a result, a method is employed to estimate the uncertainty in each mass bin for a given total angular momentum. As described, the fit is a simultaneous fit over eight subsets of the total $\gamma p \to pK^*\bar{K}$ events for mass bins from 1.34 to 1.58 GeV, meaning eight distributions for each J are obtained for the three angles. In order to determine the

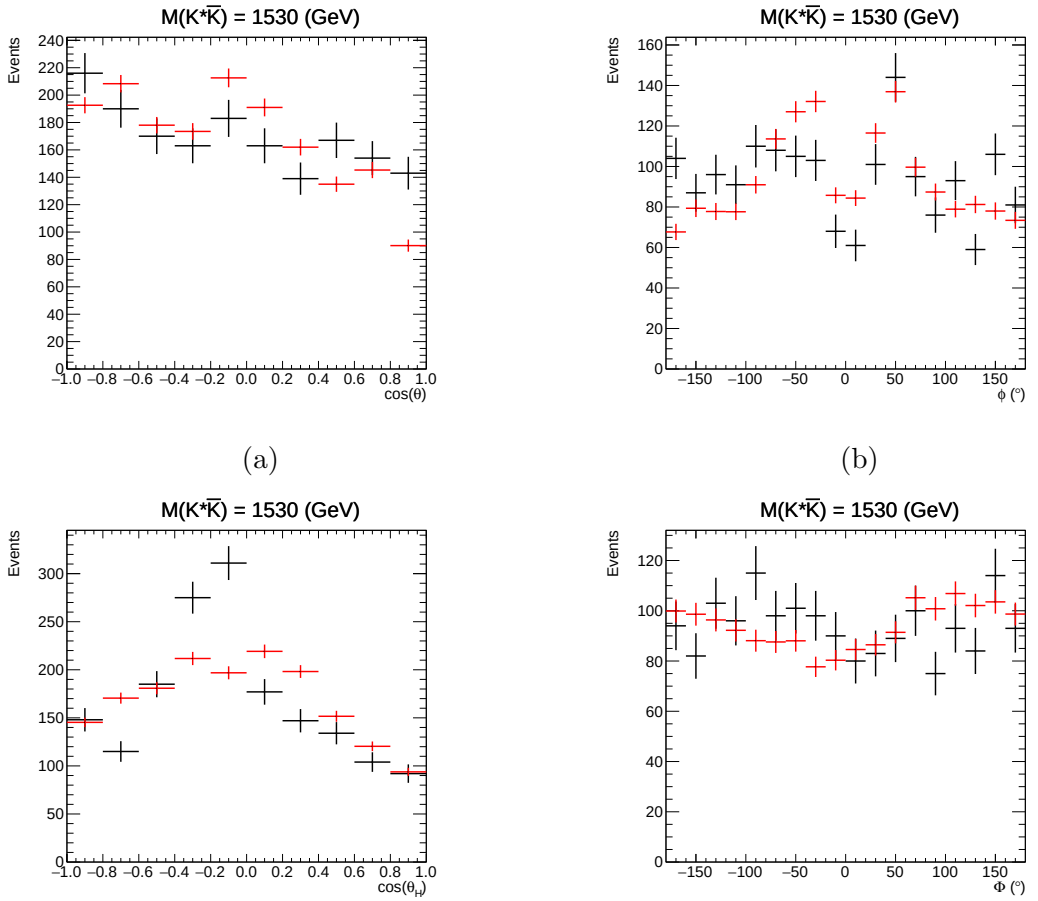

Figure 4.10: Data (black) and PWA fit results (red) for (a) $\cos\theta$, (b) ϕ, (c) $\cos\theta_H$, and (d) Φ for the 1520 to 1540 MeV mass bin.

uncertainty, the PWA fit is examined using a refit of the PWA to the data.

First, the fits and data for the four polarization are combined into their respective histograms for the different angular momentums and each charged decay mode, $K^{*+}K^-$ and $K^{*-}K^+$. The four angles $(\theta, \theta_H, \phi, \Phi)$ are plotted on the same histogram as shown in Figure 4.11. From left to right, the plot is broken up into $\cos\theta$ (first ten bins), $\cos\theta_H$ (second ten bins), ϕ (next eighteen bins), and Φ (next eighteen bins). A fitting function is built with the $J = 0$, 1, and 2 histograms resulting from the PWA where the total is a linear combination of these histograms. If the histograms are

defined as h_J, then

$$h_{tot} = a_0 h_0 + a_1 h_1 + a_2 h_2 + C, \tag{4.5}$$

where a_0, a_1, a_2, and C are the fit parameters, where $a_n = 1$ and $C = 0$ for a perfect fit. A fit to the data is applied with the function of the linear combination of the PWA fit in Equation 4.5, where the a fit parameters are limited to vary between 0.95 and 1.05. The uncertainties of the fit parameters are

$$\sigma_m = \frac{\sigma_{a_n}}{a_n} m, \tag{4.6}$$

where σ_{a_n} is a fit parameter uncertainty, a_n is a fit parameter, m is the bin content of the invariant mass distribution, and σ_m is the new error for the invariant mass bin.

The fractional uncertainties for each mass bin are shown in Figures 4.12, 4.13, and 4.14. Fits for the other mass bins can be found in Appendix C.

4.1 Results

The fitting routine provides a J spin state's fractional contribution for each $K^*\bar{K}$ mass bin, making it possible to plot the invariant mass of $K^*\bar{K}$ for the $J = 0$, 1, and 2 as outlined in Table A.1. With the invariant mass distributions corresponding to each J value of the fit, a search for meson resonances decaying $K^*\bar{K}$ can be carried out. The discussion of the findings will begin with $J = 0$ meson states decaying $K^*\bar{K}$.

As outlined in Section 1.4.1, one of the goals of this analysis effort is to determine whether two pseudoscalar mesons exist in the 1400 MeV mass region. Figure 4.15 shows the results of the PWA for $J = 0$ states. Two peaks are discernible in this distribution near 1400 MeV and 1480 MeV. According to the PDG and past experiments, two pseudoscalar mesons have been identified in these regions. To assist in

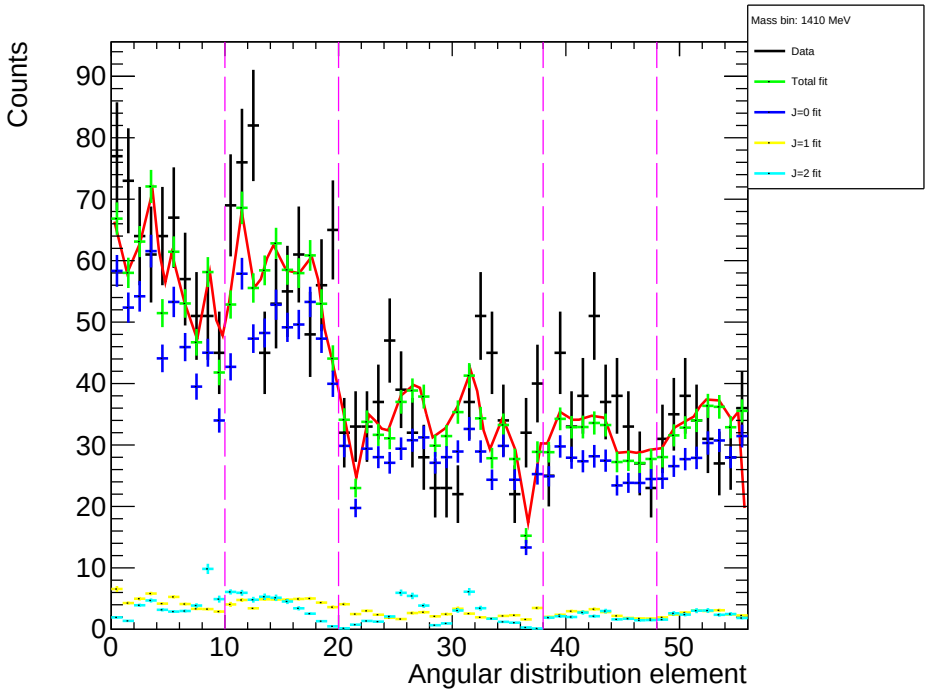

Figure 4.11: Sample fit for the determination of the fractional uncertainty for each mass bin.

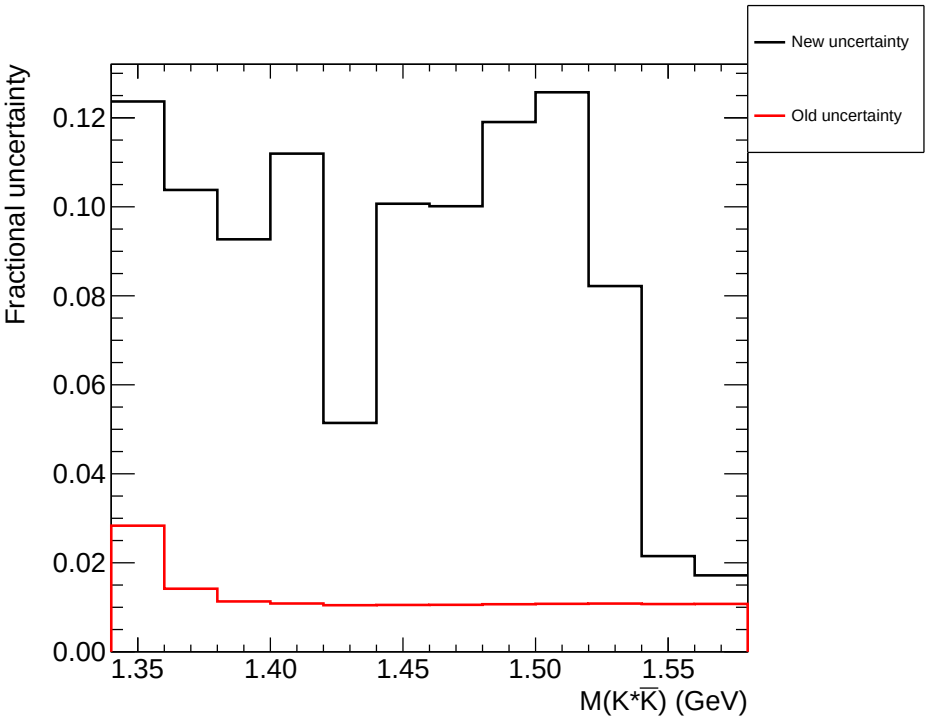

Figure 4.12: Fractional uncertainty from the fit method (black) and from the PWA (red) for $J = 0$.

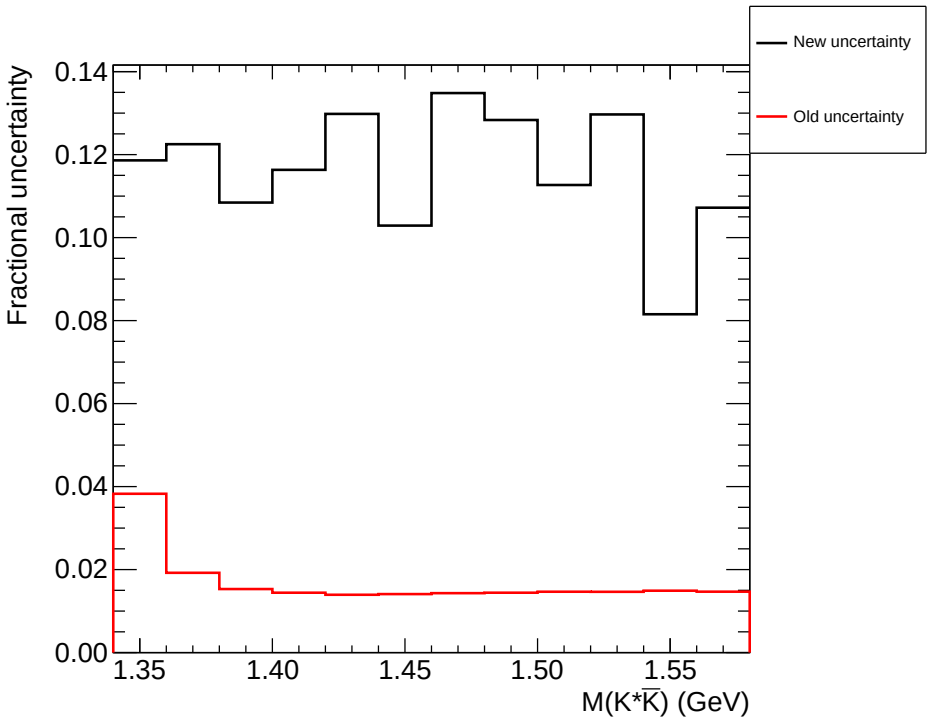

Figure 4.13: Fractional uncertainty from the fit method (black) and from the PWA (red) for $J = 1$.

confirming the possible existence of these particles, two Gaussians with a third-degree polynomial are fit to the distribution

$$f_0(M(K^*\bar{K})) = [\text{p0}]e^{-\frac{M-[\text{p1}]}{2[\text{p2}]^2}} + [\text{p3}]e^{-\frac{M-[\text{p4}]}{2[\text{p5}]^2}} + [\text{p6}]M^3 + [\text{p7}]M^2 + [\text{p8}]M + [\text{p9}]. \quad (4.7)$$

The Gaussians' centers ($[\text{p1}], [\text{p4}]$) and widths ($[\text{p2}], [\text{p5}]$) are seeded with the PDG masses and widths for the $\eta(1405)$ and $\eta(1475)$* . The center and width of the Gaussian for the $\eta(1405)$ and $\eta(1475)$ are free to vary near their respective PDG values. An increase in the parameter limits is applied until no parameter returns "at limit" in the fit routine, ensuring minimization in the parameter space. The third

* The PDG reported widths are for Breit-Wigner, meaning the seeding is $\sigma = \Gamma/2.355$ for the Gaussian standard deviation.

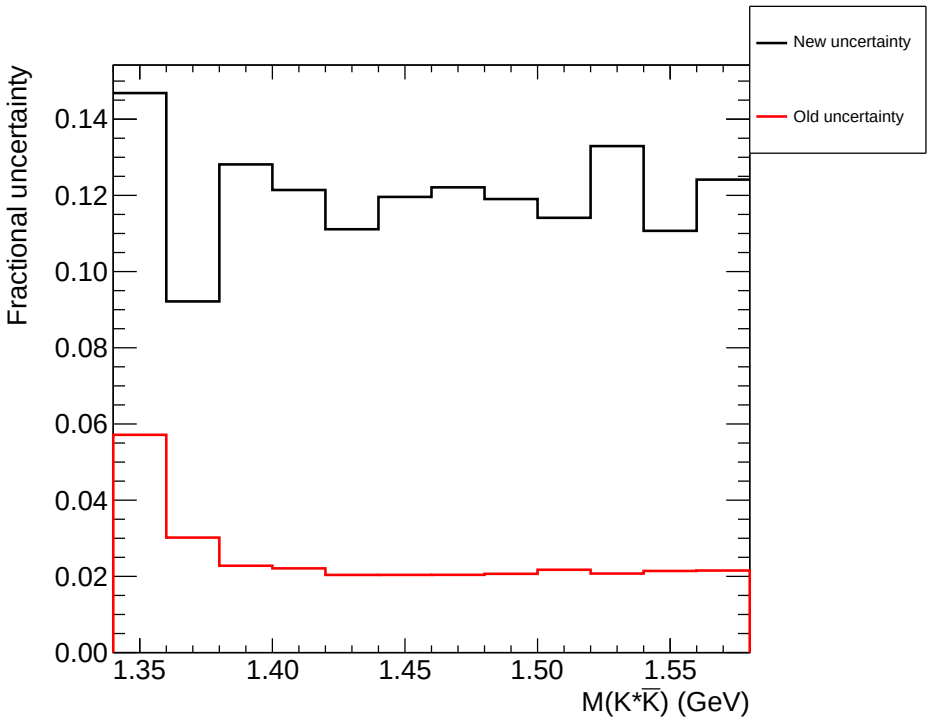

Figure 4.14: Fractional uncertainty from the fit method (black) and from the PWA (red) for $J = 2$.

degree polynomial is used to model the background. Table 4.1 reports the PDG values compared to those of the fit histograms.

Beyond the pseudoscalar mesons identified in the 1400 MeV region, the $f_1(1420)$ axial vector meson is reported to exist by multiple experiments. As stated, the $\eta(1405)$ and $f_1(1420)$ is where the $E\iota$ puzzle emerged. In Figure 4.16, two peaks are discernible in this distribution near 1440 MeV and 1510 MeV. Two axial vector mesons have been identified in these regions in previous experiments, specifically the $f_1(1420)$ and $f_1(1510)$. A fit with two Gaussians and an exponential is applied to the $J = 1$ distribution using

$$f_1(M(K^*\bar{K})) = [\text{p0}]e^{-\frac{M-[\text{p1}]}{2[\text{p2}]^2}} + [\text{p3}]e^{-\frac{M-[\text{p4}]}{2[\text{p5}]^2}} + e^{[\text{p6}]M+[\text{p7}]}, \tag{4.8}$$

where the centers $([\text{p1}], [\text{p4}])$ and widths $([\text{p2}], [\text{p5}])$ of the Gaussians are set to the

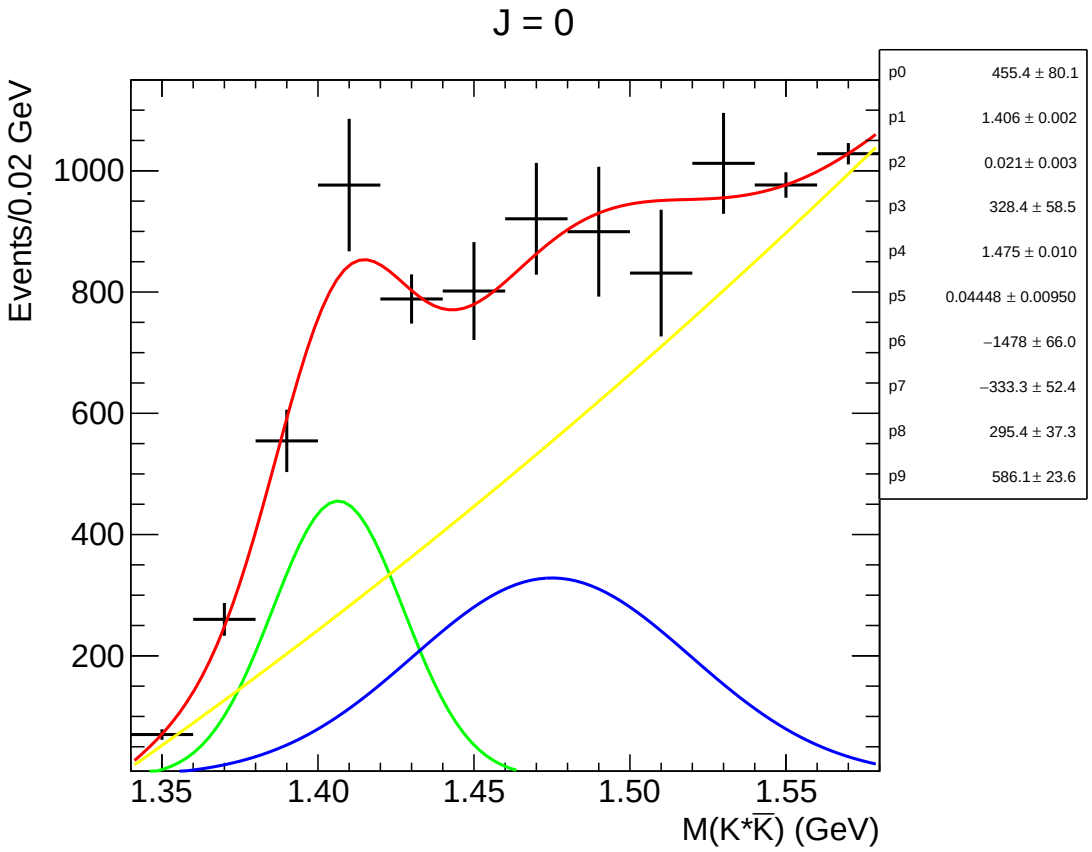

Figure 4.15: Invariant mass distribution for $K^*\bar{K}$ with $J = 0$ as determined by PWA. Red line shows total fit to the data. Green is a Gaussian for $\eta(1405)$ and blue is a Gaussian for the $\eta(1475)$. Yellow line models a smooth background contribution with a third-degree polynomial.

PDG reported values for the $f_1(1420)$ and $f_1(1510)$, respectively. All parameters are free to vary near their respective PDG values. An exponential is added to model the background. Table 4.1 reports the PDG values compared to those of the fitting routine.

Initially a $J = 2$ wave was introduce as a means to handle background contributions from tensor meson states above 1500 MeV. Two possible meson states are visible in this distribution, as is discernible in Figure 4.17. A fit with three Gaussians is applied to this distribution:

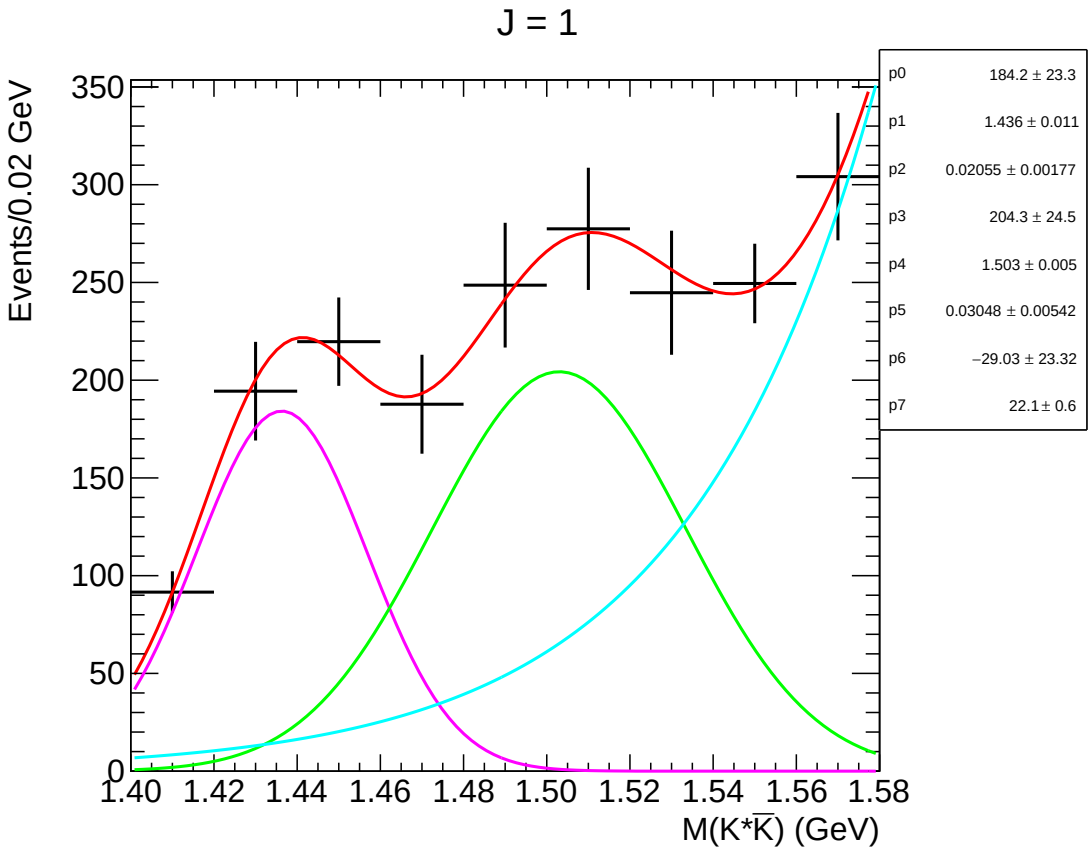

Figure 4.16: Invariant mass distribution for $K^*\bar{K}$ with $J = 1$ as determined by PWA. Red line shows total fit to the data. Magenta line shows a Gaussian for $f_1(1420)$ and green shows a Gaussian for the $f_1(1510)$. The cyan line shows the background modeled by an exponential.

$$f_2(M(K^*\bar{K})) = [\text{p0}]e^{-\frac{M-[\text{p1}]}{2[\text{p2}]^2}} + [\text{p3}]e^{-\frac{M-[\text{p4}]}{2[\text{p5}]^2}} + [\text{p6}]e^{-\frac{M-[\text{p7}]}{2[\text{p8}]^2}}. \tag{4.9}$$

The first Gaussian's center and width ([p1], [p2]) are fixed to the $f_2(1270)$ PDG values, since it is possible that leakage from the right tail of this meson state's distribution is present. The other Gaussians in this distribution had no fixed parameters, but were seeded to the PDG values for the $f_2(1430)$ center and width ([p4], [p5]), and $f_2'(1525)$ center and width ([p7], [p8]). The second Gaussian could be the $f_2(1430)$, a state seen in $K\bar{K}$ and $\pi\pi$ decay modes that needs confirmation. This could introduce a new decay mode for this state and further establish as a known state. Currently,

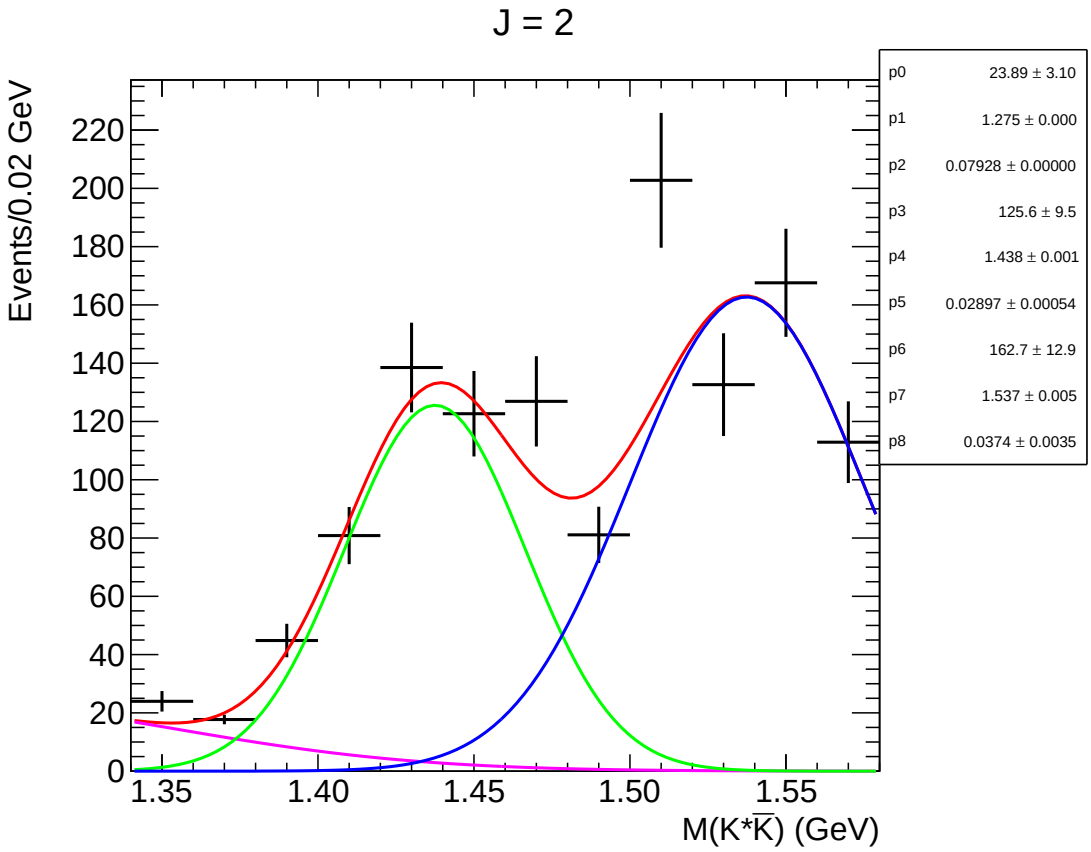

Figure 4.17: Invariant mass distribution for $K^*\bar{K}$ with $J = 1$ as determined by PWA. Red line shows total fit to the data. Green line shows a Gaussian for $f_2(1430)$ and blue shows a Gaussian for the $f_2'(1525)$. The magneta line shows the background modeled by a Gaussian for the $f_2(1260)$.

the PDG lists the state as requiring additional confirmation. The final Gaussian is the $f_2'(1525)$, which would add a production mechanism to a well established meson state. Table 4.1 reports the PDG values compared to those of the fitting routine.

To provide further confidence in the results, the fit results are presented split between the decay modes with alternate charged states, specifically the $K^{*+}K^-$ and $K^{*-}K^+$. Figure 4.18 shows the results of the invariant mass distribution results from PWA with similar values to those in Table 4.1 for the center and widths of the identified particles.

J	PID	PDG center (MeV)	PDG width (MeV)	Fit center (MeV)	Fit width (MeV)
0	$\eta(1405)$	1408.8 ± 2.0	50.1 ± 2.6	1406 ± 2	49.46 ± 7.07
0	$\eta(1475)$	1475 ± 4	90 ± 9	1475 ± 10	105.8 ± 224
1	$f_1(1420)$	1426.3 ± 0.9	54.5 ± 2.6	1436 ± 11	48.40 ± 4.17
1	$f_1(1510)$	1518 ± 5	73 ± 25	1503 ± 5	71.78 ± 12.76
2	$f_2(1430)$	$\sim$1430	NA	1438 ± 1	68.22 ± 1.27
2	$f_2(1525)$	1517.4 ± 2.5	86 ± 5	1537 ± 5	88.10 ± 8.24

Table 4.1: Comparison of the fit parameters for Figures 4.15, 4.16, and 4.17 with respect to the PDG*.

4.2 Summary

Possible evidence for pseudoscalar mesons $\eta(1405)$ and $\eta(1475)$, axial vector mesons $f_1(1420)$ and $f_1(1510)$, and tensor mesons $f_2(1430)$ and $f_2'(1525)$ from PWA results with $J = 0$, 1, and 2 wave contributions have been presented

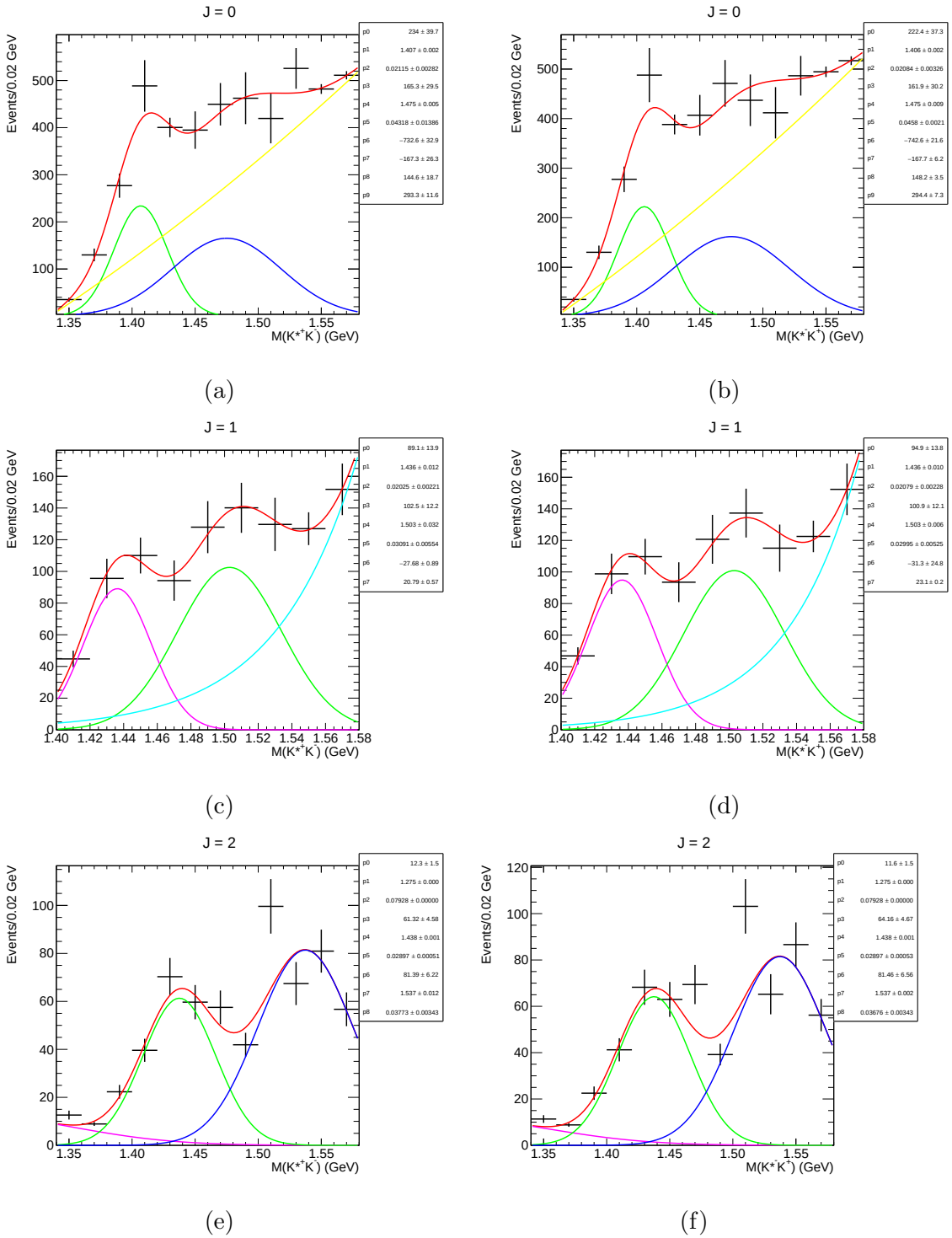

Figure 4.18: $K^{*+}K^{-}$ (left) and $K^{*-}K+$ (right) invariant mass distributions for $J = 0$ top, $J = 1$ middle, and $J = 2$ bottom.

Chapter 5

DISCUSSION

The GlueX experiment aims to map the light hybrid meson spectrum using PWA to identify of J^{PC} quantum numbers. By identifying states and assigning them to their respective nonets, the quark gluonic content of extraneous states may be identifiable.

Mesons with masses in the 1400 MeV mass region historically come with controversy. The problem of the $E\iota$ puzzle has evolved, becoming an issue as to whether two pseudoscalar mesons exist in this low mass region. Results from this PWA show evidence for two pseudoscalar mesons in the low mass region, specifically the $\eta(1405)$ and $\eta(1475)$. Alongside these two pseudoscalars, if it is true that the $\eta(1295)$ exists, then one of these particles may consist mainly of gluonic content. Assuming the $\eta(1295)$ and $\eta(1475)$ are the radial excitations of the η and η', then they would be the isoscalar partners to their nonet with the $\pi(1300)$ isovector. Coupled with the results of $\gamma\gamma$ collisions from L3, this implies that the $\eta(1405)$ is a glueball candidate. However, more work is necessary to confirm the existence of the $\eta(1295)$ to assist in determining the quark-gluon content of these meson states. Furthermore, the photoproduction of glueballs is expected to be suppressed, meaning the quark-gluonic content of these η states may need another explanation.

The axial vector meson states seen decaying $K^*\bar{K}$ in this analysis also come with controversy. Currently, the $f_1(1295)$ and $f_1(1420)$ contribute to the pseudovector nonet alongside the $a_1(1260)$ and K_{1A}. Evidence of the $f_1(1510)$ fuels the debate as to whether it or the $f_1(1420)$ is the $s\bar{s}$ isoscalar of this nonet. Confirmation of their quark content could be made by the K_L experiment out of hall D at Jefferson Lab. If the $f_1(1420)$ is not identified by the K_L experiment or it is heavily suppressed, but

the $f_1(1510)$ is identified, then the $f_1(1510)$ is the more likely $s\bar{s}$ candidate for the nonet. As a result, the hybrid meson, tetraquark, or $K^*\bar{K}$ molecule models for the $f_1(1420)$ would need further investigation.

Finally, possible evidence for two 2^{++} tensor mesons are reported, the $f_2(1430)$ and the $f_2'(1525)$. According to the PDG, the $f_2'(1525)$ is a well established state, that could be the isoscalar contribution to the nonet with the $f_2(1270)$ and isovector $a_2(1320)$. The existence of the $f_2(1430)$ gives rise to an analogous problem for determining which of these mesons contribute to the nonet and determining their quark-gluonic content. Efforts should be made to further investigate the $f_2(1430)$.

Coupled with previous experimental evidence, a discernible pattern exists in the PWA results for $K^*\bar{K}$ that could improve our understanding of the nonets for the pseudoscalar, pseudovector, and tensor mesons. Efforts should be made to expand the PWA to simultaneously fit the $K^*\bar{K}$, $a_0\pi^0$, $\phi\pi^0$, and $K^+K^-\pi^0$ to confirm these results, as well as focus attention on parity determination. These efforts would assist in establishing the spectrum for these meson states and bring us closer identifying states beyond the Constituent Quark Model.

URL https://commons.wikimedia.org/wiki/File:Meson_nonet_-_spin_0.svg (Accessed 2021).

URL https://commons.wikimedia.org/wiki/File:Meson_nonet_-_spin_1.svg (Accessed 2021).

URL https://commons.wikimedia.org/wiki/File:Baryon_octet.svg (Accessed 2021).

URL https://commons.wikimedia.org/wiki/File:Baryon_decuplet.svg (Accessed 2021).

Aaij, R., C. Abellán Beteta, B. Adeva, M. Adinolfi, C. Aidala, Z. Ajaltouni, S. Akar, P. Albicocco, J. Albrecht, F. Alessio and et al., "Amplitude analysis of bk+k decays", Physical Review Letters **123**, 23, URL http://dx.doi.org/10.1103/PhysRevLett.123.231802 (2019).

Ablikim, M., M. N. Achasov, O. Albayrak, D. J. Ambrose, F. F. An, Q. An, J. Z. Bai, R. Baldini Ferroli, Y. Ban, J. Becker and et al., "Study of(3686)kkdecays", Physical Review D **87**, 9, URL http://dx.doi.org/10.1103/PhysRevD.87.092006 (2013).

Ablikim, M., J. Z. Bai, Y. Bai, Y. Ban, X. Cai, H. F. Chen, H. S. Chen, H. X. Chen, J. C. Chen, J. Chen and et al., "Measurements ofj/decays intokk,kkandks0k", Physical Review D **77**, 3, URL http://dx.doi.org/10.1103/PhysRevD.77.032005 (2008).

Adams, G., T. Adams, Z. Bar-Yam, J. Bishop, V. Bodyagin, D. Brown, N. Cason, S. Chung, J. Cummings, K. Danyo, A. Demianov, S. Denisov, V. Dorofeev, J. Dowd, P. Eugenio, X. Fan, A. Gribushin, R. Hackenburg, M. Hayek, J. Hu, E. Ivanov, D. Joffe, I. Kachaev, W. Kern, E. King, O. Kodolova, V. Korotkikh, M. Kostin, J. Kuhn, V. Lipaev, J. Losecco, M. Lu, J. Manak, J. Napolitano, M. Nozar, C. Olchanski, A. Ostrovidov, T. Pedlar, A. Popov, D. Ryabchikov, A. Sanjari, L. Sarycheva, K. Seth, N. Shenhav, X. Shen, W. Shephard, N. Sinev, D. Stienike, S. Taegar, D. Thompson, A. Tomaradze, I. Vardanyan, D. Weygand, D. White, H. Willutzki and A. Yershov, "Observation of pseudoscalar and axial vector resonances in pk+k0n at 18 gev", Physics Letters B **516**, 3, 264–272, URL https://www.sciencedirect.com/science/article/pii/S0370269301009510 (2001).

Adhikari, S., C. Akondi, H. Al Ghoul, A. Ali, M. Amaryan, E. Anassontzis, A. Austregesilo, F. Barbosa, J. Barlow, A. Barnes and et al., "The gluex beamline and detector", Nuclear Instruments and Methods in Physics Research Section A: Accelerators, Spectrometers, Detectors and Associated Equipment **987**, 164807, URL http://dx.doi.org/10.1016/j.nima.2020.164807 (2021).

Ahohe, R., D. M. Asner, S. A. Dytman, W. Love, S. Mehrabyan, J. A. Mueller, V. Savinov, Z. Li, A. Lopez, H. Mendez, J. Ramirez, G. S. Huang, D. H. Miller, V. Pavlunin, B. Sanghi, E. I. Shibata, I. P. J. Shipsey, G. S. Adams, M. Chasse,

M. Cravey, J. P. Cummings, I. Danko, J. Napolitano, H. Muramatsu, C. S. Park, W. Park, J. B. Thayer, E. H. Thorndike, T. E. Coan, Y. S. Gao, F. Liu, R. Stroynowski, M. Artuso, C. Boulahouache, S. Blusk, J. Butt, E. Dambasuren, O. Dorjkhaidav, J. Li, N. Menaa, R. Mountain, R. Nandakumar, R. Redjimi, R. Sia, T. Skwarnicki, S. Stone, J. C. Wang, K. Zhang, S. E. Csorna, G. Bonvicini, D. Cinabro, M. Dubrovin, A. Bornheim, S. P. Pappas, A. J. Weinstein, R. A. Briere, G. P. Chen, T. Ferguson, G. Tatishvili, H. Vogel, M. E. Watkins, J. L. Rosner, N. E. Adam, J. P. Alexander, K. Berkelman, D. G. Cassel, V. Crede, J. E. Duboscq, K. M. Ecklund, R. Ehrlich, L. Fields, R. S. Galik, L. Gibbons, B. Gittelman, R. Gray, S. W. Gray, D. L. Hartill, B. K. Heltsley, D. Hertz, L. Hsu, C. D. Jones, J. Kandaswamy, D. L. Kreinick, V. E. Kuznetsov, H. Mahlke-Krüger, T. O. Meyer, P. U. E. Onyisi, J. R. Patterson, D. Peterson, J. Pivarski, D. Riley, A. Ryd, A. J. Sadoff, H. Schwarthoff, M. R. Shepherd, S. Stroiney, W. M. Sun, J. G. Thayer, D. Urner, T. Wilksen, M. Weinberger, S. B. Athar, P. Avery, L. Breva-Newell, R. Patel, V. Potlia, H. Stoeck, J. Yelton, P. Rubin, C. Cawlfield, B. I. Eisenstein, G. D. Gollin, I. Karliner, D. Kim, N. Lowrey, P. Naik, C. Sedlack, M. Selen, J. Williams, J. Wiss, K. W. Edwards, D. Besson, T. K. Pedlar, D. Cronin-Hennessy, K. Y. Gao, D. T. Gong, Y. Kubota, T. Klein, B. W. Lang, S. Z. Li, R. Poling, A. W. Scott, A. Smith, C. J. Stepaniak, S. Dobbs, Z. Metreveli, K. K. Seth, A. Tomaradze, P. Zweber, J. Ernst, A. H. Mahmood, K. Arms, K. K. Gan and H. Severini, "Search for $\eta(1475) \to K^0_S K^{\pm}\pi^{\mp}$ in two-photon fusion at the cleo detector at cornell", Phys. Rev. D **71**, 072001, URL `https://link.aps.org/doi/10.1103/PhysRevD.71.072001` (2005).

Albrow, M., M. Amaryan, E. Chudakov, P. Degtyarenko, A. Aliau, C. Fernández-Ramírez, I. Fernando, A. Filippi, J. Goity, H. Haberzettl, B. Jackson, H. Kamano, C. Keith, M. Kohl, I. Larin, W.-H. Liang, V. Magas, M. Mai, D. Manley and B. Zou, "Workshop on physics with neutral kaon beam at jlab (kl2016) mini-proceedings", (2016).

Atkinson, M., T. Axon, D. Barberis, T. Brodbeck, G. Brookes, J. Bunn, P. Bussey, A. Clegg, J. Dainton, M. Davenport, B. Dickinson, B. Diekmann, A. Donnachie, R. Ellison, P. Flower, P. Flynn, W. Galbraith, K. Heinloth, R. Henderson, R. Hughes-Jones, J. Hutton, M. Ibbotson, H. Jakob, M. Jung, M. Kemp, B. Kumar, J. Laberrigue, G. Lafferty, J. Lane, J. Lassalle, J. Levy, V. Liebenau, R. McClatchey, D. Mercer, J. Morris, J. Morris, D. Newton, C. Paterson, G. Patrick, E. Paul, C. Raine, M. Reidenbach, H. Rotscheidt, A. Schlösser, P. Sharp, I. Skillicorn, K. Smith, K. Storr, R. Thompson, C. De La Vaissière, A. Waite, M. Worsell and T. Yiou, "A spin-parity analysis of the 0 enhancement photoproduced in the energy range 20 to 70 gev", Nuclear Physics B **243**, 1, 1–28, URL `https://www.sciencedirect.com/science/article/pii/0550321384903821` (1984).

Bai, Z. *et al.*, "Partial wave analysis of J / psi —> gamma K0(s) K+- pi-+", Phys. Rev. Lett. **65**, 2507–2510 (1990).

Barbosa, F., G. Biallas, E. Chudakov, C. Cuevas, H. Egiyan, M. Ito, D. Lawrence, L. Pentchev, Y. Qiang, E. Smith, A. Somov, S. Taylor, T. Whitlatch, E. Wolin, G. Young, B. Zihlmann, and C. Zorn, "Hall d/gluex technical design report", (2014).

Barbosa, F., C. Hutton, A. Sitnikov, A. Somov, S. Somov and I. Tolstukhin, "Pair spectrometer hodoscope for hall d at jefferson lab", Nuclear Instruments and Methods in Physics Research Section A: Accelerators, Spectrometers, Detectors and Associated Equipment **795**, 376–380, URL https://www.sciencedirect.com/science/article/pii/S0168900215007573 (2015).

Beattie, T., A. Foda, C. Henschel, S. Katsaganis, S. Krueger, G. Lolos, Z. Papandreou, E. Plummer, I. Semenova, A. Semenov, F. Barbosa, E. Chudakov, M. Dalton, D. Lawrence, Y. Qiang, N. Sandoval, E. Smith, C. Stanislav, J. Stevens, S. Taylor, T. Whitlatch, B. Zihlmann, W. Levine, W. McGinley, C. Meyer, M. Staib, E. Anassontzis, C. Kourkoumelis, G. Vasileiadis, G. Voulgaris, W. Brooks, H. Hakobyan, S. Kuleshov, R. Rojas, C. Romero, O. Soto, A. Toro, I. Vega and M. Shepherd, "Construction and performance of the barrel electromagnetic calorimeter for the gluex experiment", Nuclear Instruments and Methods in Physics Research Section A: Accelerators, Spectrometers, Detectors and Associated Equipment **896**, 24–42, URL https://www.sciencedirect.com/science/article/pii/S0168900218304807 (2018).

Bertin, A. *et al.*, "E / iota decays to K anti-K pi in anti-p p annihilation at rest", Phys. Lett. B **361**, 187–198 (1995).

Denisov, S., A. Dzierba, R. Heinz, A. Klimenko, I. Polezhaeva, V. Samoylenko, E. Scott, A. Shchukin, P. Smith, C. Steffen, S. Teige and S. Volodina, "Characteristics of the tof counters for gluex experiment", Nuclear Instruments and Methods in Physics Research Section A: Accelerators, Spectrometers, Detectors and Associated Equipment **494**, 1, 495–499, URL https://www.sciencedirect.com/science/article/pii/S0168900202015383, proceedings of the 8th International Conference on Instrumentatio n for Colliding Beam Physics (2002).

Dudek, J. J., R. G. Edwards, P. Guo and C. E. Thomas, "Toward the excited isoscalar meson spectrum from lattice qcd", Physical Review D **88**, 9, URL http://dx.doi.org/10.1103/PhysRevD.88.094505 (2013).

Dugger, M., B. Ritchie, N. Sparks, K. Moriya, R. Tucker, R. Lee, B. Thorpe, T. Hodges, F. Barbosa, N. Sandoval and R. Jones, "Design and construction of a high-energy photon polarimeter", Nuclear Instruments and Methods in Physics Research Section A: Accelerators, Spectrometers, Detectors and Associated Equipment **867**, 115–127, URL https://www.sciencedirect.com/science/article/pii/S0168900217305715 (2017).

Freyberger, A., "Commissioning and Operation of 12 GeV CEBAF", in "6th International Particle Accelerator Conference", (2015).

Griffiths, D., *Introduction to elementary particles* (Wiley-VCH, 2010), 2nd edn.

Group, P. D., P. A. Zyla, R. M. Barnett, J. Beringer, O. Dahl, D. A. Dwyer, D. E. Groom, C. J. Lin, K. S. Lugovsky, E. Pianori, D. J. Robinson, C. G. Wohl, W. M. Yao, K. Agashe, G. Aielli, B. C. Allanach, C. Amsler, M. Antonelli, E. C. Aschenauer, D. M. Asner, H. Baer, S. Banerjee, L. Baudis, C. W. Bauer, J. J.

Beatty, V. I. Belousov, S. Bethke, A. Bettini, O. Biebel, K. M. Black, E. Blucher, O. Buchmuller, V. Burkert, M. A. Bychkov, R. N. Cahn, M. Carena, A. Ceccucci, A. Cerri, D. Chakraborty, R. S. Chivukula, G. Cowan, G. D'Ambrosio, T. Damour, D. de Florian, A. de Gouvêa, T. DeGrand, P. de Jong, G. Dissertori, B. A. Dobrescu, M. D'Onofrio, M. Doser, M. Drees, H. K. Dreiner, P. Eerola, U. Egede, S. Eidelman, J. Ellis, J. Erler, V. V. Ezhela, W. Fetscher, B. D. Fields, B. Foster, A. Freitas, H. Gallagher, L. Garren, H. J. Gerber, G. Gerbier, T. Gershon, Y. Gershtein, T. Gherghetta, A. A. Godizov, M. C. Gonzalez-Garcia, M. Goodman, C. Grab, A. V. Gritsan, C. Grojean, M. Grünewald, A. Gurtu, T. Gutsche, H. E. Haber, C. Hanhart, S. Hashimoto, Y. Hayato, A. Hebecker, S. Heinemeyer, B. Heltsley, J. J. Hernández-Rey, K. Hikasa, J. Hisano, A. Höcker, J. Holder, A. Holtkamp, J. Huston, T. Hyodo, K. F. Johnson, M. Kado, M. Karliner, U. F. Katz, M. Kenzie, V. A. Khoze, S. R. Klein, E. Klempt, R. V. Kowalewski, F. Krauss, M. Kreps, B. Krusche, Y. Kwon, O. Lahav, J. Laiho, L. P. Lellouch, J. Lesgourgues, A. R. Liddle, Z. Ligeti, C. Lippmann, T. M. Liss, L. Littenberg, C. Lourengo, S. B. Lugovsky, A. Lusiani, Y. Makida, F. Maltoni, T. Mannel, A. V. Manohar, W. J. Marciano, A. Masoni, J. Matthews, U. G. Meißner, M. Mikhasenko, D. J. Miller, D. Milstead, R. E. Mitchell, K. Mönig, P. Molaro, F. Moortgat, M. Moskovic, K. Nakamura, M. Narain, P. Nason, S. Navas, M. Neubert, P. Nevski, Y. Nir, K. A. Olive, C. Patrignani, J. A. Peacock, S. T. Petcov, V. A. Petrov, A. Pich, A. Piepke, A. Pomarol, S. Profumo, A. Quadt, K. Rabbertz, J. Rademacker, G. Raffelt, H. Ramani, M. Ramsey-Musolf, B. N. Ratcliff, P. Richardson, A. Ringwald, S. Roesler, S. Rolli, A. Romaniouk, L. J. Rosenberg, J. L. Rosner, G. Rybka, M. Ryskin, R. A. Ryutin, Y. Sakai, G. P. Salam, S. Sarkar, F. Sauli, O. Schneider, K. Scholberg, A. J. Schwartz, J. Schwiening, D. Scott, V. Sharma, S. R. Sharpe, T. Shutt, M. Silari, T. Sjöstrand, P. Skands, T. Skwarnicki, G. F. Smoot, A. Soffer, M. S. Sozzi, S. Spanier, C. Spiering, A. Stahl, S. L. Stone, Y. Sumino, T. Sumiyoshi, M. J. Syphers, F. Takahashi, M. Tanabashi, J. Tanaka, M. Taševský, K. Terashi, J. Terning, U. Thoma, R. S. Thorne, L. Tiator, M. Titov, N. P. Tkachenko, D. R. Tovey, K. Trabelsi, P. Urquijo, G. Valencia, R. Van de Water, N. Varelas, G. Venanzoni, L. Verde, M. G. Vincter, P. Vogel, W. Vogelsang, A. Vogt, V. Vorobyev, S. P. Wakely, W. Walkowiak, C. W. Walter, D. Wands, M. O. Wascko, D. H. Weinberg, E. J. Weinberg, M. White, L. R. Wiencke, S. Willocq, C. L. Woody, R. L. Workman, M. Yokoyama, R. Yoshida, G. Zanderighi, G. P. Zeller, O. V. Zenin, R. Y. Zhu, S. L. Zhu, F. Zimmermann, J. Anderson, T. Basaglia, V. S. Lugovsky, P. Schaffner and W. Zheng, "Review of Particle Physics", Progress of Theoretical and Experimental Physics **2020**, 8, URL `https://doi.org/10.1093/ptep/ptaa104`, 083C01 (2020).

Gutsche, T., V. E. Lyubovitskij and M. C. Tichy, "Strong decays of radially excited mesons in a chiral approach", Physical Review D **79**, 1, URL `http://dx.doi.org/10.1103/PhysRevD.79.014036` (2009).

Jarvis, N., C. Meyer, B. Zihlmann, M. Staib, A. Austregesilo, F. Barbosa, C. Dickover, V. Razmyslovich, S. Taylor, Y. Van Haarlem and et al., "The central drift chamber for gluex", Nuclear Instruments and Methods in Physics Research Section A: Accelerators, Spectrometers, Detectors and Associated Equipment **962**, 163727, URL `http://dx.doi.org/10.1016/j.nima.2020.163727` (2020).

Klempt, E. and A. Zaitsev, "Glueballs, hybrids, multiquarks", Physics Reports **454**, 1-4, 1–202, URL http://dx.doi.org/10.1016/j.physrep.2007.07.006 (2007).

Leemann, C. W., D. R. Douglas and G. A. Krafft, "The continuous electron beam accelerator facility: Cebaf at the jefferson laboratory", Annual Review of Nuclear and Particle Science **51**, 1, 413–450, URL https://doi.org/10.1146/annurev.nucl.51.101701.132327 (2001).

Mathieu, V., M. Albaladejo, C. Fernández-Ramírez, A. Jackura, M. Mikhasenko, A. Pilloni and A. Szczepaniak, "Moments of angular distribution and beam asymmetries in 0 photoproduction at gluex", Physical Review D **100**, 5, URL http://dx.doi.org/10.1103/PhysRevD.100.054017 (2019).

Mathieu, V., N. Kochelev and V. Vento, "The Physics of Glueballs", Int. J. Mod. Phys. E **18**, 1–49 (2009).

Meyer, C. and E. Swanson, "Hybrid mesons", Progress in Particle and Nuclear Physics **82**, 21–58, URL http://dx.doi.org/10.1016/j.ppnp.2015.03.001 (2015).

Meyer, C. A. and Y. Van Haarlem, "Status of exotic-quantum-number mesons", Physical Review C **82**, 2, URL http://dx.doi.org/10.1103/PhysRevC.82.025208 (2010).

Pentchev, L., F. Barbosa, V. Berdnikov, D. Butler, S. Furletov, L. Robison and B. Zihlmann, "Studies with cathode drift chambers for the gluex experiment at jefferson lab", Nuclear Instruments and Methods in Physics Research Section A: Accelerators, Spectrometers, Detectors and Associated Equipment **845**, 281–284, URL https://www.sciencedirect.com/science/article/pii/S0168900216302893, proceedings of the Vienna Conference on Instrumentation 2016 (2017).

Pooser, E., F. Barbosa, W. Boeglin, C. Hutton, M. Ito, M. Kamel, P. Khetarpal, A. LLodra, N. Sandoval, S. Taylor and et al., "The gluex start counter detector", Nuclear Instruments and Methods in Physics Research Section A: Accelerators, Spectrometers, Detectors and Associated Equipment **927**, 330–342, URL http://dx.doi.org/10.1016/j.nima.2019.02.029 (2019).

Reece, C. E., "Continuous wave superconducting radio frequency electron linac for nuclear physics research", Physical Review Accelerators and Beams **19**, 12, URL http://dx.doi.org/10.1103/PhysRevAccelBeams.19.124801 (2016).

Salgado, C. W. and D. P. Weygand, "On the partial-wave analysis of mesonic resonances decaying to multiparticle final states produced by polarized photons", Physics Reports **537**, 1, 1–58, URL http://dx.doi.org/10.1016/j.physrep.2013.11.005 (2014).

Shepherd, M. R., "Amptools implementation of polarized production", GlueX-doc-4094 (2019).

Stevens, J., "Vector-pseudoscalar amplitude in reflectivity basis", (2021).

Thomson, M., *Modern particle physics* (Cambride University Press, 2013).

Van Haarlem, Y., C. Meyer, F. Barbosa, B. Dey, D. Lawrence, V. Razmyslovich, E. Smith, G. Visser, T. Whitlatch, G. Wilkin and B. Zihlmann, "The gluex central drift chamber: Design and performance", Nuclear Instruments and Methods in Physics Research Section A: Accelerators, Spectrometers, Detectors and Associated Equipment **622**, 1, 142–156, URL `https://www.sciencedirect.com/science/article/pii/S0168900210014622` (2010).

Vorobiev, I., "Study of resonance formation in the mass region 1400 – 1500 mev through the reaction ks0k", AIP Conference Proceedings **892**, 1, 531–532, URL `https://aip.scitation.org/doi/abs/10.1063/1.2714470` (2007).

APPENDIX A

PWA WAVES

J	M	L	m_L	S	m_S
0	0	1	-1	1	1
0	0	1	0	1	0
0	0	1	1	1	-1
1	-1	0	0	1	-1
1	0	0	0	1	0
1	1	0	0	1	1
2	-2	2	-2	1	0
2	-2	2	-1	1	-1
2	-1	2	-2	1	1
2	-1	2	-1	1	0
2	-1	2	0	1	-1
2	0	2	-1	1	1
2	0	2	0	1	0
2	0	2	1	1	-1
2	1	2	0	1	1
2	1	2	1	1	0
2	1	2	2	1	-1
2	2	2	1	1	1
2	2	2	2	1	0

Table A.1: The set of waves used in the partial wave analysis meeting the criteria outlined in Section 4.0.3.

APPENDIX B

ANGULAR DISTRIBUTION FITS

B.1 $\cos\theta$ fit

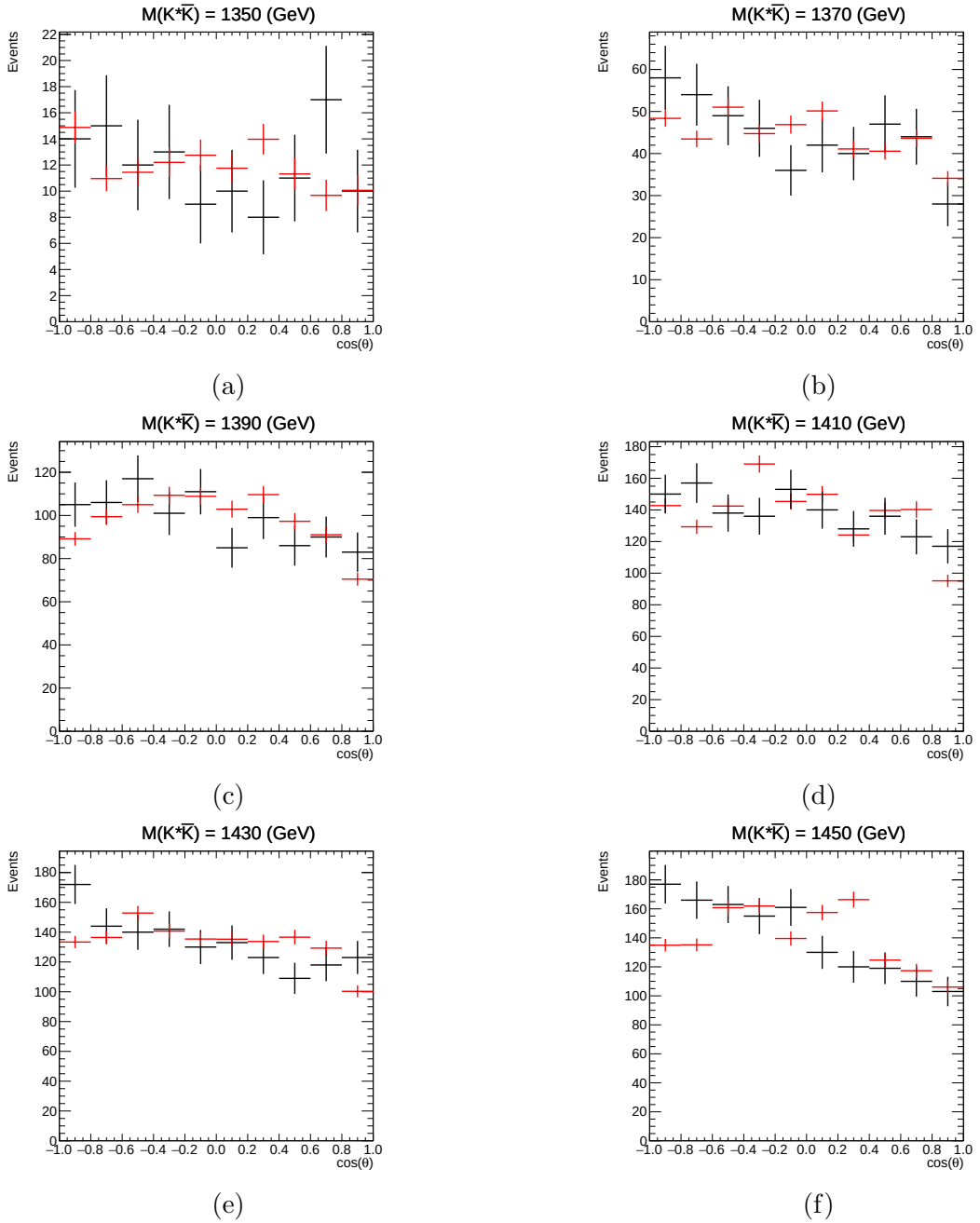

(a) (b) (c) (d) (e) (f)

Figure B.1: PWA fits to $\cos\theta$ distributions for mass bins (a) 1350 MeV, (b) 1370 MeV, (c) 1390 MeV, (d) 1410 MeV, (e) 1430 MeV, and (f) 1450 MeV.

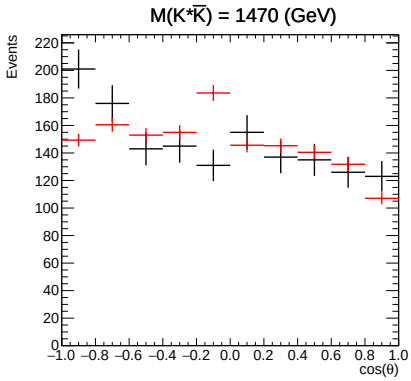

(a)

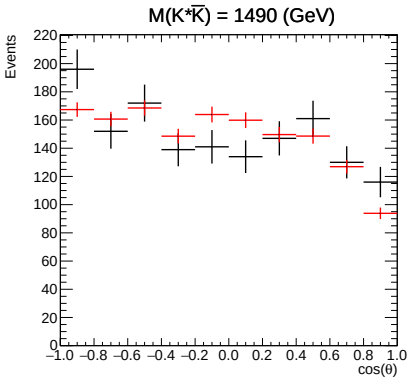

(b)

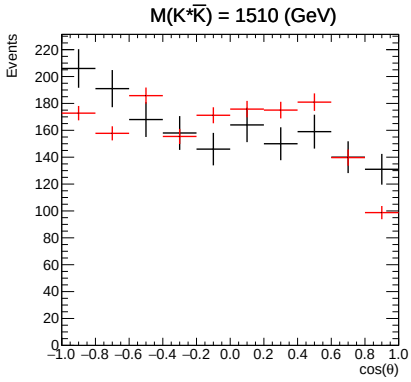

(c)

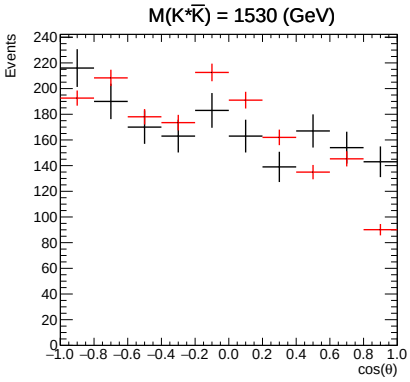

(d)

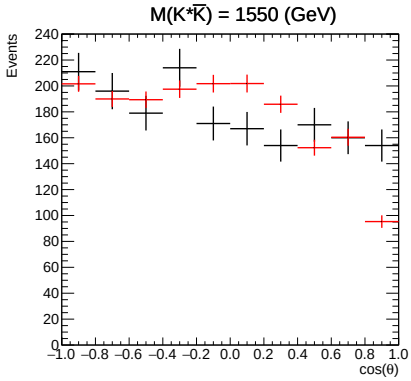

(e)

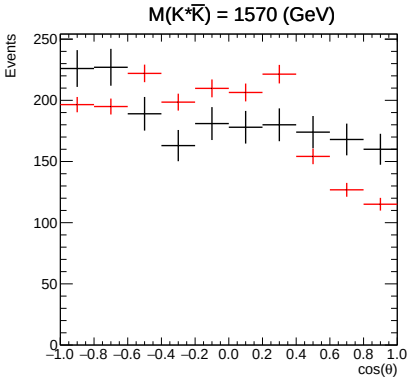

(f)

Figure B.2: PWA fits to $\cos\theta$ distributions for mass bins (a) 1470 MeV, (b) 1490 MeV, (c) 1510 MeV, (d) 1530 MeV, (e) 1550 MeV, and (f) 1570 MeV.

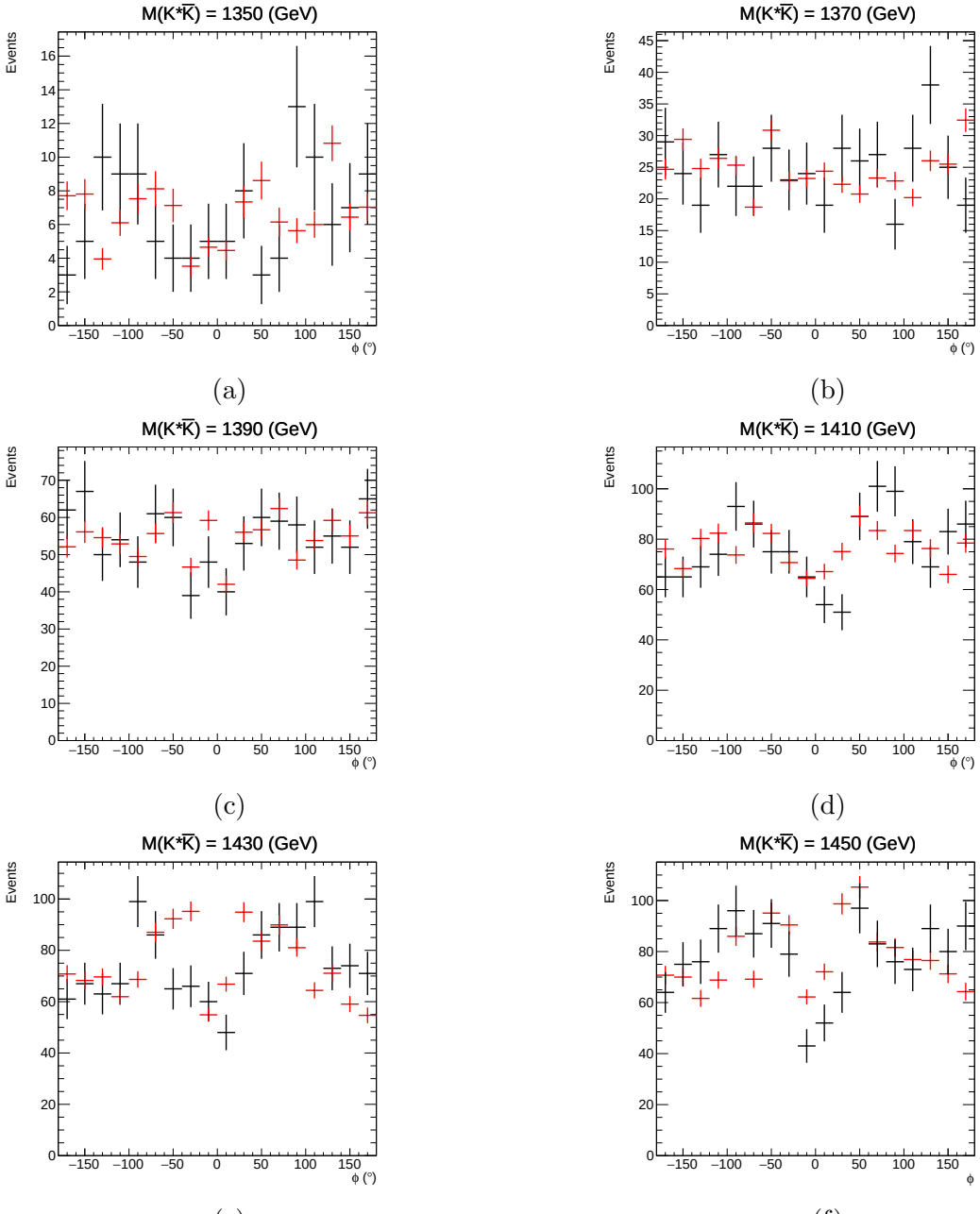

Figure B.3: PWA fits to ϕ distributions for mass bins (a) 1350 MeV, (b) 1370 MeV, (c) 1390 MeV, (d) 1410 MeV, (e) 1430 MeV, and (f) 1450 MeV.

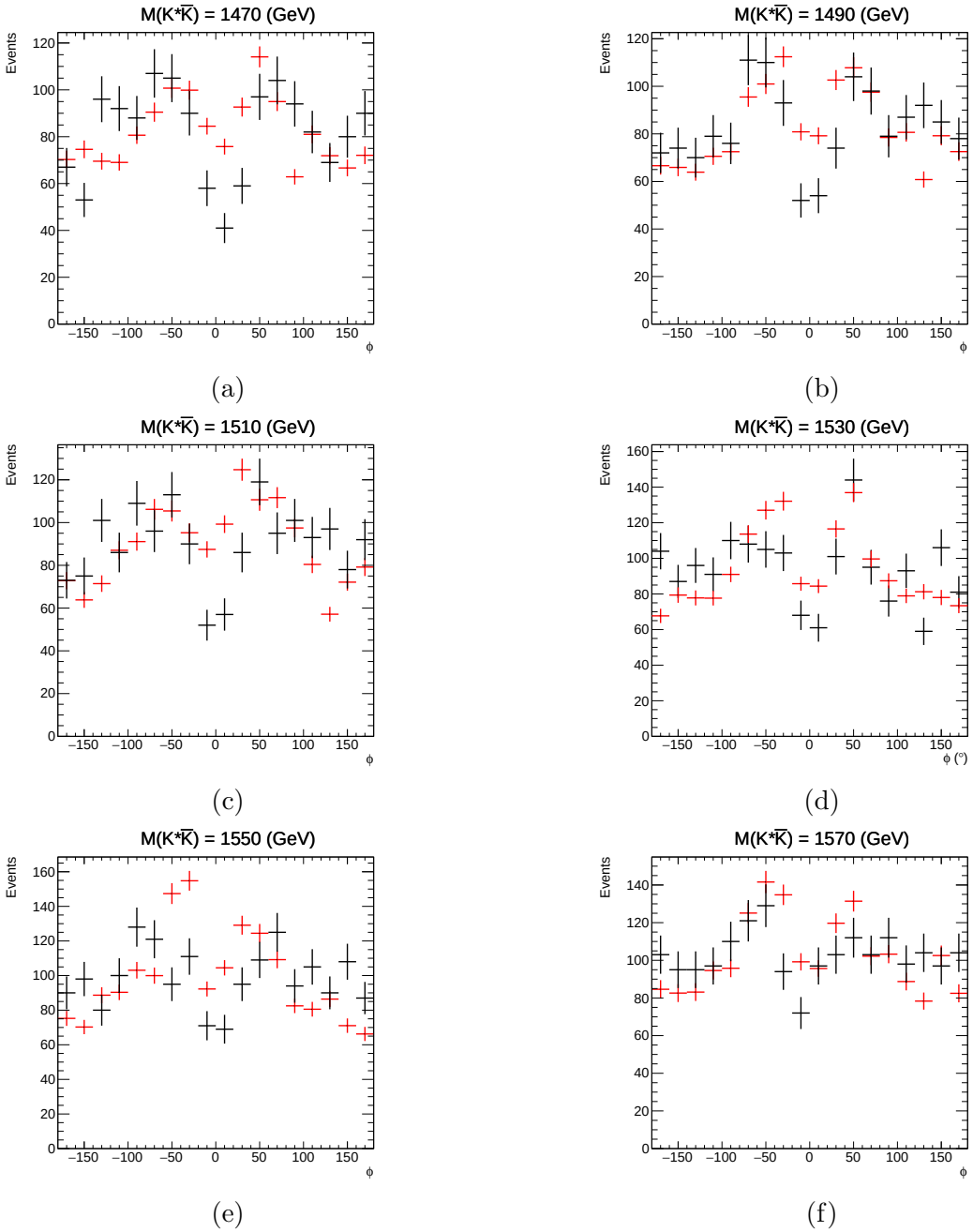

(a) (b) (c) (d) (e) (f)

Figure B.4: PWA fits to ϕ distributions for mass bins (a) 1470 MeV, (b) 1490 MeV, (c) 1510 MeV, (d) 1530 MeV, (e) 1550 MeV, and (f) 1570 MeV.

B.3 $\cos\theta_H$ fit

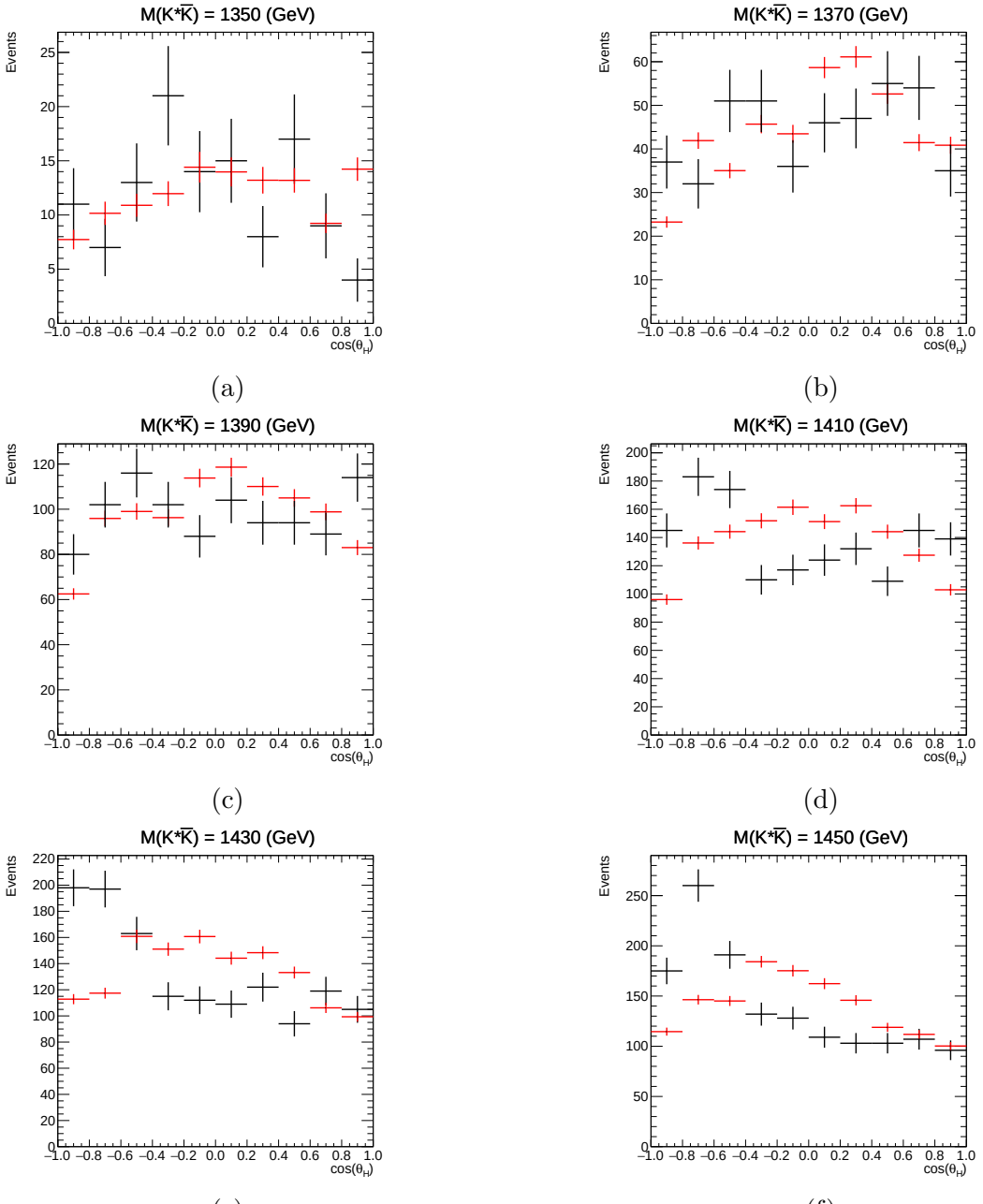

(a) (b) (c) (d) (e) (f)

Figure B.5: PWA fits to $\cos\theta_H$ distributions for mass bins (a) 1350 MeV, (b) 1370 MeV, (c) 1390 MeV, (d) 1410 MeV, (e) 1430 MeV, and (f) 1450 MeV.

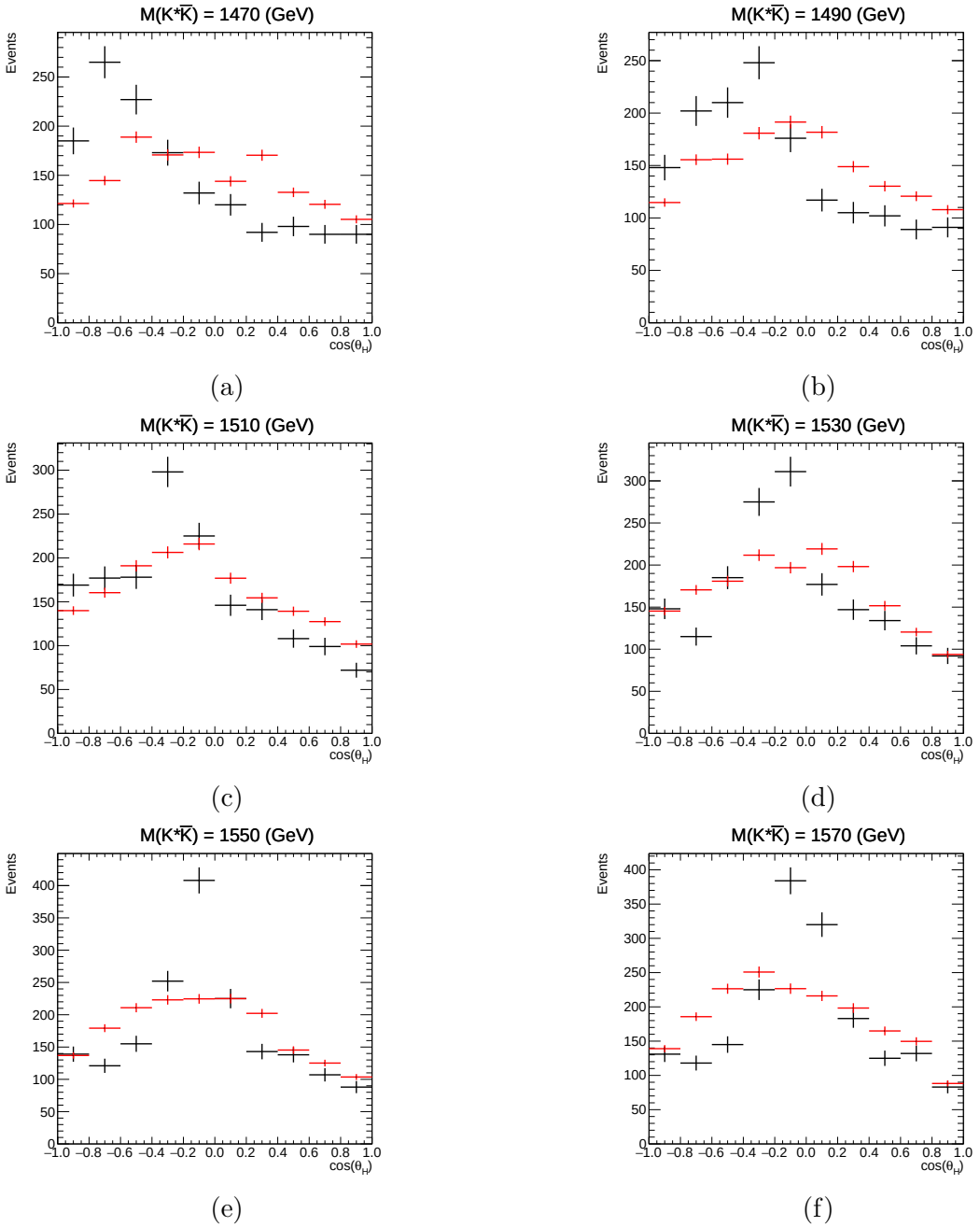

(a) (b) (c) (d) (e) (f)

Figure B.6: PWA fits to $\cos\theta_H$ distributions for mass bins (a) 1470 MeV, (b) 1490 MeV, (c) 1510 MeV, (d) 1530 MeV, (e) 1550 MeV, and (f) 1570 MeV.

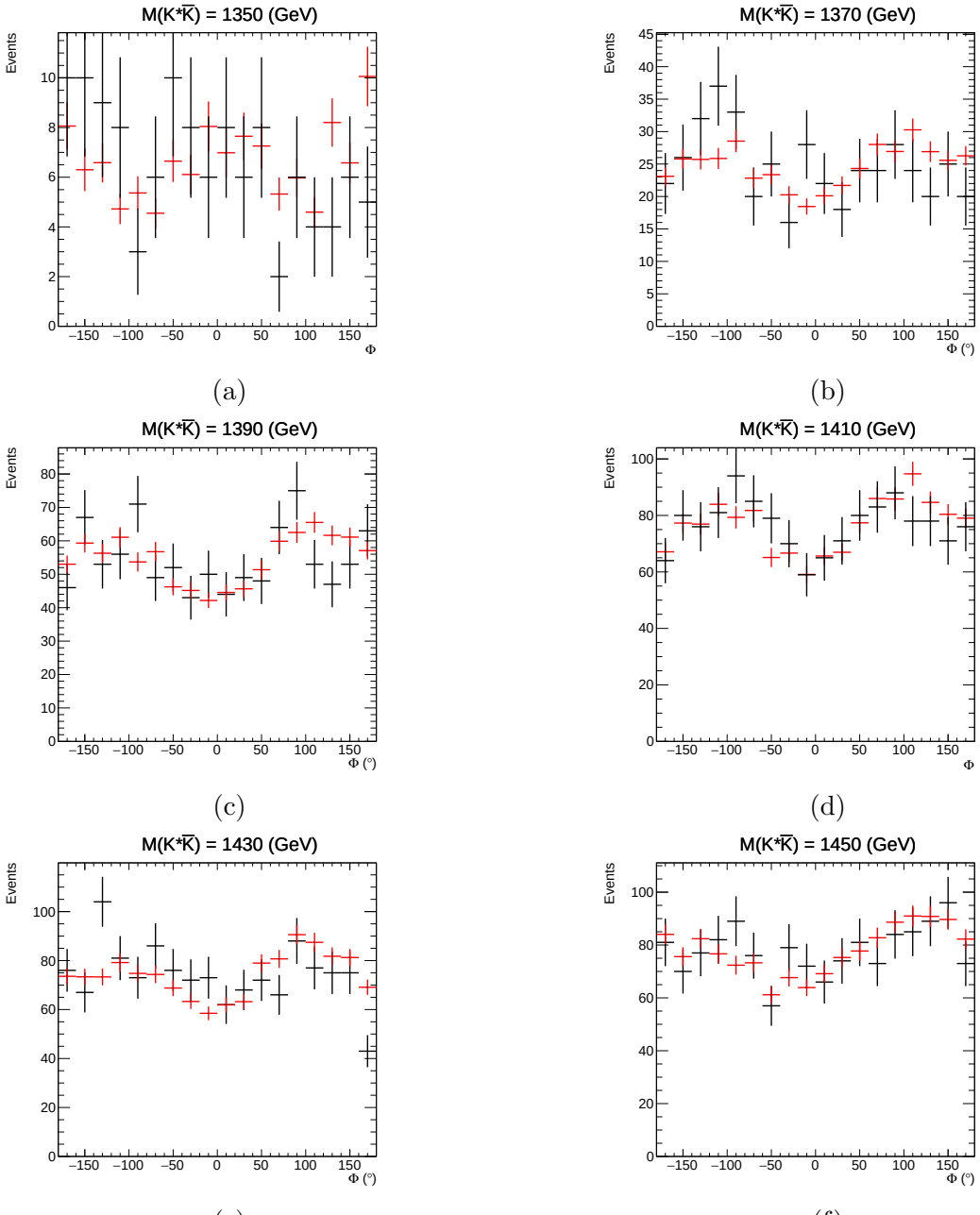

Figure B.7: PWA fits to Φ distributions for mass bins (a) 1350 MeV, (b) 1370 MeV, (c) 1390 MeV, (d) 1410 MeV, (e) 1430 MeV, and (f) 1450 MeV.

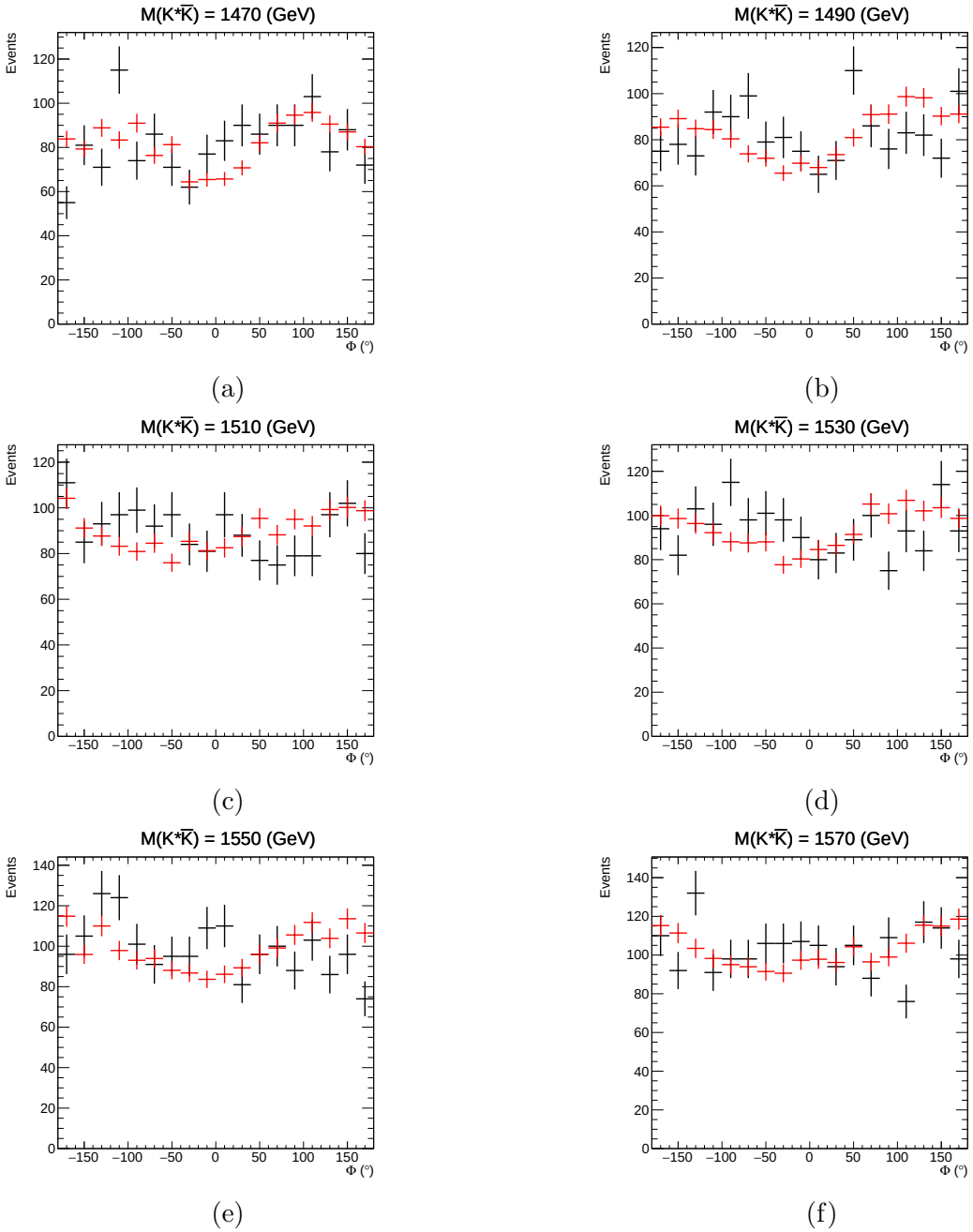

(a) (b) (c) (d) (e) (f)

Figure B.8: PWA fits to Φ distributions for mass bins -(a) 1470 MeV, (b) 1490 MeV, (c) 1510 MeV, (d) 1530 MeV, (e) 1550 MeV, and (f) 1570 MeV.

APPENDIX C

ERROR DETERMINATION FITS

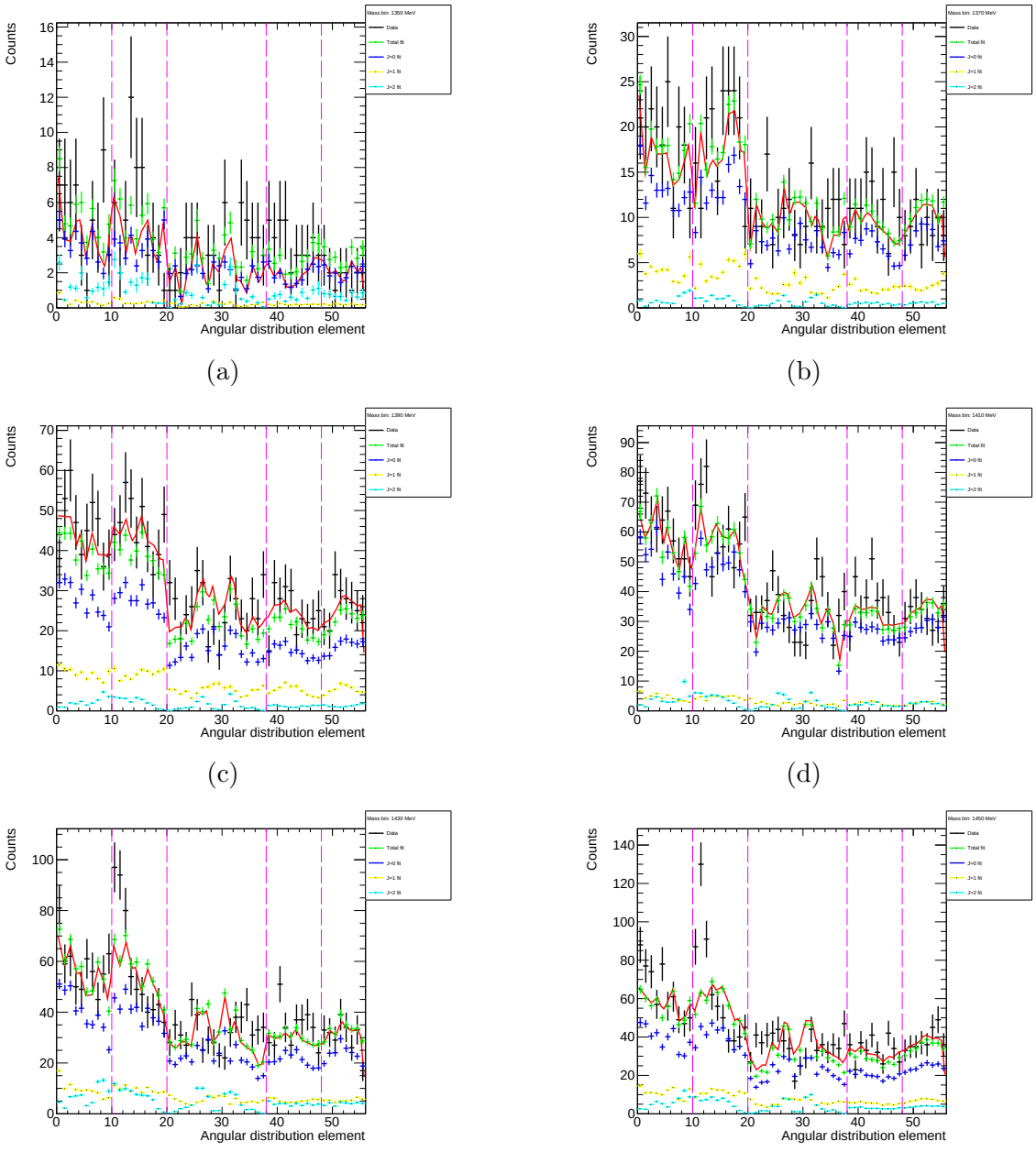

(a) (b) (c) (d) (e) (f)

Figure C.1: Uncertainty determination fits as described in Section 4.0.4 for mass bins (a) 1350 MeV, (b) 1370 MeV, (c) 1390 MeV, (d) 1410 MeV, (e) 1430 MeV, and (f) 1450 MeV.

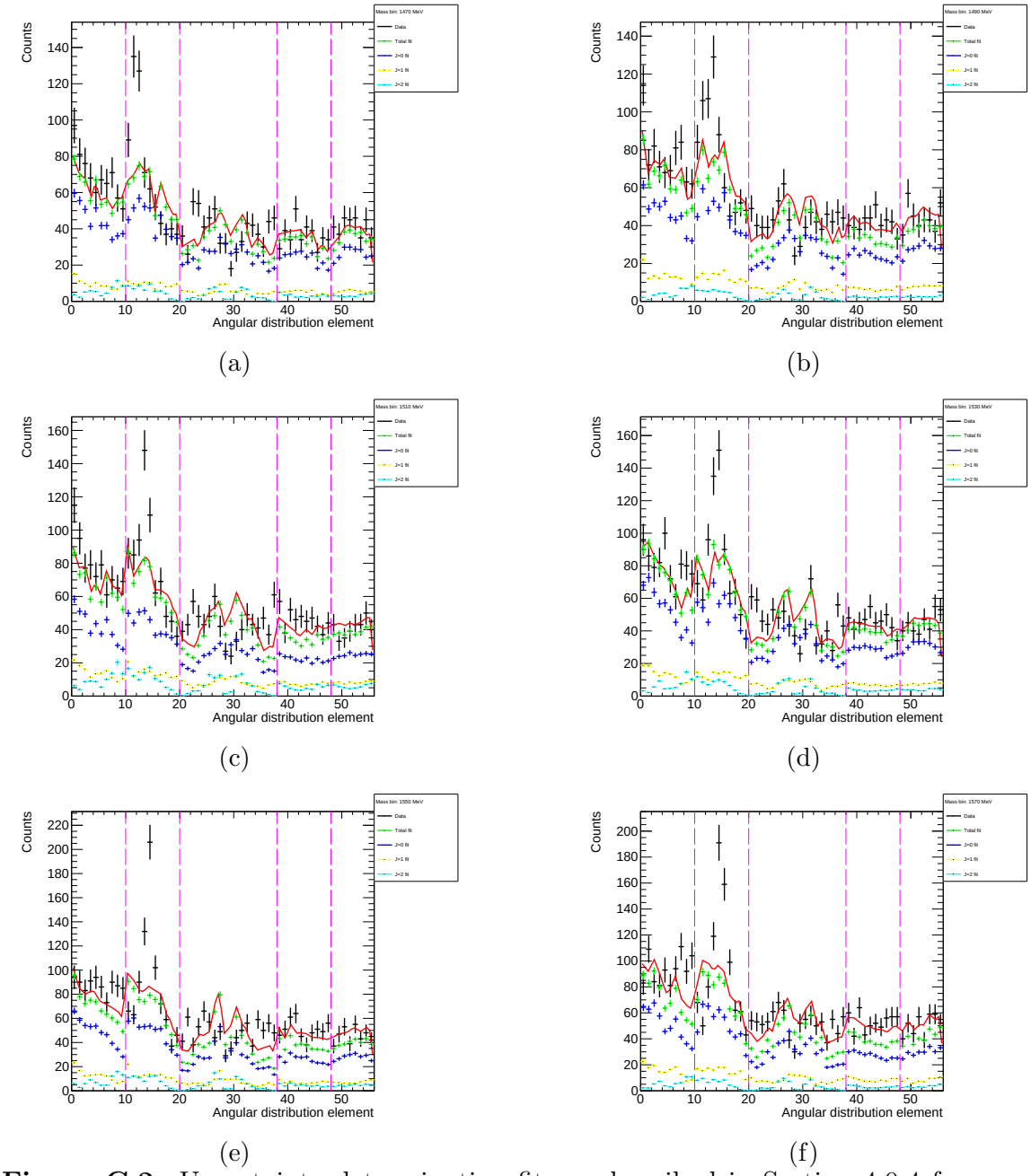

(a) (b) (c) (d) (e) (f)

Figure C.2: Uncertainty determination fits as described in Section 4.0.4 for mass bins (a) 1470 MeV, (b) 1490 MeV, (c) 1510 MeV, (d) 1530 MeV, (e) 1550 MeV, and (f) 1570 MeV.

APPENDIX D

PWA INVARIANT MASS DISTRIBUTIONS

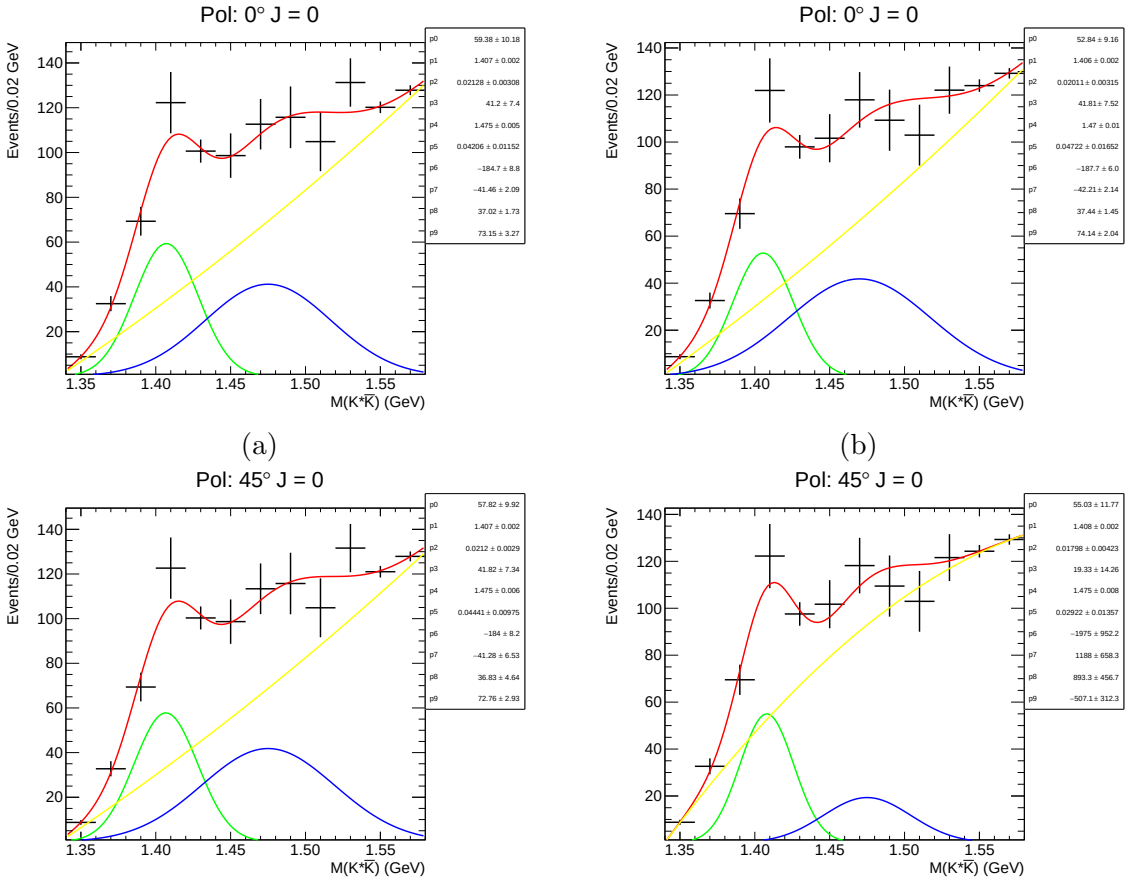

Figure D.1: $J = 0$ invariant mass distributions of (a) $K^{*+}K^{-}$ and (b) $K^{*-}K^{+}$ for 0° polarization and (c) $K^{*+}K^{-}$ and (d) $K^{*-}K^{+}$ 45° polarization.

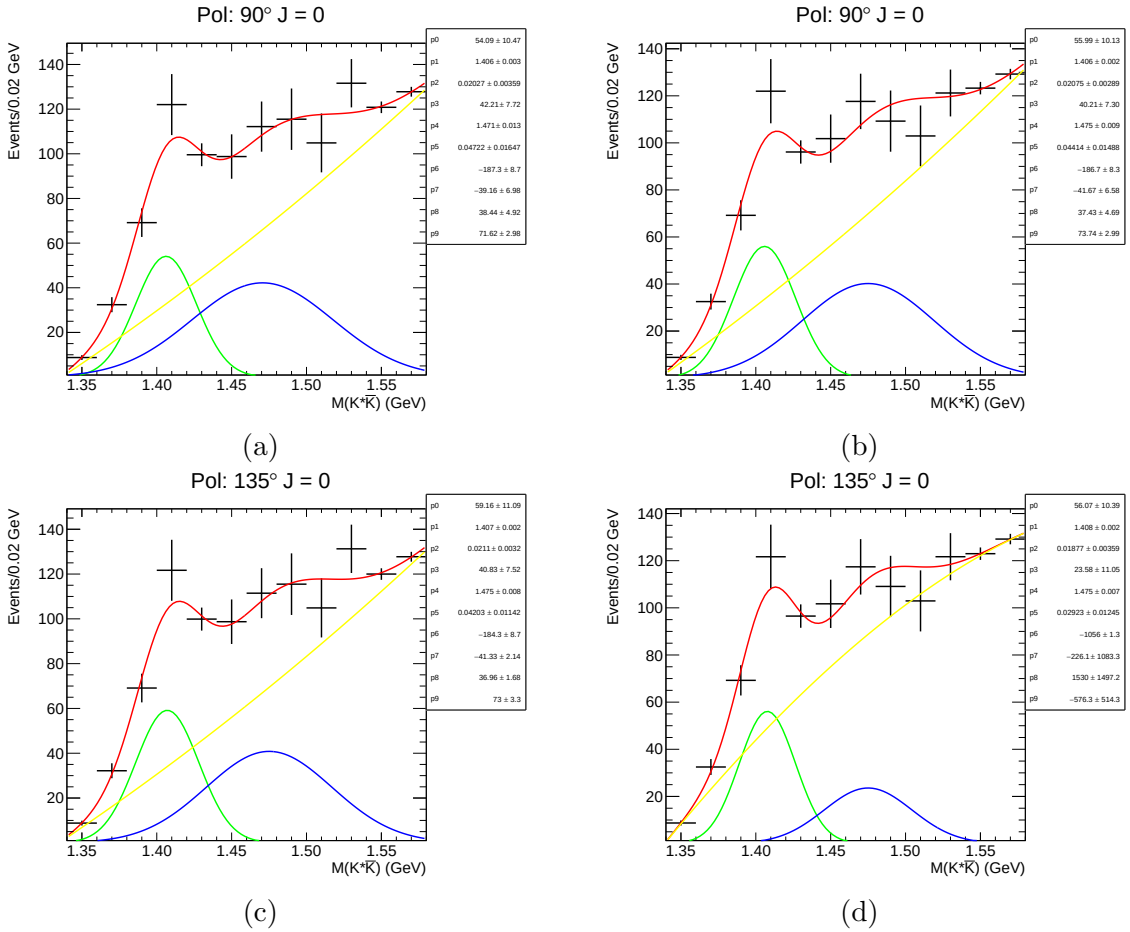

Figure D.2: $J = 0$ invariant mass distributions of (a) $K^{*+}K^-$ and (b) $K^{*-}K^+$ for 90° polarization and (c) $K^{*+}K^-$ and (d) $K^{*-}K^+$ 135° polarization.

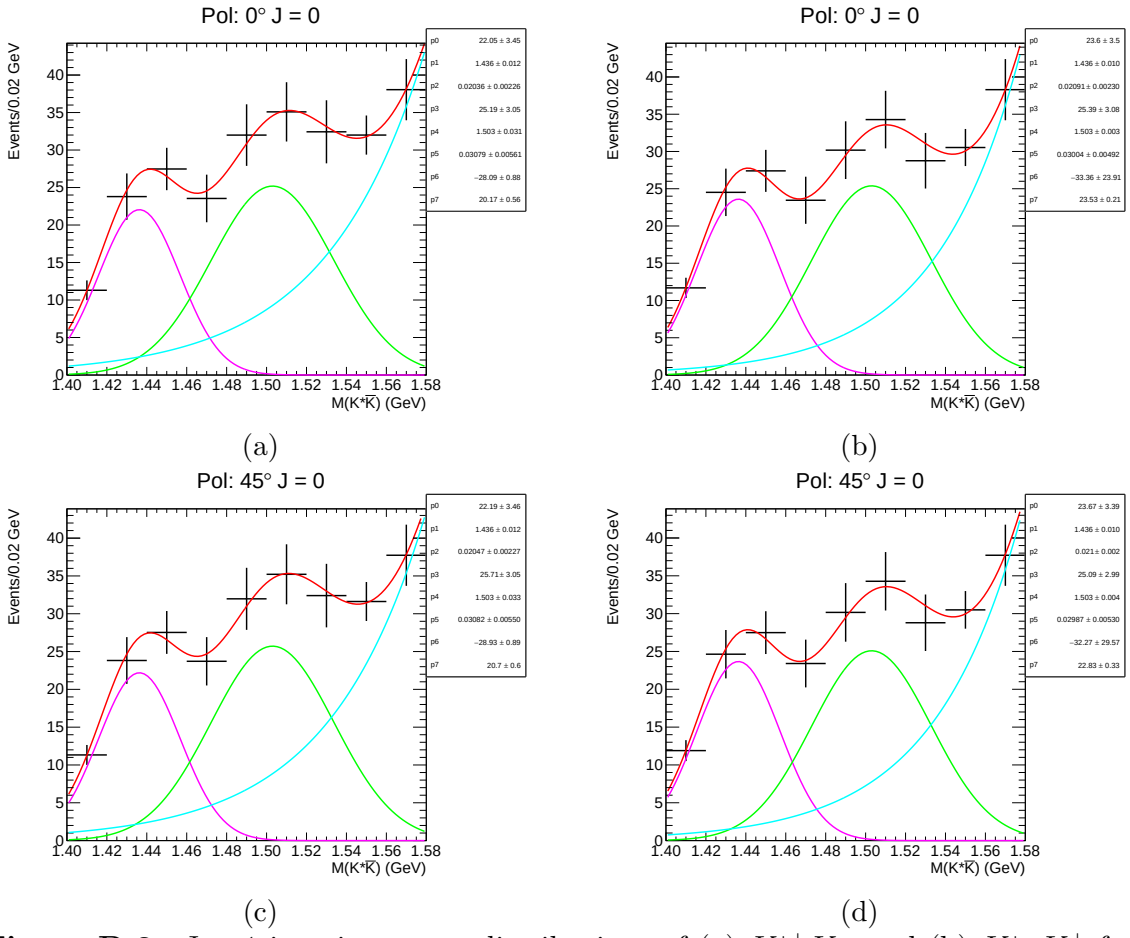

Figure D.3: $J = 1$ invariant mass distributions of (a) $K^{*+}K^-$ and (b) $K^{*-}K^+$ for $0°$ polarization and (c) $K^{*+}K^-$ and (d) $K^{*-}K^+$ $45°$ polarization.

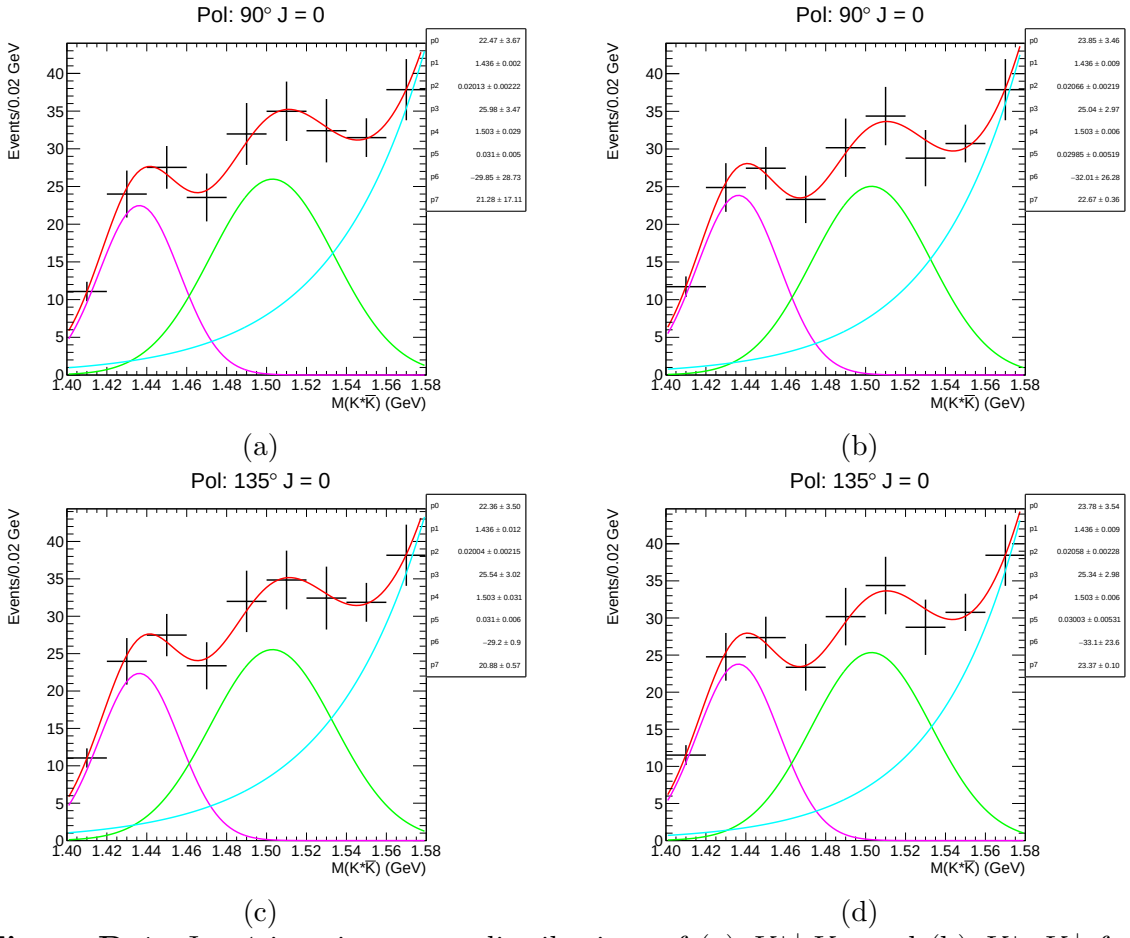

Figure D.4: $J = 1$ invariant mass distributions of (a) $K^{*+}K^-$ and (b) $K^{*-}K^+$ for 90° polarization and (c) $K^{*+}K^-$ and (d) $K^{*-}K^+$ 135° polarization.

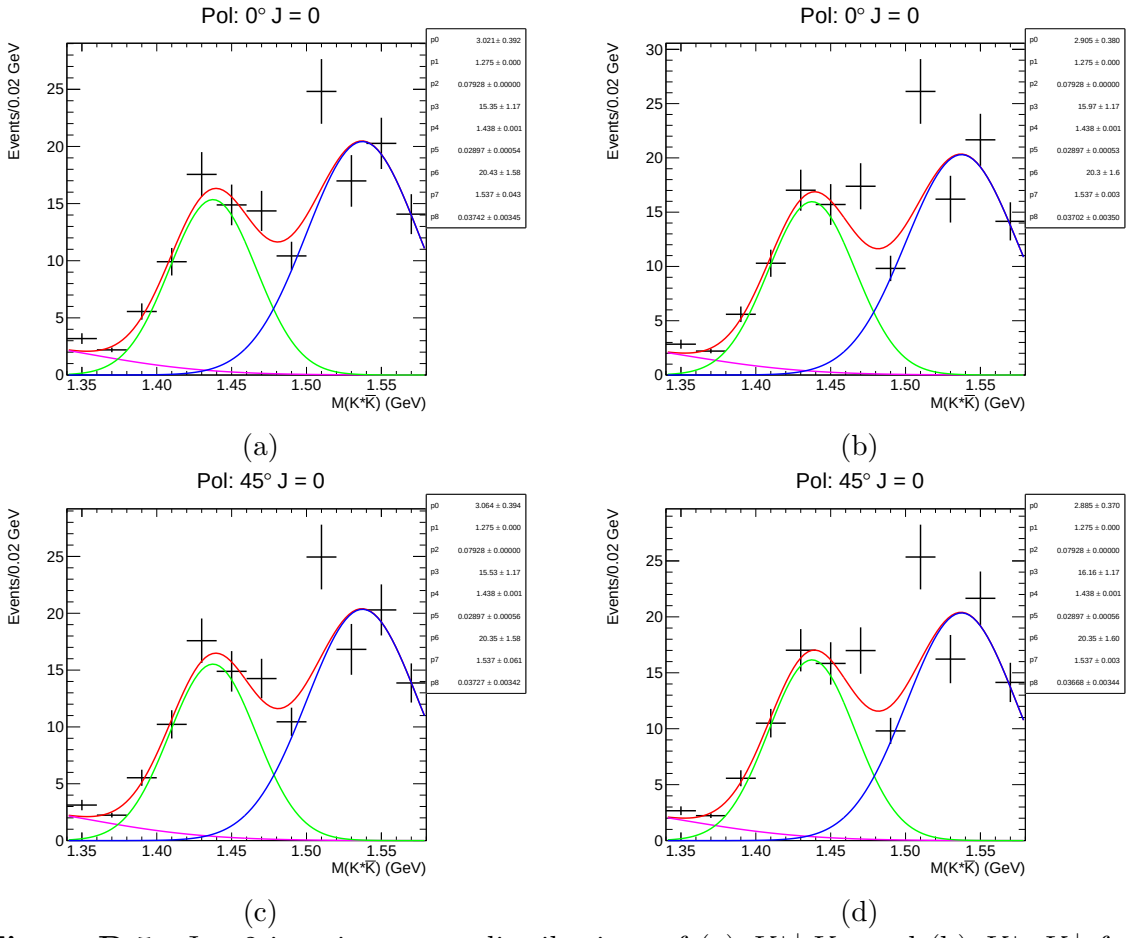

Figure D.5: $J = 2$ invariant mass distributions of (a) $K^{*+}K^-$ and (b) $K^{*-}K^+$ for $0°$ polarization and (c) $K^{*+}K^-$ and (d) $K^{*-}K^+$ $45°$ polarization.

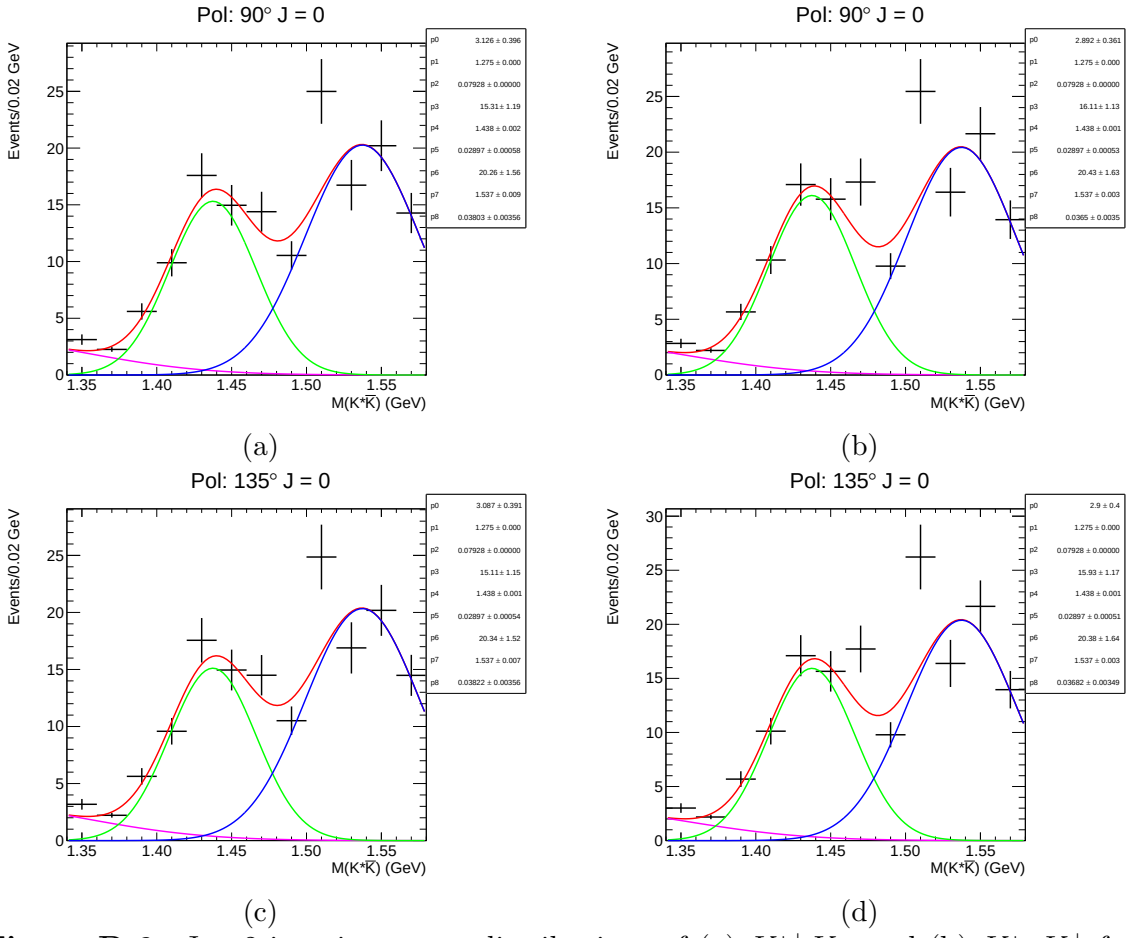

Figure D.6: $J = 2$ invariant mass distributions of (a) $K^{*+}K^-$ and (b) $K^{*-}K^+$ for 90° polarization and (c) $K^{*+}K^-$ and (d) $K^{*-}K^+$ 135° polarization.

Curriculum Vita
Sebastian Cole

(Prepared: November 12, 2020)

Email: sebastian.cole@asu.edu
Phone: (602) 318-2603

Education

- Brophy College Preparatory: Graduated Spring 2008
- Arizona State University Bachelor of Science Physics: Graduated *cum laude* Spring 2015
- Arizona State University Physics Graduate Program: Expected Graduation Spring 2021

Research

- Biophysics ASU: Daniel Martin (Ph.D.) Individual Instruction Summer/Fall 2012
  - CLAS Funded Research Summer 2014
- Arizona State University's Meson Physics Group: Summer 2015 - Present
- Jefferson Lab's GlueX collaboration: Summer 2015 - Present
  - Research Assistant: Fall 2017 - Present

Grants and Awards

- Bold Leader Award: Awarded to top Cadet of Company at LTC July 12, 2010
- Wally Stoezl Scholarship: Awarded April 30, 2014
- CLAS Funding: Awarded May, 2014
- Wally Stoezl Scholarship: Awarded April 18, 2017
- CLAS Student Leader: Awarded November 2, 2018
- CLAS Student Leader: Awarded November 20, 2020
- CISA Outstanding Graduate Student: Awarded December 2, 2020

Professional Development

- Army ROTC: Fall 2009 - Fall 2010
- Leadership Training Course (LTC): Summer 2010
- Matlab: 12 years
- Unix shell (Bash): 11 years
- C++: 10 years

- Python: 9.5 years
- GlueX software: 5.5 years
- CERN's ROOT: 5.5 years
- Research at Jefferson Lab with GlueX collaboration Newport News, VA: Fall 2017 - Fall 2018

Teaching experience

- ASU Physics 132 Lab: Fall 2011 (two sections)
- ASU Physical Science 110 Lab: Fall 2011
- ASU Physical Science 110 Lab: Spring 2012
- ASU Physics 111 Recitation: Spring 2012
- ASU Physics 121 Recitation: Summer 2012
- ASU Physics 113 Lab: Summer 2012
- ASU Physics 150: Fall 2013
- ASU Physics 122 Lab: Spring 2013
- ASU Physics 131 Recitation: Spring 2013
- ASU Physics 132 Lab: Spring 2013
- ASU Physics 121 Recitation: Fall 2013 (three sections)
- ASU Physics 131 Recitation: Fall 2013
- ASU Physics 113 Lab: Spring 2014 (three sections)
- ASU Physics 121 Recitation: Summer 2014
- ASU Physics 112 Recitation: Summer 2014
- ASU Physics 121 Recitation: Fall 2014 (two sections)
- ASU Physics 131 Recitation: Fall 2014 (three sections)
- ASU Physics 121 Recitation: Spring 2015 (five sections)
- ASU Physics 121 Recitation: Fall 2015 (five sections)
- ASU Physics 121 Recitation: Spring 2016 (three sections)
- ASU Physics 112 Recitation: Fall 2016 (two sections)
- ASU Physics 121 Recitation: Fall 2016 (two sections)
- ASU Physics 121 Recitation: Spring 2017 (four sections)
- ASU Physics 121 Recitation: Summer 2017
- ASU Physics 132 Lab: Summer 2017
- ASU Physics 310: Fall 2018 (in class section)
- ASU Physics 311: Fall 2018 (hybrid section)
- ASU Physics 311: Spring 2019 (in class and hybrid sections)

- ASU Physics 113 Lab: Summer 2019 (online)
- ASU Physics 150: Fall 2019
- ASU Physics 121: Fall 2020

Presentations

1. **"Analysis of K^*K states photoproduced from the proton"** American Physics Society Division of Nuclear Physics conference: October 16, 2019
2. **"$K^{*\pm}(892)K^{\mp}$ in GlueX"** CISA poster session: December 12, 2020

Publications

1. **"First measurement of near-threshold J/ψ exclusive photoproduction off the proton"**, A. Ali *et al.* (The GlueX Collaboration), Phys. Rev. Lett. **123**, 072001 (2019)

2. **"Beam Asymmetry Σ for the Photoproduction of η and η' Mesons at $E_\gamma = 8.8$ GeV"**, S. Adhikari *et al.* (The GlueX Collaboration), Phys. Rev. C **100**, 052201(R) (2019)

3. **"Measurement of beam asymmetry for $\pi^-\Delta^{++}$ photoproduction on the proton at $E_\gamma = 8.5$ GeV"**, S. Adhikari, *et al.* (The GlueX Collaboration), Submitted to Phys. Rev. C (2020)

4. **"Measurement of the Beam Asymmetry in $\gamma p \to K^+\Sigma^0$ at $E_\gamma = 8.5$ GeV"**, S. Adhikari, *et al.* (The GlueX Collaboration), Phys. Rev. C **101**, 065206 (2020)

5. **"The GlueX Beamline and Detector"**, S. Adhikari *et al.* (The GlueX Collaboration), Nucl. Instrum. & Meth. A **987**, 164807 (2021)